https://ntrs.nasa.gov/search.jsp?R=20180007052 2019-07-30T11:19:20+00:00Z

LARGE SCALE CRYOGENIC STORAGE WITH ACTIVE REFRIGERATION

by

ADAM M. SWANGER
B.S. The Ohio State University, 2012

A thesis submitted in partial fulfillment of the requirements
for the degree of Master of Science
in the Department of Mechanical and Aerospace Engineering
in the College of Engineering and Computer Science
at the University of Central Florida
Orlando, Florida

Summer Term
2018

Major Professor: Louis Chow

© 2018 Adam Swanger

ABSTRACT

Storage and transfer of cryogenic liquefied gases on volume scales from under 10 liters for lab use, up to hundreds of millions of liters for industrial applications is of paramount importance across a vast range of industries. Traditionally, these commodities have been stored at or near the normal boiling point due to relative ease of operation and safety-related considerations; however, this also means that some percentage will always be lost due to environmental heat leaking into the vessel and causing boiloff. These losses become more concerning as scales increase, and are of particular importance for high-cost commodities such helium and hydrogen. Additionally, the normal boiling point has typically marked the highest liquid density achievable, which became a strong driver of end-use system designs such as space launch vehicles. Recent development and testing of an Integrated Refrigeration and Storage (IRAS) system for liquid hydrogen has proven that next generation cryogenic storage operations such as zero boiloff and densification are feasible on a large scale. This IRAS system married an 850 Watt at 20 Kelvin reverse-Brayton cycle commercial cryogenic refrigerator with a 125,000 liter LH_2 storage tank via an internal tubular heat exchanger; thereby allowing heat to be removed directly from the hydrogen, and by extension, providing a means to control the bulk thermodynamic state. Tests of zero boiloff, in-situ liquefaction, and densification down to the triple point were performed, and data including fluid temperature profiles and tank pressure were gathered. Details regarding the design, setup, and testing of the IRAS system are discussed herein, and the data are used to anchor various physics models created to predict the behavior of the system during both transient and steady state operations. Hopefully these efforts will provide a useful basis for the design and implementation of future large scale IRAS systems across numerous industries.

ACKNOWLEDGMENTS

First and foremost I would like to thank Ms. Joette Feeney and the Kennedy Graduate Fellowship Program at NASA Kennedy Space Center for providing me with the opportunity to pursue a graduate degree while continuing to work. Also, Mr. Jason Crusan and Mr. Richard Mcginnis of the Advanced Exploration Systems Program at NASA Headquarters for their continuous support and funding during the five-year hardware build-up and testing campaign, and throughout my fellowship, even in the midst of a challenging financial landscape. I must acknowledge the fantastic team of the Cryogenics Test Laboratory at NASA Kennedy Space Center, whose sustained dedication and commitment to the project vison is what has made it such a resounding success. Without their combined talents this work would not have been possible. Finally, I extend my sincerest thanks to my advisor Dr. Chow, the other distinguished committee members Dr. Kapat and Dr. Notardonato, and Mr. James Fesmire for their encouragement and invaluable insights.

TABLE OF CONTENTS

LIST OF FIGURES vii

LIST OF TABLES ix

LIST OF ACRONYMS AND SYMBOLS x

CHAPTER ONE: INTRODUCTION 1

Overview on Cryogenic Storage & Transport 1

Cryogenic Storage at NASA KSC 4

Integrated Refrigeration and Storage 6

CHAPTER TWO: LITERATURE REVIEW 12

CHAPTER THREE: TEST SETUP 14

GODU-LH2 Design 14

IRAS Tank 16

Refrigeration System 22

Ancillary Systems 24

Data Acquisition 26

Testing Program 26

Testing Results 29

CHAPTER FOUR: ANALYSIS 37

Overview 37

Transient Analysis Data Envelope 37

Transient Physics Models 38

Saturated Model 41

Subcooled Model 49

Steady State Analysis 58

1st Order Analytical Estimate of IRAS Tank Heat Leak 59

Steady State Data Envelope 65

Steady State Refrigerator Performance Analysis 65

CHAPTER FIVE: CONCLUSION 72

CHAPTER SIX: FUTURE WORK 75

APPENDIX A: CURVE-FITS FOR HELIUM INPUT DATA 76

APPENDIX B: SATURATED ANALYSIS FLOW CHART 79

APPENDIX C: SUBCOOLED ANALYSIS FLOW CHART 82

APPENDIX D: GODU-LH2 IRAS HEAT EXCHANGER AREA RELATIONS 86

REFERENCES 88

LIST OF FIGURES

Figure 1: LH_2 and LOX Storage Spheres at LC39 at NASA KSC 5

Figure 2: Simplified Comparison of a Traditional Storage Tank and an IRAS System 9

Figure 3: Aerial View of the GODU-LH2 System 14

Figure 4: GODU-LH2 Storage Tank Prior to IRAS Modifications 17

Figure 5: Cut-Away of GODU-LH2 IRAS Tank 20

Figure 6: Layout of Temperature Sensors inside the IRAS Test Tank 21

Figure 7: GODU-LH2 Refrigeration System 24

Figure 8: Simplified Functional Diagram of the GODU-LH2 System 25

Figure 9: 33% & 46% End-to-End Test Results 30

Figure 10: 67% End-to-End Test Results 31

Figure 11: 100% End-to-End Test Results 32

Figure 12: IRAS Tank Heat Leak Trends 35

Figure 13: Densification Depressurization Data Used for Analysis 41

Figure 14: Saturated Model Setup 42

Figure 15: Saturated Model Results at the 46% Fill Level 45

Figure 16: Saturated Model Results at the 67% Fill Level 46

Figure 17: Saturated Model Results at the 100% Fill Level 46

Figure 18: Subcooled Model Setup 50

Figure 19: Subcooled Model Pressure Trends 55

Figure 20: Subcooled Model Temperature Trends 55

Figure 21: Setup for Man-Way Port Analysis 61

Figure 22: Steady State Refrigerator Performance Model Setup..... 66

Figure 23: Steady State Results at the 46% Fill Level..... 68

Figure 24: Steady State Results at the 67% Fill Level..... 68

Figure 25: Steady State Results at the 100% Fill Level..... 69

Figure 26: GHe Inputs for Transient Analysis at 46% Fill Level..... 77

Figure 27: GHe Inputs for Transient Analysis at 67% Fill Level..... 77

Figure 28: GHe Inputs for Transient Analysis at 100% Fill Level..... 78

Figure 29: IRAS Heat Exchanger Area Ratio vs. Inner Tank Height..... 87

Figure 30: IRAS Heat Exchanger Area Ratio vs. Liquid Height..... 87

LIST OF TABLES

Table 1: Select Properties & Costs of Common Cryogenic Liquids 3

Table 2: Temperature Sensor Coordinates inside the IRAS Test Tank 22

Table 3: IRAS Tank Heat Leak Results..... 35

Table 4: Saturated Model Initial Conditions..... 45

Table 5: Data Used for Steady State Refrigerator Performance Analysis 65

LIST OF ACRONYMS AND SYMBOLS

Acronyms

AES	Advanced Exploration Systems Program
ASME	American Society of Mechanical Engineers
ASTM	American Society for Testing and Materials
BPVC	Boiler and Pressure Vessel Code
CAD	Computer Aided Design
CCAFS	Cape Canaveral Air Force Station
CFD	Computational Fluid Dynamics
CGT	Compressed Gas Trailer
DOT	Department of Transportation
GH_2	Gaseous Hydrogen
GHe	Gaseous Helium
GN_2	Gaseous Nitrogen
GODU-LH2	Ground Operations Demonstration Unit for Liquid Hydrogen Project
GSDO	Ground Systems Development and Operations Program
H_2O	Water
IRAS	Integrated Refrigeration and Storage
ISO	International Organization for Standardization
KSC	Kennedy Space Center
LC39	Launch Complex 39 at Kennedy Space Center
LH_2	Liquid Hydrogen
LN_2	Liquid Nitrogen
LNG	Liquefied Natural Gas
LOX	Liquid Oxygen
MAWP	Maximum Allowable Working Pressure of a Tank
MLI	Multi-Layer Insulation
MSU	Mobile Storage Unit

NASA	National Aeronautics and Space Administration
NBP	Normal Boiling Point
NBS	National Bureau of Standards
NEC	National Electric Code
NER	Normal Evaporation Rate
NFPA	National Fire Protection Association
NIST	National Institute of Standards and Technology
RPM	Revolutions per Minute
SLS	Space Launch System
SSC	Stennis Space Center
ZBO	Zero Boiloff
ZBO-DC	Zero Boiloff Duty Cycle Control Scheme
ZBO-PC	Zero Boiloff Pressure Control Scheme
ZBO-TC	Zero Boiloff Temperature Control Scheme

Units

cm	Length: Centimeters
cm^2	Area: Square centimeters
g	Mass: Grams
hr	Time: Hours
Hz	Frequency: Hertz (cycles/sec)
J	Energy: Joule [$kg\text{-}m^2/s^2$]
K	Temperature: Kelvin
kg	Mass: Kilograms
kPa(a)	Pressure: Kilopascals (absolute)
kPa(g)	Pressure: Kilopascals (gauge)
kW	Power (heat transfer): Kilowatts
L	Volume: Liters
m	Length: Meters
m^2	Area: Square meters

m^3	Volume: Cubic meters
mm	Length: Millimeters
mmHg	Pressure: Millimeters of mercury
MPa	Pressure: Megapascals
mW	Power (heat transfer): Milliwatts
Pa	Pressure: Pascal [kg-m/s^2]
s	Time: Seconds
scm	Standardized volume: Standard cubic meters
slpm	Standardized flow rate: Standard liters per minute
VAC	A/C voltage
W	Power (heat transfer): Watts [J/s]

Symbols

A_{G10}	Area of G-10 support block, m^2
A_{LV}	Area of liquid-to-vapor interface at liquid height for entire tank, m^2
$A_{LV,head}$	Area of liquid-to-vapor interface at liquid height for elliptical head, m^2
A_{MLI}	Area of MLI insulation, m^2
$A_{xs,Dh}$	Cross-sectional area of the inner tank based on hydraulic diameter, m^2
$A_{xs,plug}$	Thermal conduction area of man-way plug cross-section, m^2
$A_{xs,port}$	Thermal conduction area of man-way port cross-section, m^2
$C_{P,liq}$	Specific heat of stored liquid, J/kg-K
D	Inner diameter of man-way port, m
D_h	Hydraulic (inner) diameter of tank, m
D_{piston}	Diameter of expander piston, m
h	Height of liquid (i.e. liquid level), m
h_{fg}	Heat of vaporization, J/g
$h_{GHe,supply}$	Enthalpy of helium at refrigerator outlet (i.e. tank supply), J/g
$h_{HX,in}$	Enthalpy of helium at IRAS heat exchanger inlet, J/g
$h_{HX,out}$	Enthalpy of helium at IRAS heat exchanger outlet, J/g
i	Iterative counter

j	Iterative counter
k	Iterative counter
k_e	Effective thermal conductivity of MLI, mW/m-K
k_{SL}	Thermal conductivity of saturated liquid layer, W/m-K
L	Length of cylindrical tank section, m
L_{SL}	Thickness of saturated liquid layer, m
$\dot{m}_{condense}$	Mass flow rate of condensate, g/s
$\dot{m}_{GHe}$	Mass flow rate of helium, kg/s
m_{liq}	Mass of stored liquid, kg
P_{exp}	Pressure of helium at expander inlet, kPa
$P_{GHe,supply}$	Pressure of helium at refrigerator outlet (i.e. tank supply), kPa(a)
P_{liq}	Pressure of stored liquid, kPa(a)
P_{tank}	Tank pressure (saturated), kPa(a)
P_{vap}	Vapor pressure of stored fluid, kPa(a)
$\dot{Q}_{axial,port}$	Axial heat transfer through man-way port, W
$\dot{Q}_{heater}$	Heat input from in-line heater, W
$\dot{Q}_{HL,liq}$	Tank heat leak in liquid region, W
$\dot{Q}_{HL,total}$	Total tank heat leak, W
$\dot{Q}_{HL,vap}$	Tank heat leak in vapor region, W
$\dot{Q}_{Lift}$	IRAS heat exchanger heat removal, W
$\dot{Q}_{manway}$	Total heat transfer through the man-way assembly, W
$\dot{Q}_{MLI}$	Heat transfer through the man-way port MLI, W
$\dot{Q}_{MLI,broad}$	Heat transfer through the tank MLI, W
$\dot{Q}_{pads}$	Heat transfer through the tank support pads, W
$\dot{Q}_{plug}$	Heat transfer through the man-way plug, W
$\dot{Q}_{port}$	Heat transfer through the man-way port, W
$\dot{Q}_{SL}$	Heat transfer through the saturated liquid layer, W
$\dot{Q}_{VJ,return}$	Heat load on the vacuum-jacketed helium return line, W

$\dot{Q}_{VJ,supply}$	Heat load on the vacuum-jacketed helium supply line, W
T_{exp}	Temperature of helium at expander inlet, K
$T_{GHe,return}$	Temperature of helium at refrigerator inlet (i.e. tank return), K
$T_{GHe,supply}$	Temperature of helium at refrigerator outlet (i.e. tank supply), K
$T_{HX,in}$	Temperature of helium at IRAS heat exchanger inlet, K
$T_{HX,out}$	Temperature of helium at IRAS heat exchanger outlet, K
T_{liq}	Temperature of stored liquid, K
T_{mean}	Average helium temperature across the vacuum-jacketed supply line, K
T_{tank}	Tank temperature (saturated), K
T_{vap}	Vapor temperature of stored fluid, kPa(a)
t	Time, seconds
t_{G10}	Thickness of G-10 support block, m
t_{MLI}	Thickness of man-way port MLI, m
t_{shell}	Thickness of man-way port shell, m
$\hat{V}_{piston}$	Virtual piston volume of expander, m^3
$\dot{W}_{out}$	Work removed by expander, W
X	Axial conduction length of man-way, m
$\hat{X}_{piston}$	Virtual piston displacement of expander, m
λ_{304}	Bulk thermal conductivity of 304 stainless steel, W/m-K
λ_{G10}	Bulk thermal conductivity of G-10 material, W/m-K
ρ_{GHe}	Density of helium, kg/m^3

<u>Additional Symbols (appendix only)</u>

$A_{LV,bottom}$	Area of liquid-to-vapor interface at bottom of saturated liquid layer for entire tank, m^2
$C_{P,GHe,supply}$	Specific heat of helium at refrigerator outlet (i.e. tank supply), J/kg-K
$C_{P,liq,avg}$	Average specific heat of stored liquid, J/kg-K
$k_{SL,avg}$	Average thermal conductivity of saturated liquid layer, W/m-K
$k_{SL,avg,ZBO}$	Average thermal conductivity of saturated liquid layer during ZBO-PC testing, W/m-K

$k_{SL,bottom}$	Thermal conductivity at the bottom (i.e. liquid side) of the saturated liquid layer, W/m-K
$k_{SLbottom,ZBO}$	Thermal conductivity at the bottom (i.e. liquid side) of the saturated liquid layer during ZBO-PC testing, W/m-K
$k_{SL,top}$	Thermal conductivity at the top (i.e. vapor side) of the saturated liquid layer, W/m-K
$k_{SL,top,ZBO}$	Thermal conductivity at top (i.e. vapor side) of saturated liquid layer during ZBO-PC testing, W/m-K
$m_{condense}$	Mass of condensate, kg
m_{GHe}	Mass of helium, kg
$m_{liq,avg}$	Average mass of stored liquid, kg
$m_{liq,NBP}$	Mass of stored liquid at normal boing point, kg
m_{SL}	Mass of saturated liquid layer, kg
$m_{SL,calc}$	Calculated mass of saturated liquid layer, kg
m_{total}	Total mass of stored fluid, kg
$m_{total,NBP}$	Total mass of stored fluid at normal boiling point, kg
m_{vap}	Vapor mass of stored fluid, kg
$m_{vap,NBP}$	Vapor mass of stored fluid at normal boiling point, kg
N_i	Iterative limit for i-loop
N_j	Iterative limit for j-loop
N_k	Iterative limit for k-loop
P_{atm}	Atmospheric pressure, kPa(a)
$P_{tank,avg}$	Average tank pressure (saturated), kPa(a)
P_{ZBO}	Tank pressure during ZBO-PC testing, kPa(a)
$\dot{Q}_{LV}$	Heat transfer through the liquid-to-vapor interface, W
$\dot{Q}_{vap}$	Heat transfer in the vapor region, W
$T_{liq,ZBO}$	Temperature of stored liquid during ZBO-PC testing, K
$T_{sat,ZBO}$	Saturation temperature of hydrogen during ZBO-PC testing, K
t_s	Time step, seconds
t_{SL}	Thickness of saturated liquid layer, m
$T_{vap,avg}$	Average vapor temperature, K

$V_{condense}$	Volume of condensate, m^3
V_{liq}	Stored liquid volume, m^3
$V_{liq,NBP}$	Stored liquid volume at normal boiling point, m^3
V_{SL}	Volume of saturated liquid layer, m^3
V_{vap}	Vapor volume of stored fluid, m^3
$V_{vap,NBP}$	Vapor volume of stored fluid at normal boiling point, m^3
$m_{condense \rightarrow liq}$	Mass of condensate that migrates into the subcooled liquid, kg
Δm_{SL}	Difference in mass of the saturated liquid layer between iterations, kg
$\rho_{condense}$	Density of the condensate, kg/m^3
ρ_{liq}	Density of the stored liquid, kg/m^3
$\rho_{liq,NBP}$	Density of the stored liquid at normal boiling point, kg/m^3
ρ_{SL}	Density of the saturated liquid layer, kg/m^3
$\rho_{SL,bottom}$	Density at the bottom (i.e. liquid side) of the saturated liquid layer, kg/m^3
$\rho_{SL,top}$	Density at the top (i.e. vapor side) of the saturated liquid layer, kg/m^3
ρ_{vap}	Vapor density of the stored fluid, kg/m^3
$\rho_{vap,NBP}$	Vapor density of the stored fluid at normal boiling point, kg/m^3

CHAPTER ONE: INTRODUCTION

Overview on Cryogenic Storage & Transport

Industrial gasses such as helium, hydrogen, argon, nitrogen and oxygen play a crucial role in virtually every industry on Earth. They are used in innumerable applications; everything from welding and fabrication to semiconductor production, and from surgery to space travel—it is not a stretch to assert that the extraction, transport, and storage of such commodities has played a pivotal role in the technological advancement of the human race.

In most applications the end use process requires the molecule/atom rather than the bulk phase product. In other words, the method of storing the required commodity, be it in liquid form or as a high pressure gas, is usually irrelevant to the ultimate goal. For example, from a chemistry standpoint, the Space Shuttle main engines did not explicitly require *liquid* hydrogen (LH_2) and *liquid* oxygen (LOX) to operate, only certain mass flow rates of both elements (although clever engineering exploited the cold power stored by the liquid to cool the engines also, which resulted in a convenient synergy). Storage in liquid form simply provided a means by which the necessary amount of mass (energy)—103,000 kg of hydrogen and 520,000 kg of oxygen in this case—could be reasonably contained onboard the vehicle in order to make it to orbit. Without the large density increase from gas to liquid (865:1 for hydrogen and 877:1 for oxygen) vehicle flight tanks would need to be unrealistically large and heavy, making human space travel impossible by chemical-based propulsion.

This situation is also true for the energy industry, where the decision to store and transport commodities in liquid form was primarily born out of logistical and economic realities. The energy industry ships and stores vast quantities of liquefied natural gas (LNG) throughout the world

because the benefit of condensing large amounts of mass/energy in such a small volume (around 600:1 for natural gas) outweighs the increased complexity and costs; even though virtually all LNG is ultimately gasified and burned in gas turbines used for power production. Thermodynamically this overall process is inefficient. However, the economics bear out, and the adopted transport method of industrial gasses is in liquid form, either over the road in tanker trucks, or over the ocean in tanker ships.

Complicating matters, is the fact that most gaseous commodities cannot be liquefied at ambient conditions—they possess a critical temperature above which liquefaction is impossible, and that usually lies well below Earth average (~293 K). Such commodities are commonly referred to as cryogenic liquids, and their liquefaction temperatures range from ~4 K to ~120 K. Due to the extremely low temperatures involved, storage and transport methods must take into account not only pressure containment, but also high performance thermal insulation systems to deal with the potential for extreme heat transfer between the liquid and ambient environment. This fact, above all others, has shaped the design of cryogenic liquid systems since the first "permanent gas" (oxygen) was liquefied by Louis Paul Cailletet and Raoul Pictet in 1877 [1].

Bulk storage of cryogenic liquids such as nitrogen (LN_2), hydrogen and natural gas has become routine on volume scales ranging from a few liters, used in laboratories and hospitals for example, to hundreds of millions of liters in the case of large LNG facilities [2]. Storage conditions are typically held close to the normal boiling point (NBP) (i.e. saturated at atmospheric pressure) in order to keep the vessel in a minimum-stress state, and/or maintain the low liquid temperature and high density. Table 1 presents some relevant properties and costs of typical cryogenic liquids at NBP.

Table 1: Select Properties & Costs of Common Cryogenic Liquids

Fluid[†]	NBP	Crtical Temperature	Density	Heat of Vaporization	Cost[‡]
	K	K	kg/L	kJ/kg	$/L
Methane (LNG)	111.7	190.6	0.42	510.8	~0.39
Oxygen	90.2	154.6	1.14	213.1	~0.15
Argon	87.3	150.7	1.40	161.1	~1.4
Nitrogen	77.4	126.2	0.81	199.2	~0.08
Hydrogen[‡]	20.4	33.1	0.07	448.7	~0.5
Helium	4.2	5.2	0.12	20.8	~15

[†] All fluid properties referenced from NIST Refprop Version 8.
[‡] Properties of "normal" hydrogen.
[‡] Prices vary temporally, by location, and by quantity. Reported values were determined from various sources, and may not reflect current market values

Because the liquid is stored in a saturated state, any heat transferred into the tank from the environment contributes to liquid loss governed by the heat of vaporization. If the storage times are long, the build-up of vapor must eventually be vented so as not to exceed the pressure rating of the vessel. Heat leak can be minimized by elaborate and sophisticated vessel designs and thermal insulation systems such as vacuum-jacketing plus insulation materials, but can never be completely eliminated; therefore, all users of traditional cryogenic liquid storage tanks must accept some percentage of product loss over time. Historically this loss has been quantified by a term called the normal evaporation rate (NER), and is used as a performance metric when evaluating storage vessels. Due to the importance of the current point it needs to be reiterated that the NER cannot be circumvented using traditional passive methods (i.e. insulation); physics effectively forbids it. The only means to eliminate losses due to unavoidable heat intrusion is to remove it via active refrigeration—therein lies one of the prime motivations for the work presented here.

Cryogenic Storage at NASA KSC

In the 1960s, the National Aeronautics and Space Administration (NASA) accelerated the development of large scale cryogenic liquid storage technologies in support of the Apollo moon missions—the Saturn V vehicle required roughly 1.74M liters of LOX and 1.25M liters of LH_2 on-board at lift-off [3]. Accounting for the normal evaporation rate and other losses, potential launch scrubs/turn-around's, and including margin, NASA engineers commissioned the construction of similarly sized storage spheres for both LOX and LH_2 at Launch Complex 39 (LC39) at Kennedy Space Center (KSC), of roughly double the required on-board volumes (3.41M liters for LH_2 and 3.22M liters for LOX). Similar in construction, the only substantial difference between the two tanks is the thermal insulation system. Both employ expanded perlite powder bulk-fill insulation to help reduce environmental heat leak, however, the LH_2 vessel is vacuum-jacketed, while the LOX sphere is only double-walled and purged with gaseous nitrogen (GN_2) to prevent moisture ingress. Each was designed and certified to store normal boiling point liquid only; meaning that the lowest allowable temperatures and pressures were the NBP of their respective fluids, and atmospheric pressure. Other important design factors are the vacuum loading on the outer vessel of the LH_2 tank, which puts practical limits on how large the tank can be; and the stress on the inner LOX tank due to the weight of the liquid (roughly 16 times that of LH_2). During transfer operations the LH_2 vessel was pressurized to approximately 455 kPa(g), and the liquid was pressure-fed to the vehicle; conversely, the liquid oxygen was pump-fed, which required a tank backpressure of approximately 82.7 kPa(g). Figure 1 shows both spheres during the Space Shuttle program (1981-2011), although little had changed since their commissioning.

Photos: NASA

Figure 1: LH_2 and LOX Storage Spheres at LC39 at NASA KSC

NASA was one of the largest consumers of LH_2 during Apollo, and that trend continued throughout the 30 year duration of the Space Shuttle program. Post-Shuttle analysis revealed that NASA lost approximately 12% of the total liquid hydrogen purchased due to NER, and 28% of liquid oxygen; and accounting for all losses, only about half of the total LH_2 purchased was actually flown, and 32% of the LOX [4]. These commodity losses directly translated to economic losses, but also had many negative latent effects due to the continuous venting of hazardous (flammable) material, and the need to replenish the storage vessels from mobile tankers, considered a hazardous operation that required specially trained and qualified personnel, and was subject to unpredictable weather conditions.

Following the retirement of the Space Shuttle, NASA began development of another heavy lift launch vehicle deemed the Space Launch System (SLS). As with the Shuttle, SLS is designed to be a LOX/LH_2 powered vehicle; however, because of the substantial size difference SLS will require roughly 46% more propellant on-board [5]. This increase puts a strain on the LC-39

storage systems, in particular the hydrogen side. Analysis by the Ground Systems Development and Operations (GSDO) program at KSC, who are responsible for the SLS ground systems, revealed that the existing LH_2 storage capacity supported too few launch attempts—in the case of a scrubbed launch, which is a frequent occurrence, it was possible that there would not be enough LH_2 remaining to support another attempt in 24 hours. This realization prompted GSDO to explore numerous solutions, and ultimately resulted in the decision to build an entirely new storage sphere at LC-39B. This new LH_2 sphere is slated to be placed in close proximity to the existing one, and will be roughly 47% larger by volume, with a usable liquid capacity of 4.73M liters [6].

Because building a new tank is a substantial undertaking, both in terms of time and cost, and because any investment in Pad infrastructure must also consider long term usage—the 1960s era tanks ended up supporting programs for 50 years—GSDO solicited ideas for advanced technologies to possibly be infused into the design. Fully aware of the historical findings discussed above, GSDO was very interested in any technologies related to reducing/recouping propellant losses. Two ideas made the cut and were incorporated into the design as bid options: advanced bulk-fill thermal insulation system using glass bubbles instead of expanded perlite, and a newly developed NASA technology referred to as Integrated Refrigeration and Storage (IRAS).

Integrated Refrigeration and Storage

Following the retirement of the Space Shuttle, and prompted in part by the historical findings reported above, NASA decided to invest in next generation cryogenic storage technologies. A competitive research solicitation was announced in 2011 by the newly formed Advanced Exploration Systems (AES) Program from NASA Headquarters, and research engineers

at KSC responded with a proposal to demonstrate Integrated Refrigeration and Storage (IRAS)—coupling a storage tank with a remotely located cryogenic refrigerator via an internal heat exchanger distributed throughout the bulk fluid volume—on a scale relevant to those required at space launch sites. The proposal was selected for award by AES, and in 2012 work began on the Ground Operations Demonstration Unit for Liquid Hydrogen (GODU-LH2), a large scale IRAS test using LH_2 at Kennedy Space Center.

IRAS technology affords five unique capabilities, and were the primary test objectives of the GODU-LH2 campaign:

1. Zero-loss cooldown of a large cryogenic tank from ambient temperature: Via the internal heat exchanger the refrigerator can be used for initial cooling of the entire tank mass without losing commodity, as opposed to the traditional method of unloading liquid product into the warm tank and boiling most away until the tank cools.
2. Zero-loss tanker off-loading of liquid product: Depending on the commodity, cryogenic liquid tanker trucks are not allowed to vent while in transit, so the product they contain is usually saturated at a higher pressure (and temperature) when they arrive at their destination, requiring venting prior to off-load. This product loss can be recuperated by the IRAS system by simply allowing the storage tank to accept the higher temperature product, and subsequently decreasing the pressure by removing heat with the refrigerator after the off-loading process is complete.
3. Zero Boiloff (ZBO): By balancing the refrigerator lift (i.e. the cooling power) with the NER, in either a steady state manner or cyclically, an IRAS system can prevent boiloff and maintain liquid level indefinitely. This integrated refrigeration eliminates the need to vent,

as well as associated product loss. Constant tank pressure control can also be achieved depending on operational mode.

4. In-Situ Liquefaction: If gaseous product is introduced into the storage tank, the IRAS system can liquefy it to fill the vessel, eliminating or reducing the dependency on tanker trucks to fill the vessel.
5. Densification: If the refrigerator lift is greater than the storage tank heat leak, the liquid can be cooled below its normal boiling point, becoming denser in the process.

Capabilities one through four have obvious economic ramifications, either by directly eliminating product loss, or by providing logistical/operational flexibility. Number five however, is considered to be more of an advanced technological capability; one that can have broad reaching effects on both the launch vehicle as well as the launch pad architecture and operations [7].

Remote placement of the refrigeration system away from the storage tank makes the design of IRAS systems extremely flexible and scalable. It does however, require that a "direct-flow" type refrigeration cycle be employed, such as reverse Brayton, to provide a continuous flow of refrigerant to the internal heat exchanger. Conveniently, Brayton units are commercially available in a wide range of capacities. Most of these machines use gaseous helium (GHe) as the working fluid (i.e. the refrigerant)—which is necessary for IRAS systems used to store liquid helium, and satisfactory for storing liquid hydrogen, but at storage temperatures above roughly 65 K it may be beneficial to entertain a vapor compression cycle using a working fluid with a higher boiling point such as nitrogen or methane.

Regardless of refrigerant or cycle, the core innovation of IRAS is the ability to control the bulk fluid properties inside the tank via direct addition and removal of thermal energy (heat), as

opposed to venting/pressurizing. By directly coupling the cold heat exchanger with the liquid, thermal resistance is minimized. This contributes to faster overall system response and greater control over the state of the stored product. In fact, in a properly designed IRAS system the entire bulk volume of stored liquid can be conditioned anywhere along its respective saturation curve, from the triple point to the maximum allowable pressure rating of the vessel—a fact proven by GODU-LH2 testing, and impossible without the use of active refrigeration. Figure 2 shows a simple graphic comparing a traditional cryogenic liquid storage tank with an equivalent volume IRAS system.

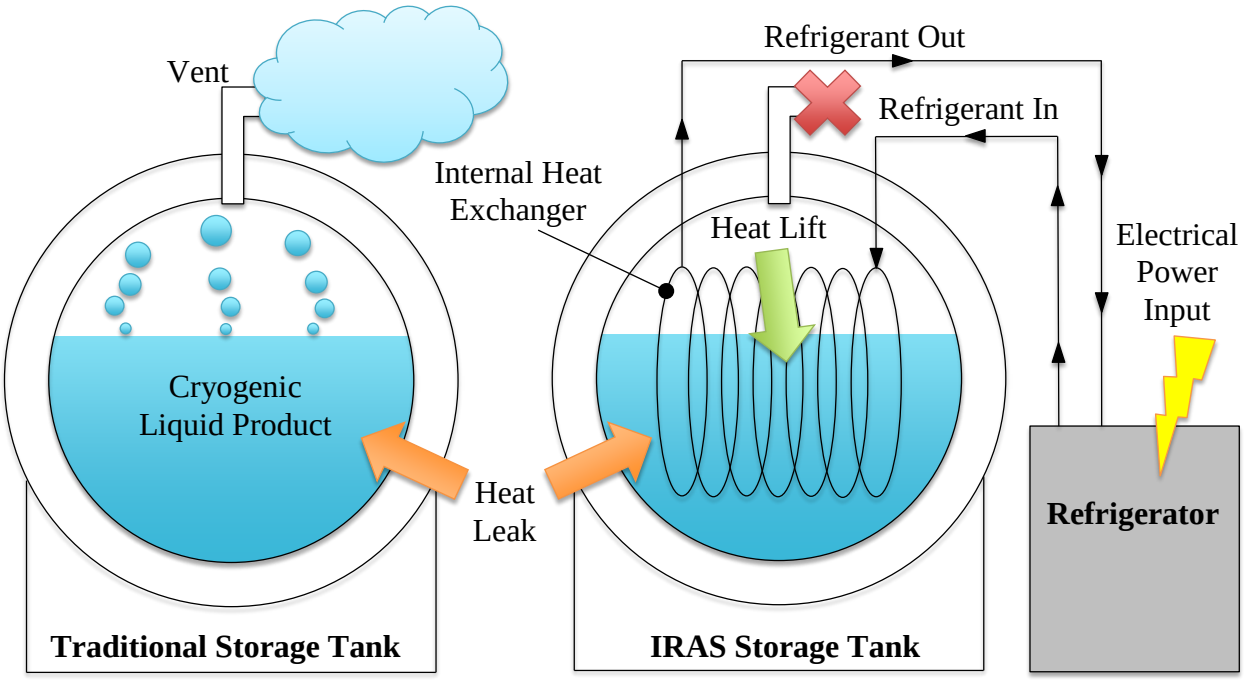

Figure 2: Simplified Comparison of a Traditional Storage Tank and an IRAS System

If the vent is closed on the traditional tank the pressure will build as the heat leak is absorbed by the saturated liquid and converted to vapor. The rate of increase is dictated by the heat of vaporization and thermal performance of the tank itself, and will eventually lead to

structural failure if the tank is not vented to atmosphere. Also resulting from the pressure rise, the liquid temperature will increase and density decrease; both are typically unfavorable to the end-use process for which liquid is being stored in the first place.

In the case of an IRAS tank the refrigeration system must be sized to remove at least as much heat as is entering from the environment or else the pressure will climb similar to a traditional tank. Provided the lift-to-heat leak ratio is ≥1 the vent can remain closed at all times while the refrigerator is operating, ensuring no mass is lost to the ambient environment. Pressure is controlled using refrigerator lift alone by varying the mass flow rate and/or temperature of the refrigerant passing though the internal heat exchanger. If the lift matches the heat leak, the pressure and liquid properties will remain stable; this process is referred to as the pressure control ZBO operating mode (ZBO-PC). ZBO can also be achieved by cycling the refrigerator on and off, allowing the tank to pressurize and de-pressurize within an allowable range, or by setting a constant refrigerant inlet temperature and allowing the tank to reach equilibrium. The former is referred to as duty cycle ZBO (ZBO-DC) and is the most efficient from an electrical power consumption standpoint, but can be hard on mechanical equipment. The latter is temperature control ZBO (ZBO-TC) and results in very long time scales for the storage tank to reach equilibrium. Lastly, if the refrigeration lift is greater than the heat leak, the liquid density will increase (i.e. the liquid will "densify") and its temperature and pressure will decrease. Densifying at the saturation point presents unique challenges. Notably, once the liquid is cooled below its normal boiling point, the pressure becomes sub-atmospheric after which air intrusion into the vessel becomes an obvious and real possibility. This situation can be exacerbated by having numerous and/or large fluid penetrations, so careful thought and engineering must be applied to decrease the possibility of

leaks. Additionally, most storage tanks are not designed to withstand external pressure, therefore the fundamental pressure vessel design must account for this additional load case.

As a result of recent GODU-LH2 testing efforts, the potential for IRAS technology to substantially change the way cryogenic liquids are stored and transported is only beginning to be realized. The door has been successfully opened for possible advanced liquid hydrogen hardware and operations at the KSC launch complex, and the extension to future designs and applications will require a thorough understanding of the unique design, behavior, and response of the GODU-LH2 system in order predict performance, meet economic objectives, and identify potential areas of improvement. This thesis will labor to those ends by focusing on analyzing various aspects of the system performance via generalized physics models, and comparing those to actual data gathered during GODU-LH2 testing.

CHAPTER TWO: LITERATURE REVIEW

In the 1950s, some work was published regarding integrating cryogenic refrigerators and/or reliquefiers with liquid hydrogen storage tanks by individuals affiliated with the National Bureau of Standards (NBS) Cryogenics Engineering Laboratory in Boulder, CO [8, 9]. These works were driven by the scale-up of hydrogen liquefiers in support of the hydrogen bomb program, and were principally centered on the transport and the keeping of LH_2 for long durations (i.e. ZBO) at relatively small volume scales (< 4,000 L). Most notably, a transport truck was built that housed a custom helium refrigerator that supplied cooling to a coil located in the ullage (i.e. vapor space) of a 2,000 L storage tank. This configuration allowed for ZBO by re-condensing boiloff vapor, but was never intended to be used to condition the bulk liquid as was IRAS.

In 1954 Pastuhov spoke of the applicability of closed-loop helium refrigeration for eliminating boiloff in liquefied gas containers, and extended the concept to fluids other than hydrogen by submitting design specifications for a machine capable of producing 1,500 W of refrigeration at 96 K to preserve liquid oxygen [10].

More recently, NASA has explored active refrigeration for use in long duration space missions, where keeping of cryogenic propellants is of vital importance [11, 12]. Various rounds of analysis and testing of flight-like ZBO systems have been conducted and show encouraging results; however, to-date no in-space or zero-gravity demonstrations have been accomplished.

In 2004 the first small scale IRAS-type system was demonstrated by integrating a Gifford-McMahon cycle cryocooler with a 180 L storage vessel by Notardonato et. al. at the Florida Solar Energy Center in Cocoa, FL [13]. This test successfully demonstrated the ability to liquefy

hydrogen from a gaseous source inside the vessel, provide indefinite zero boiloff, and to densify below the normal boiling point using heat removal alone.

In 2010, a larger IRAS test was conducted at KSC using a 400 L liquid oxygen storage tank with an integrated flow-through liquid nitrogen heat exchanger [14]. The heat exchanger height was varied in order to determine what affect it may have on the ability of the refrigerant to condition the liquid. Results revealed the position of the heat exchanger had little effect, and guided the design of the large GODU-LH2 unit.

Most recently, the design, build-up, and individual test results of the large scale GODU-LH2 IRAS system at NASA KSC have been reported [7, 15-20]. GODU-LH2 testing demonstrated ZBO, liquefaction, and densification of hydrogen at various fill levels, with volumes up to 125,000 L. These results proved the applicability of IRAS for keeping and conditioning of cryogenic liquids on scales relevant to launch pads, as well as for a host of other industrial interests, and directly influenced the decision by the GSDO program to incorporate it into the design of the new LH_2 sphere at KSC.

CHAPTER THREE: TEST SETUP

GODU-LH2 Design

Build-up of the GODU-LH2 system began in 2012 in a remote area of Kennedy Space Center where hazardous LH_2 testing could be safely conducted. At a high level, the overall system consisted of two primary subsystems—the IRAS tank, and the refrigerator—as well as various supporting ancillary hardware such as pneumatics, electrical, liquid nitrogen, cooling water, and other subsystems. Each of the subsystems was built-up and integrated together over the course of two and a half years in an empty grass field, culminating in the full system shown in figure 3.

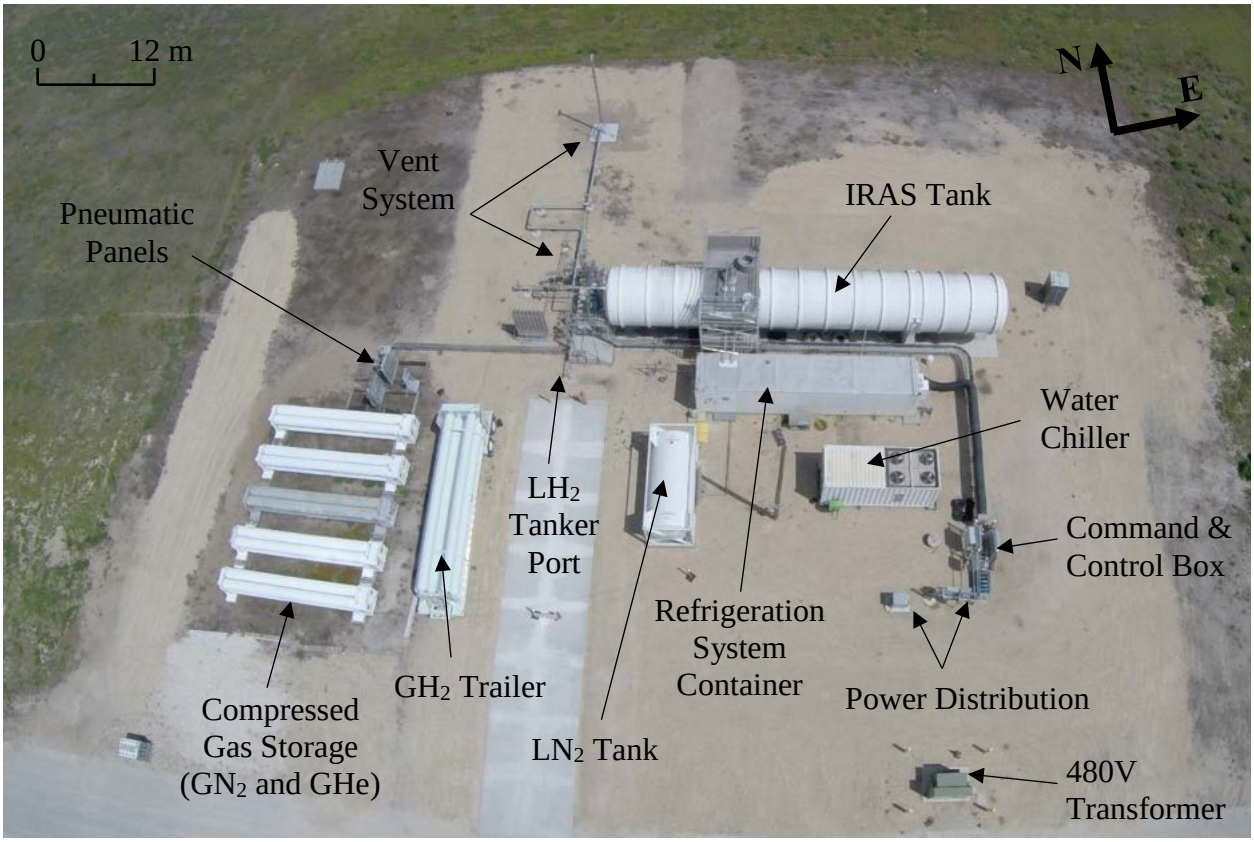

Photo: NASA

Figure 3: Aerial View of the GODU-LH2 System

Residing 183 m west of the test hardware shown in figure 3 was a 30.5 m by 30.5 m steel hanger that acted as a hardware staging and work area, provided equipment storage, and housed an air conditioned trailer that served as the control room. Command and control signaling and data channels were run to and from the control trailer out to the test site via buried Ethernet cables.

Due to the scope and complexity of the test program, as well as various procedural and regulatory requirements, the fluid system design was particularly challenging. In all, seven different fluid commodities were utilized in the design (GN_2, GHe, GH_2, LN_2, LH_2, water and air), each requiring specific, and in some cases sophisticated, hardware and implementation strategies.

A significant objective that drove the overall system architecture was that the refrigeration system be located near the IRAS tank so as to limit parasitic heat losses into the cold helium refrigerant as it was piped between the two components. This objective in turn presented its own set of challenges because the project was also required to comply with national safety standards such as the National Fire Protection Association (NFPA) National Electric Code (NEC), which places restrictions on electrical equipment operating in proximity to flammable commodities (within 7.6 m for LH_2). This requirement at least partially drove the decision to house much of the equipment, including the refrigeration system, inside a standard 12 m ISO shipping container—this allowed the entire container to be kept at a positive pressure using a blower fed by air from outside the NFPA zone. Placing the refrigerator close to the IRAS tank effectively defined the layout of the rest of the site—along with the general desire for site compactness and operational efficiency—since almost every other subsystem interfaced with these two components.

IRAS Tank

The dominate component of the GODU-LH2 system architecture was the integrated refrigeration and storage tank, custom-built (retrofitted) by the project team at KSC. Originally constructed in 1991 by Minnesota Valley Engineering, the vessel spent most of its life as the primary LH_2 storage tank at launch complex 40 on Cape Canaveral Air Force Station (CCAFS) in Florida in support of the Titan launch vehicle. Upon completion of the Titian program in 2005, possession of the vessel was transferred to NASA, and plans to utilize it for large scale IRAS testing began soon thereafter.

Original Construction

A horizontal-cylindrical configuration, the tank has 2:1 elliptical heads and a maximum NBP liquid hydrogen volume of 125,000 L. It is a dewar-type vessel for maximum thermal performance—vacuum-jacketed with 80 layers of aluminum foil and fiberglass paper insulation in the annular space—with original pressure and temperature ranges of 0 to 554 kPa(g) and 20 K to 311 K respectively. The outer jacket measures roughly 23 m long and 3.4 m in diameter, while the inner tank length and diameter are 21.8 m and 2.9 m respectively. Fluid penetrations into the vessel consist of three 7.6 cm liquid transfer ports, a 10.2 cm primary vent port, a 58.4 cm man-way port, and three smaller ($\leq$ 25 mm) ports used for liquid level sensing and sampling. The man-way port is the only point of entry into the inner vessel for personnel and materials, and is sealed by a vacuum-jacketed capacitance probe by the original manufacturer. Figure 4 shows the tank as it was being placed at the GODU-LH2 site, prior to any IRAS modifications.

Photo: NASA

Figure 4: GODU-LH2 Storage Tank Prior to IRAS Modifications

IRAS Modifications

Extensive modifications had to be made to transform this relatively standard LH_2 storage vessel into an advanced IRAS tank, and to accommodate the various GODU-LH2 test objectives. Detailed accounts of the design and construction of the modifications have been covered in the reference material [18-20], thus only a high level description will be presented here to provide an overall understanding of the IRAS tank and its operation.

Most of the modifications were focused on the inside of the vessel, and included four major components: (1) the internal heat exchanger, (2) internal stiffening rings to allow for sub-atmospheric densification testing, (3) an updated man-way plug with provisions for helium refrigerant inlet/outlet ports and instrumentation feedthroughs, and (4) temperature sensor rakes placed throughout the tank to map the horizontal and vertical temperature profiles within the hydrogen. Other modifications were recertification of the vessel to the new temperature and

pressure conditions—13 K to 311 K and -87.6 to 554 kPa(g) respectively—per the American Society of Mechanical Engineers (ASME) Boiler and Pressure Vessel Code (BPVC) requirements, and implementation of helium purge bags at each connection with the pressure boundary in case of a leak during densification testing.

Design and implementation of the internal modifications is best described as a "ship-in-a-bottle" approach. Because the small man-way was the only point of entry, and because no welding was permitted inside the vessel, the heat exchanger, stiffening rings and rakes all had to be modular. Engineering ingenuity resulted in an elegant, synergistic design solution wherein the stiffening rings acted to not only strengthen the inner tank, but also provided a backbone of sorts for suspension of the heat exchanger and rakes.

The IRAS heat exchanger consisted of roughly 290 m of stainless steel tubing distributed throughout the fluid volume. Helium inlet (lower) and exit (upper) manifolds constructed of 25 mm diameter tubing ran axially down the length of the tank, and were suspended from the stiffening rings at the 25% and 75% fill levels via stainless steel wire. Connecting these manifolds were forty 6.4 mm diameter tubes, evenly spaced, and bent into a 3-dimensional shape that followed the curvature of the tank wall. Total heat transfer area of the heat exchanger was approximately 8 m^2, and the entire assembly was secured together using ultra-low-leak Swagelok VCR fittings with silver plated nickel gaskets. Helium refrigerant entered the heat exchanger through the man-way plug, flowed into the bottom manifold through a stainless steel flexhose, where it was distributed down the length of the tank and flowed up to the top manifold through the 6.4 mm coils. Gathering in the top manifold, the helium was plumbed into another flexhose and flow back out the man-way to the refrigerator. In an effort to more evenly distribute the cold

power throughout the entire fluid volume—even though the heat exchanger was adequately spread out, the coldest helium would still exist at the inlet, which would create a undesirable region of localized cooling—custom orifice plates were utilized at the VCR interface between the 6.4 mm coils and 25 mm bottom manifold to balance the mass flow rate across the heat exchanger. These orifices were precision fabricated by a wire-EDM machine using blank VCR gaskets, and the unique hole sizes were determined from a fluid model of the heat exchanger built and analyzed using off-the-shelf thermo-fluid software.

An updated man-way plug was designed and fabricated by NASA Stennis Space Center (SSC) in Mississippi, and was similar to the original unit save three 38 mm bayonet style fluid penetrations for GHe supply/return and GH_2 feed, instrumentation feedthroughs that featured 96 total wires, and aluminum baffles on the liquid-facing side to decrease heat leak.

Temperature rakes were secured to the stiffening rings at three locations within the tank; these rakes were used to locate a total of 20 silicon diode sensors at various vertical and horizontal positions to map the hydrogen temperatures. These rakes consisted of a vertical 38 mm by 38 mm aluminum box channel with horizontal G-10 fiberglass arms and stand-offs to thermally isolate the sensors and provide modularity for construction inside the tank. One rake, housing only vertical sensors, was located at the middle of the tank, while the two others had both vertical and radial sensors (3 arms each), and were placed at each end—one 4.1 m from the middle and the other at 6.2 m.

In addition to the 20 sensors located on the rakes, four others were employed to read helium temperatures at the inlet and outlet of two different 6.4 mm coils in an effort to characterize the heat exchanger performance. Custom feedthroughs were devised and built to connect the helium

flow stream sensor wires to the man-way feedthrough. Figure 5 shows a cut-away of the IRAS tank CAD model, and calls out the significant components.

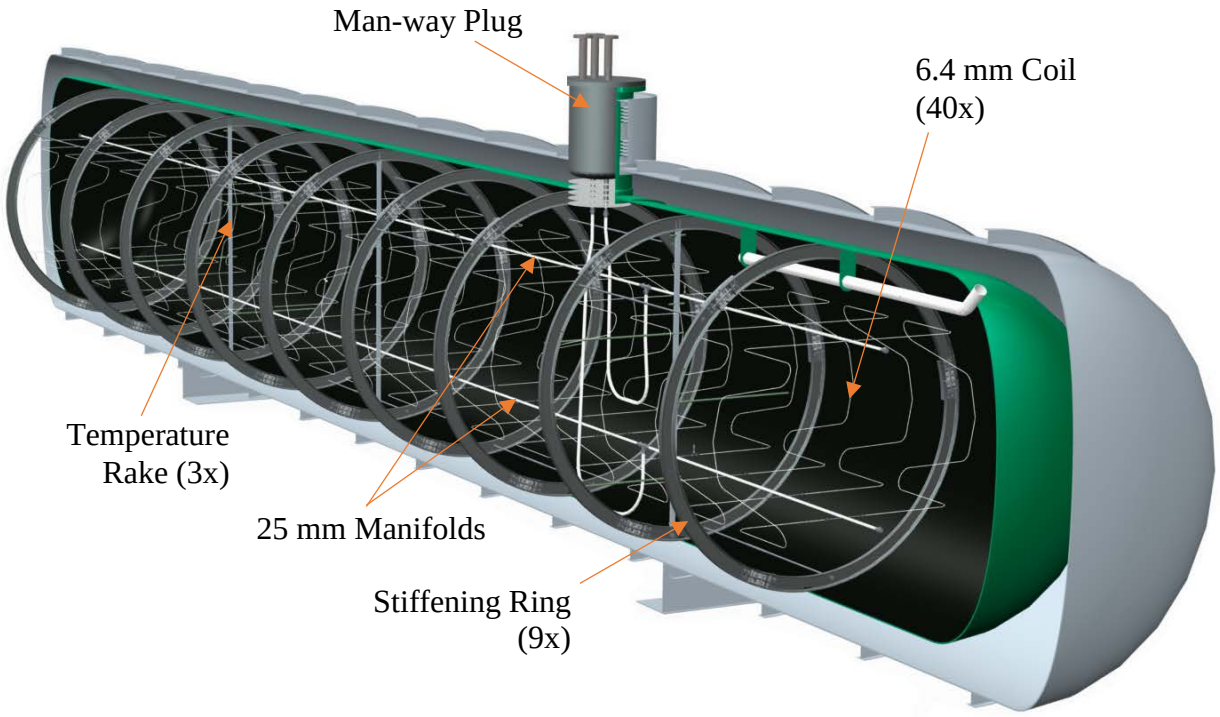

Figure 5: Cut-Away of GODU-LH2 IRAS Tank

Instrumentation

Five primary tank measurements were taken during the course of GODU-LH2 testing: (1) temperature of the liquid hydrogen, (2) temperature of the hydrogen vapor in the ullage space, (3) pressure, (4) liquid level, and (5) hydrogen mass flow rate out the vent (only used during tank heat leak determination). All temperature sensors internal to the tank were silicon diode type units from Scientific Instruments, model Si-410 with group AA calibration (±0.5 K from 450 K to 25 K, and ±0.1 K from 25 K to 1.5 K). Tank pressure was measured by redundant 0-689 kPa(a) transducers from Teledyne Taber. The transducers communicated with the ullage space through 6.4 mm tubes that interfaced to the tank at the 10.2 cm vent outlet, and were located roughly 3 m

away on the concrete pad. Each unit had an error of ±1.0% of full scale (i.e. ±6.89 kPa) within the ambient temperature range with which they were subjected. Liquid level gauging was accomplished via differential pressure measurement between the bottom of tank and the ullage space. A Dwyer Instruments 3100D model differential pressure transmitter with a 0-56 mmHg range was employed for this, and had an accuracy of ±0.075% of full scale (±0.042 mmHg). Differential pressure measurements were linked to the equivalent head of LH_2, and then the head to inner tank geometry to establish the liquid height (i.e. the liquid level). Lastly, a hydrogen mass flow meter was installed in the vent system to characterize the heat leak into the IRAS tank at different fill levels by measuring the steady-state boiloff rate. A Brooks Instruments unit was tasked for this measurement; model SLAMf63 with a 0-900 slpm range and an accuracy of ±0.18% of full scale (±1.6 slpm).

Figure 6 shows the layout of the 20 silicon diode temperature sensors within the tank, designated TT1 thru TT20, and table 2 reports each sensors relative coordinates.

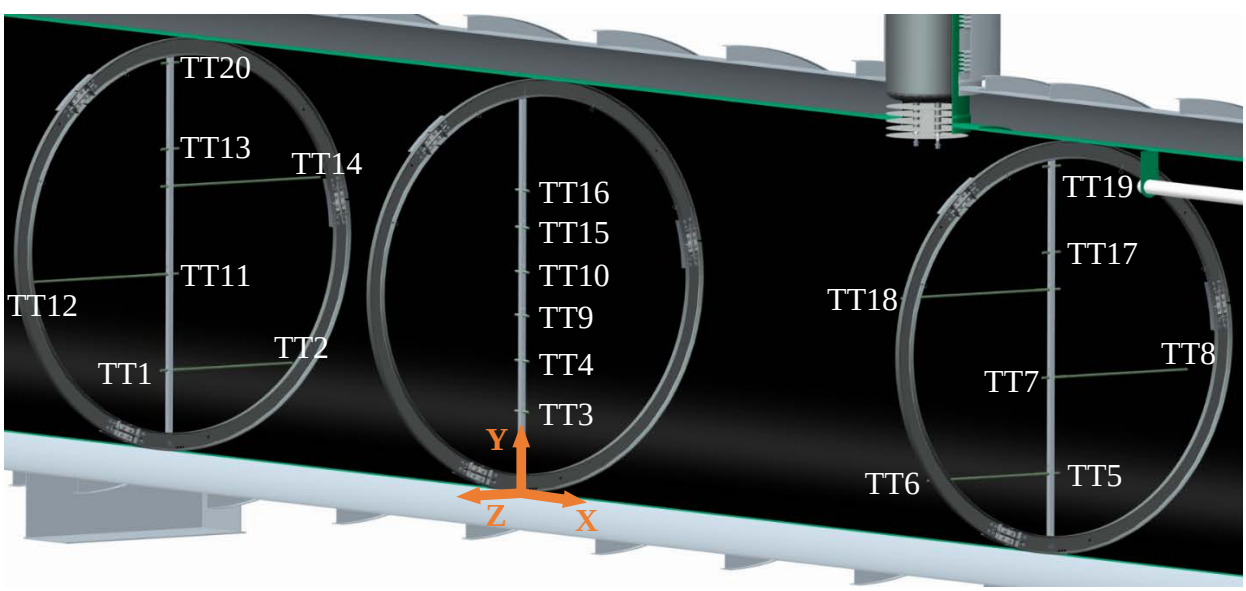

Figure 6: Layout of Temperature Sensors inside the IRAS Test Tank

Table 2: Temperature Sensor Coordinates inside the IRAS Test Tank

	Distance, m				Distance, m		
Sensor #	X-dir	Y-dir	Z-dir	Sensor #	X-dir	Y-dir	Z-dir
TT1	-4.11	0.57	0.16	TT11	-4.11	1.24	0.00
TT2	-4.11	0.57	-0.99	TT12	-4.11	1.24	1.27
TT3	0.12	0.57	0.08	TT13	-4.11	2.12	0.00
TT4	0.12	0.92	0.08	TT14	-4.11	1.85	-1.22
TT5	6.27	0.57	0.00	TT15	0.12	1.85	0.08
TT6	6.27	0.57	1.15	TT16	0.12	2.12	0.08
TT7	6.27	1.24	0.16	TT17	6.27	2.12	0.00
TT8	6.27	1.24	-1.10	TT18	6.27	1.85	1.39
TT9	0.12	1.24	0.08	TT19	6.27	2.72	0.00
TT10	0.12	1.54	0.08	TT20	-4.11	2.72	0.00

Directions correspond to the coordinate system in figure 6

In order to characterize the behavior of the IRAS system when the tank is low versus when it is full, four fill levels were part of the GODU-LH2 test program: 33%, 46%, 67% and 100%. At the 33% fill level (31,250 L) the liquid-to-vapor interface fell just above TT4; at 46% full (57,500 L) it was located very close to TT7, 8, 9, 11 & 12; at 67% (83,750 L) it resided between TT10 and TT15, 14 & 18; and at 100% full all sensors were submerged except for TT19 and TT20.

Refrigeration System

Choice of refrigeration system was driven by three key factors: (1) because the heat exchanger was designed as a flow-through type configuration, the refrigerator had to supply a continuous flow of refrigerant in a closed-loop; (2) since the cold load was LH_2 (NBP of 20.4 K) the choice of working fluid was effectively limited to helium; and (3) preliminary analysis of the storage tank thermal performance yielded an estimated heat leak of around 335 W (see chapter 4).

Therefore the refrigerator had to provide at least this much cooling power, plus margin, in order to successfully achieve all the test objectives. After considering numerous options, a Linde Cryogenics model LR1620 machine was chosen, with an RSX helium compressor. The LR1620 employs a reverse-Brayton cycle with twin parallel piston expanders and four stage of recuperation, while the RSX compressor could supply up to 22 g/s of helium at 1655 kPa(g) and required 480 VAC 3-phase 60 Hz electrical power. To supplement the base cooling capacity, the option for LN_2 precooling was chosen for the GODU-LH2 unit—which required additional hardware and a sacrificial commodity, but boosted the refrigeration performance by roughly a factor of 2. Rated capacities were 390 W at 20 K without precooling, and 850 W with precooling; however, initial performance testing yielded slightly better results of 500 W and 900 W, respectively. When compared to the estimated IRAS tank thermal performance, lift-to-heat leak ratios of 2.7 and 1.5 were achieved with and without precooling, respectively; and as will be seen later, these ratios were found to be higher during testing due to an overestimated tank heat leak.

Control of the cooling power was achieved by introducing heat into the helium supply just after the expansion engine via an in-line resistive heater. Control over this heater was built into the stand-alone Linde software, and responded to a given temperature set point. However, to accommodate the unique GODU-LH2 test objectives, software was developed that could override this feature and control the heater based on a given tank pressure set point. This technique allowed the lift to be varied automatically in order to achieve a constant tank pressure during ZBO-PC testing. Figure 7 shows the LR1620 unit and RSX compressor from two different vantage points inside the aforementioned refrigeration system container.

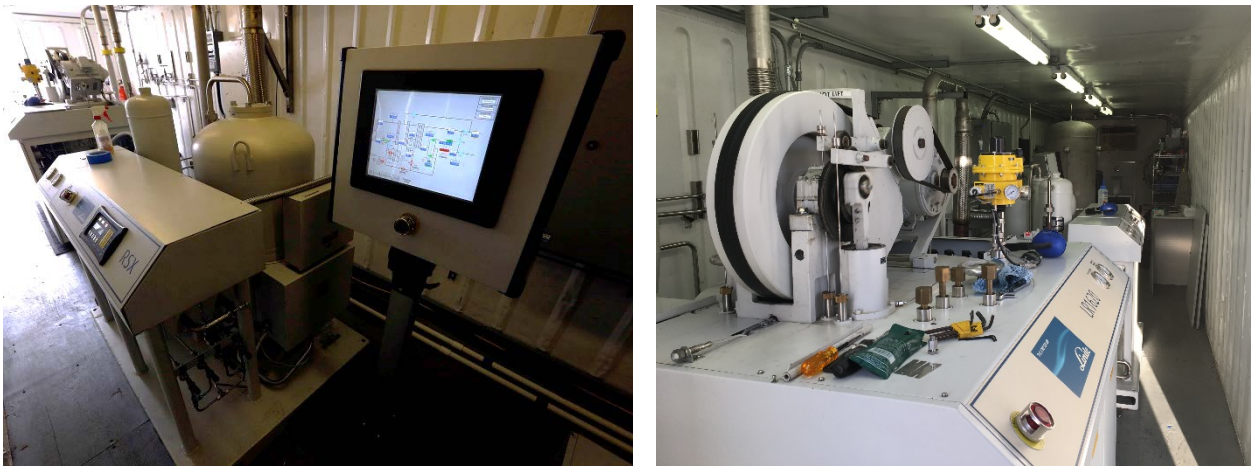

Photos: NASA

Figure 7: GODU-LH2 Refrigeration System
(Foreground left: RSX compressor & control panel; Foreground right: LR1620 refrigerator)

Ancillary Systems

Many smaller subsystems were necessary to facilitate the overall IRAS system. The most significant of these were the close-loop water chiller, pneumatics, and LN_2 storage/transfer systems. A chilled water supply was necessary in order to reject both the heat of compression (in the helium) as well as to cool the RSX compressor oil. Also integrated into a separate smaller standard shipping container (6 m long), the chiller unit was designed to reject 96 kW to the ambient, provide the compressor with a constant supply of 289 K water at a maximum flow rate of 95 L/min, and fully comply with NFPA rules. Five 16.5 MPa mobile storage units (MSU), three GN_2 and two GHe, fed various panels repurposed from the Space Shuttle Program that in turn provided purge and actuation pressure to the site. In total, roughly 5660 scm of inert gaseous storage was permanently on-site, and GH_2 was supplied by 25.5 MPa transportable compressed gas trailers (CGT) on a test-by-test basis. Lastly, LN_2 was stored on-site in a 21,200 L US Department of Transportation (DOT) approved tank placed adjacent to the refrigeration container.

When operating in precooling mode the DOT vessel supplied LN_2 to the refrigerator through vacuum-jacketed hard piping, and the Linde control software maintained a pool of boiling liquid inside the refrigerator using a bang-bang control scheme. Helium refrigerant from the compressor was partially routed through the LN_2 heat exchanger, dropping its temperature close to the boiling point of LN_2 before being fed back into the recuperators. Boiloff vapor was vented to atmosphere out the side of the refrigeration container. Figure 8 shows a simplified functional diagram of the entire GODU-LH2 system.

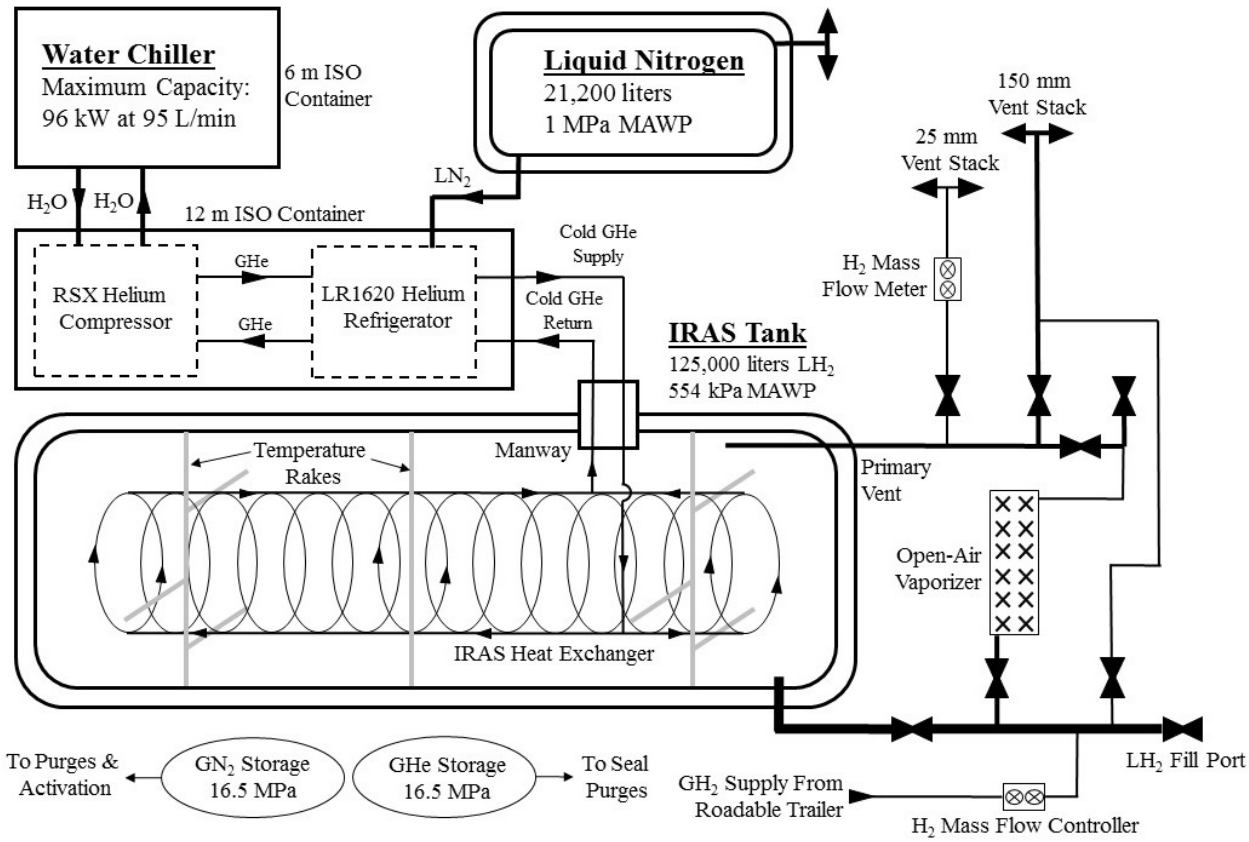

Figure 8: Simplified Functional Diagram of the GODU-LH2 System

Data Acquisition

Three independent systems were used to capture and record the various data from the GODU-LH2 testing. All IRAS tank temperature and mass flow data were recorded using a custom built Labview program, and saved to text files; refrigerator data such as temperatures, pressure, and valve positions were recorded by the Linde-supplied software, which generated a new Excel spreadsheet daily; and the IRAS tank pressure and liquid level readings were captured by another custom built program using Data Historian software, and saved to an on-site server. In order to simplify post-test analysis, these three data files were combined into a master Excel spreadsheet for each test series.

Testing Program

The original test program consisted of performing four individual tests—(1) a steady-state boiloff test to determine tank heat leak, (2) ZBO, (3) liquefaction, and (4) densification—at three different fill level targets: 30%, 60%, and 90%. Secondary objectives were to perform a zero-loss cooldown of the tank prior to introducing LH_2, and zero-loss off-loads of liquid from the tanker trucks at each fill level. Ultimately, an additional level was added to make up for down time associated with equipment failure, so testing was performed at four different liquid levels: 33%, 46%, 67%, and 100%. Also, the discrepancy between the target and actual levels tested was due to the fact that the quantity of liquid that was actually unloaded into the IRAS tank from the tankers depended on numerous, uncontrollable factors; so, in each case the target level was overshot. ZBO was also performed by three separate methods (described previously). In all, 21 separate tests were performed during the course of the GODU-LH2 campaign.

Testing officially began in April 2015 with the zero-loss cooldown of the IRAS tank. The refrigerator was run at full capacity, and GH_2 was introduced into the vessel periodically using a mass flow controller in order to maintain pressure. Over the course of one month the tank temperature was brought from ambient down to ~20 K with no loss of hydrogen, which allowed for the initial no-loss off-load of LH_2 to bring the fill level to 33%. During the tanker operation, the IRAS tank vent valve remained closed, and the tanker transferred roughly 41,250 L of liquid into the vessel. Because the truck was unable to vent while in-route from Alabama, the transferred LH_2 was saturated at a higher pressure (and temperature) than the receiver tank. This condition resulted in rapid boiloff of the transferred product, and a subsequent pressure rise in the tank while its saturation condition came back into equilibrium. This pressure build-up was expected, and was monitored closely to ensure it did not approach the tank maximum. Once the transfer was complete, the refrigerator was brought back online and the pressure immediately began to decrease, ultimately settling at the chosen set point. A similar process was repeated at each fill level, proving that IRAS can afford a user the ability execute completely zero-loss transfer of liquid product from a transportable tanker to a stationary storage vessel.

Typically following a stabilized tanker operation was a period of steady-state boiloff testing (i.e. without refrigeration) to determine the tank performance as a function of liquid level. This objective was achieved via the method known as boiloff calorimetry, wherein the boiloff gases from a test vessel are recorded using a mass flow meter over a long enough duration of time to ensure steady-state is achieved (i.e. the pressure and boiloff flow rate are essentially constant). Because the liquid is saturated, any heat it absorbs is converted directly into vapor, the quantity of which is a function of the latent heat of vaporization (h_{fg}) of the particular fluid. Therefore, once

the steady-state mass flow rate is known the total heat leak into the liquid can be easily determined by simply multiplying it by h_{fg}. For high precision lab calorimeters, this process may capture the entirety of the heat load; however, for certain fluids, and/or real-world tanks, sensible heat can also be absorbed by the vapor, resulting in a large deviation in temperature at the top of the ullage space compared to the saturation temperature at the liquid-to-vapor interface. This situation is exaggerated when the ullage volume is large compared to the liquid volume also (i.e. for low liquid levels), which can lead to significant errors in total heat load estimation if only the latent heat is accounted for. For the GODU-LH2 IRAS tank, this additional heat load was determined by using the upper-most silicon diode reading, closest to the vent (TT19 in figure 6), along with the fact that the pressure was constant and known. From these two quantities the enthalpy of the vapor leaving the tank could be found, and from there the sensible heat absorbed by the ullage calculated.

Once the heat leak was established at a given fill level, zero boiloff, liquefaction, and densification testing commenced. Order and duration of each test was driven by numerous factors, hence was not always consistent between fill levels. For example, ZBO-PC and densification testing had to be moved from the 33% level to 46% due to a lengthy and unanticipated down-time due to failure of the helium compressor—this was, however the only such instance of test sequences being split between fill levels; 67% and 100% saw full test programs. Also, liquefaction was only performed at the 33% and 67% fill levels due to budget and time constraints. Extensive details of individual tests have been reported previously [15-18], therefore will not be greatly elaborated upon here. However, high level results for each fill level will be presented in the next section, as well as more detailed data of particular tests required to substantiate the proceeding analysis.

Testing Results

End-to-end results at each LH_2 fill level and a summary of the IRAS tank heat leak testing/analysis are presented in the following sections. Each of the end-to-end plots reports all hydrogen temperature readings inside the tank (solid lines), as well as the tank pressure (red dashed line). Diode call-outs correspond to figure 6 and table 2. Different tests are delineated by vertical lines and individually labeled for clarity, and curve colors are common between plots. The x-axes are in units of hours, however, because the tests were not always carried out in a sequential fashion they are purposely not labeled, and some discontinuities exist between adjacent test series. Small gaps in data are also present within some test series due to intermittent data drop-outs, usually associated with weather or maintenance. A 200 hour gauge is supplied to give a sense of temporal scale, and can be applied within an individual test series but cannot be summed across them (i.e. across vertical lines). Additionally, "analysis regions" are shown within each densification and ZBO-PC test series that establish the time slices corresponding to the analyses presented in chapter 4. Table 3 and its corresponding figure summarize the IRAS tank heat leak results/trends, and will also be instrumental in the forthcoming analyses.

33% and 46% Fill Level

Figure 9 shows the end-to-end testing at the 33% and 46% LH_2 fill levels. As was mentioned previously, unexpected equipment failure during the 33% campaign, prior to densification and ZBO-PC testing resulted in a long delay, which forced a refill. Because the second LH_2 tanker arrived with more liquid on-board, and it was impractical to attempt to precisely fill the IRAS tank back to the previous level, the resulting transfer filled the vessel to 46%. This

is reflected in figure 9 by the large discontinuity (done deliberately) between liquefaction and densification testing. In total, the graph spans around 1 year worth of actual time—beginning and end dates were May 21st 2015 (33% tanker off-load) to May 2nd 2016 (end of ZBO-PC testing).

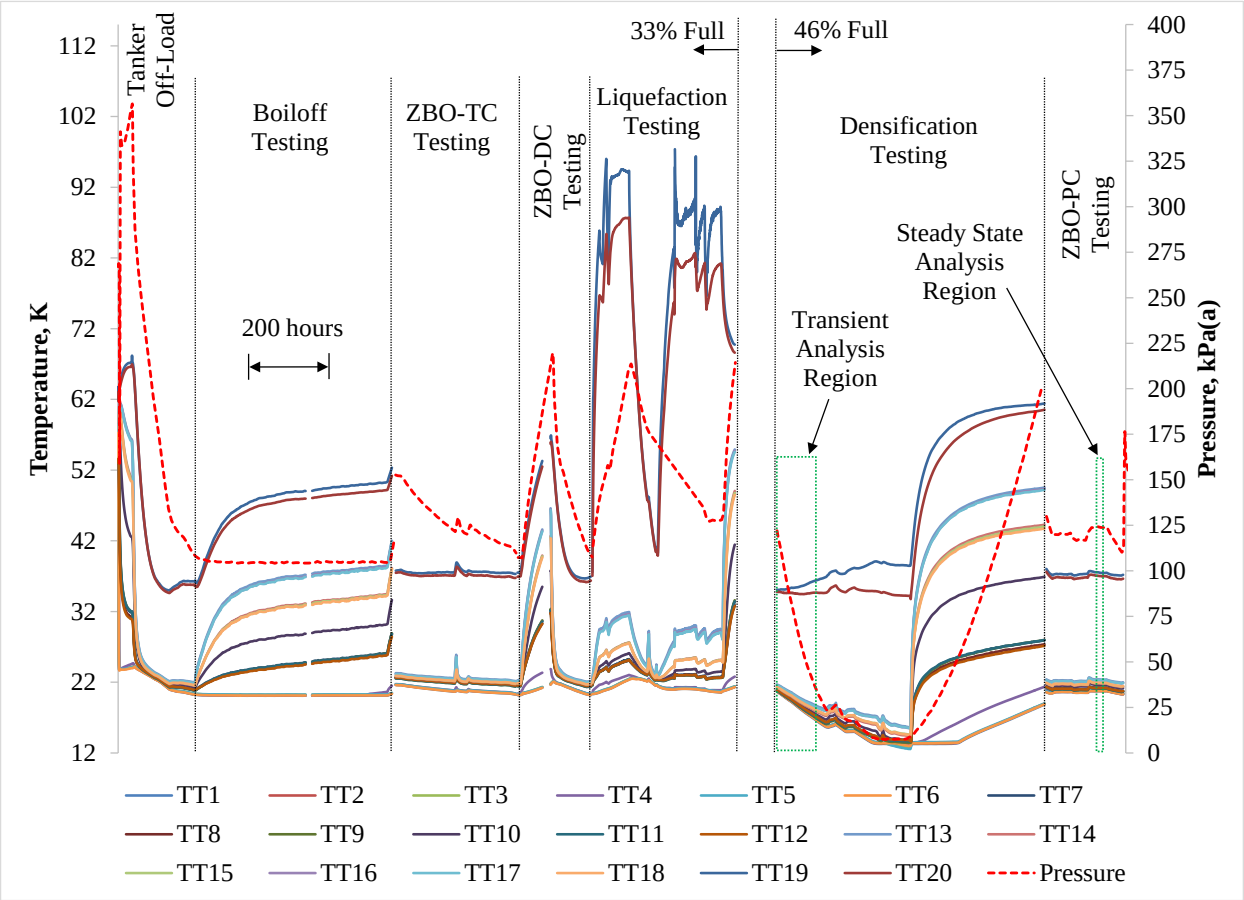

Figure 9: 33% & 46% End-to-End Test Results

<u>67% Fill Level</u>

Testing at the 67% fill level began on May 3rd 2016 with the second zero-loss off-load of LH_2 into the IRAS tank, and ran until August 2nd 2016. Figure 10 shows the end-to-end results for the test campaign. Unlike the lower fill levels, a full series of uninterrupted tests were successfully conducted, which is reflected in the plot by only one discontinuity between individual

tests (from boiloff to ZBO-DC, which is only due to compression of the timeline on the graph, not system down-time as with the 33% program above).

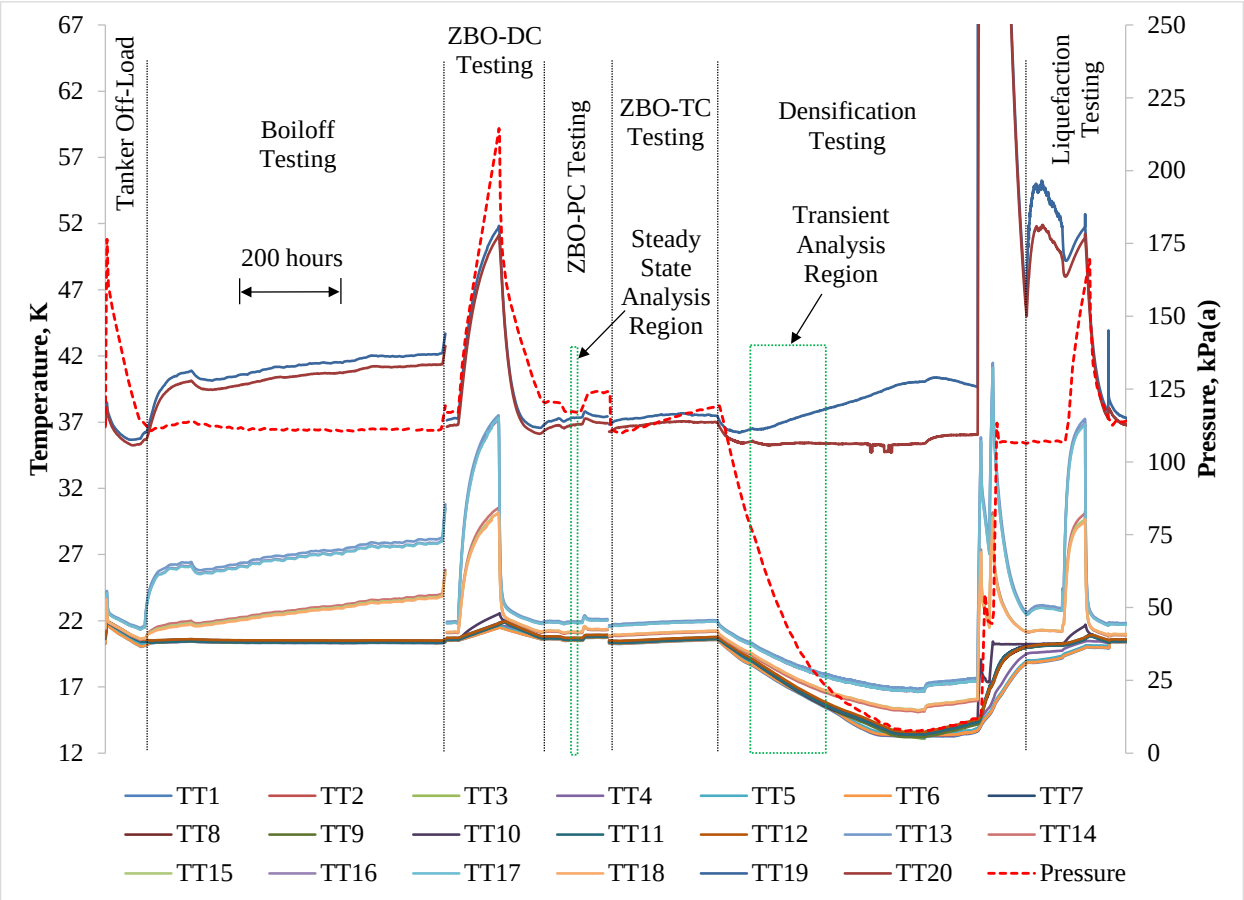

Figure 10: 67% End-to-End Test Results

<u>100% Fill Level</u>

Finally, the tank was filled to 100% on August 3rd 2016, and testing ran through October 1st 2016, at which point the GODU-LH2 project officially ended. Figure 11 shows the end-to-end testing at the 100% fill level. The unlabeled region between the tanker off-load and boiloff test was attributed to an unplanned refrigerator shut-down, which is reflected in the data as a pressure and temperature spike, and the tail-end region marks the end of testing operations.

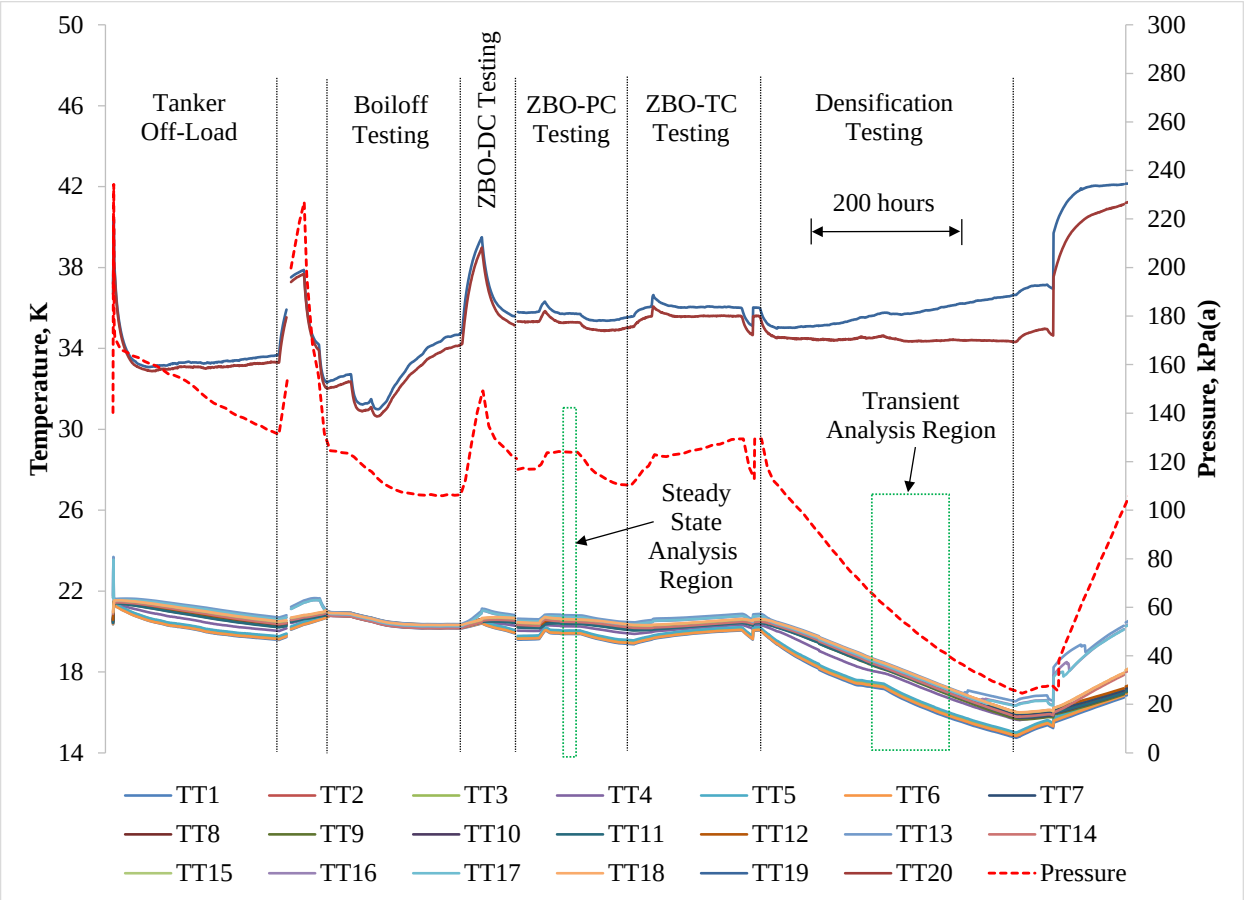

Figure 11: 100% End-to-End Test Results

Discussion of End-to-End Results

Comparing figures 9, 10 and 11 reveals many similarities between tests at the different fill levels. Tanker off-loads and ZBO-DC testing show a signature pressure spike and temperature stratification, followed by a rapid de-pressurization and isothermalization once the refrigerator was brought online; proving that IRAS can be used not only for steady state operation, but, more importantly, for transient control also.

Boiloff tests comprised a large portion of each campaign, and are recognizable by the constant pressure and liquid temperatures, as well as the thermal stratification within the ullage.

Although the ullage temperatures never fully stabilized, the decision was made to declare state-state reached, and proceed with subsequent tests because the mass flow and pressure were constant.

ZBO-PC testing produced a square wave type pressure curve as the refrigerator varied the lift in response to a change in the pressure set point from both above and below the steady state pressure—interestingly, because the control algorithm tried to obtain the set point as fast as possible, when approaching it from below it forced the refrigerator heater to input more heat than was entering the tank naturally; or in other words, the refrigerator became a heater. Once a chosen set point was achieved however, the system was able to maintain it indefinitely by simply varying the lift capacity.

ZBO-TC tests consisted of simply entering a refrigerator outlet temperature, and allowing the hydrogen pressure and temperature to trend toward equilibrium. Unfortunately, the response of the system was such that the time scales required to reach equilibrium were too long to manage within the project schedule. This stands out in the three figures as non-constant pressure curves. At the 33% fill level the pressure decreased during ZBO-TC testing, whereas at the 67% and 100% levels it increased. This was due to both the quantity, and the progressively decreasing value of the set points tested at 33% (beginning at 20 K and ending at 16 K). Due to schedule, an outlet temperature of 18 K was the only set point able to be tested at the 67% and 100% fill levels, which could not stabilize the hydrogen within the allotted time.

Liquefaction testing at the 33% and 67% fill levels produced chaotic curves due to the periodic introduction of warm GH_2 into the tank. Although the system was not optimized for liquid yield, steady state liquefaction was nonetheless achieved, producing around 200 kg of LH_2

total. This proved that IRAS can be used for in-situ liquefaction, but would require some additional sub-systems, such as precooling, and an ortho-to-para reactor, to maximize the liquid yield.

Lastly, the most significant portion of each campaign was dedicated to densification testing. These operations produced characteristic sub-atmospheric de-pressurization curves, and hydrogen temperatures well below the NBP—in fact, tests at the 46% and 67% fill levels yielded liquid temperatures down to and below the triple point, resulting in the production of large quantities of solid hydrogen. Testing at 100% was terminated prior to reaching the triple point due to schedule unfortunately. A notable feature common to all three tests is the divergence of TT19 from TT20. The cause of this is unknown, but it is surmised that helium could have been leaking in through the primary vent line from a purged connection outside. This is plausible because the densification tests were the only time this was witnessed, and is also the only time the tank was subatmospheric. Additionally, TT19 is closest to the vent opening inside the tank. However, post-test sampling of the tank revealed almost pure hydrogen content, so the cause of the divergence is still a matter of debate.

The combination of densification and ZBO-PC testing represented a landmark achievement for the GODU-LH2 project and IRAS technology, as it proved that full control over the cryo-fluid properties is achievable anywhere along the saturation curve, from the triple point to the maximum allowable working pressure of the vessel. This is an ability unique to IRAS, and one never before available. In addition, the demonstration of IRAS to create large batches of solid, and/or slush product, with no loss of commodity, is unprecedented. It is estimated that densification at the 46% fill level produced the largest single batch of solid hydrogen in history: 1,020 kg, with a solid-to-liquid mass fraction of 25%, or around 11,780 L of solid material.

IRAS Tank Heat Leak Results

Table 3 summarizes the results of the boiloff calorimetry testing carried out at each fill level, and figure 12 shows the trends for each heat leak component as a function of liquid level. The curve fit equations presented in figure 12 will be used in the chapter 4 analyses.

Table 3: IRAS Tank Heat Leak Results

Fill Level	Boiloff Flow Rate	Tank Pressure	Avg. Liquid Temp.	TT19 Reading	Liquid Heat Load	Ullage Heat Load	Total Heat Load	Total Heat Flux†
	slpm	kPa	K	K	W	W	W	W/m^2
33%	255	104.8	20.2	49.5	170	120	290	1.26
67%	295	114.5	20.5	41.3	196	100	296	1.28
100%	351	109.6	20.3	34.5	234	81	315	1.36

† Based on log-mean area between the outside of the inner shell and the inside of the outer shell

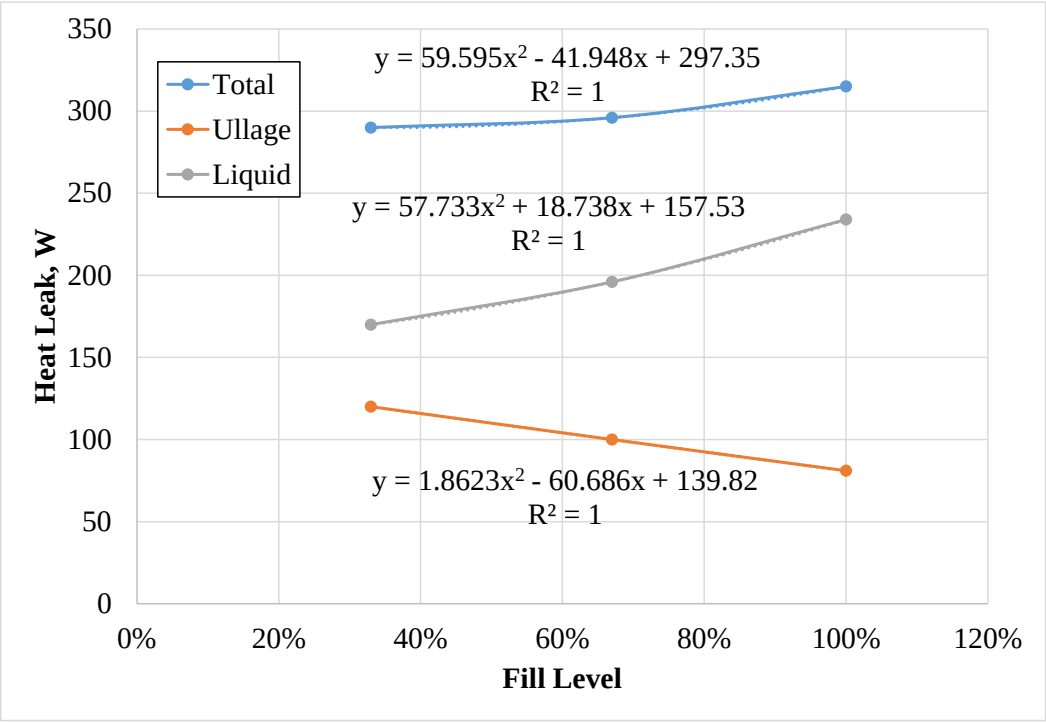

Figure 12: IRAS Tank Heat Leak Trends

Table 3 reveals that the total IRAS tank heat leak was relatively constant with respect to the fill level, varying by only 8% from 33% to 100% full. Also, the pre-test estimate of 335 W was proven to be conservative, which translated to higher lift-to-heat leak ratios and quicker system response times. Using an average heat leak of 300 W, and the actual refrigerator lift capacities presented above, yields lift-to-heat leak ratios of 1.7 and 3, with and without LN_2 precooling, respectively. These are >20% higher than estimates from the pre-test analysis.

CHAPTER FOUR: ANALYSIS

Overview

Analysis focused on the two different regimes presented in figures 9 through 11: transient and steady state. Transient models examined the behavior and response of the system during densification testing (i.e. predicting the rate of depressurization and temperature decrease); while, during steady state ZBO-PC operation the tank pressure and temperatures were constant, therefore the analysis was primarily focused on exploring the initial sizing of the refrigerator, tank heat leak, and how closely the actual performance matched expectation.

Multiple predictive physics models were developed in an effort to better understand the behavior of the GODU-LH2 system over time. Each model was built on assumptions that evolved based upon how accurately the previous model predicted the test data, which ultimately led to two unique transient schemes. Interestingly, the accuracy of a particular model appeared to be dependent on the LH_2 fill level; therefore, none of the models could be called "best," or "most accurate" across all fill levels. Although the GODU-LH2 test data was used to anchor the analysis, the models were purposely generic—applicable to any tank size/geometry, and any desired cryogenic fluid—with the goal of predicting the performance of future IRAS systems.

Transient Analysis Data Envelope

One of the most unique and enabling capabilities of the IRAS technology is its ability to densify large quantities of stored commodity. Because the tank is a closed-system during this operation the pressure decreases as heat is removed by the refrigerator. Eventually the pressure will fall below atmospheric, effectively transforming the vessel into a large vacuum chamber.

Because of this added complexity the behavior of an IRAS system during densification is of particular importance and interest, hence much attention was afforded to the analysis of these tests.

Developing predictive models that could capture every conceivable system perturbation, such as changes in lift capacity due to refrigerator valve adjustments, would be exceedingly difficult. Instead, the models assumed consistent, but not necessarily constant, parameters over time. Because of this approach, test data had to be chosen that accurately reflected this reality in order to anchor the analysis; meaning that time slices from the three densification tests had to be chosen during periods when the system was operating consistently, and without interruption. Also, the duration of time had to be long enough to sufficiently capture the system behavior. At the 46% and 100% fill levels the analysis envelope was 100 hours in duration (from test time = 0 to 100 hours at 46% full, and from 150 to 250 hours at 100%), and 150 hours long at 67% full (from test time = 50 to 200 hours); these correspond to the regions called out in figures 9-11. Within these envelops the depressurization and temperature decrease was relatively smooth and consistent, fulfilling the requirement for stable system operation needed to match the physics models. Refrigerator performance data from these time periods were fed into the respective models, and the outputs compared to the hydrogen data shown in the chapter 3 plots.

Transient Physics Models

All of the transient models were constructed in Microsoft Excel, and coded in Visual Basic. This allowed for use of an Excel imbedded fluid properties solver known as the Reference Fluid Thermodynamic and Transport Properties Database (RefProp) to obtain the hydrogen and helium properties as a function of different parameters. RefProp was developed and distributed by the

National Institute of Standards and Technology (NIST) as a tool for scientists and engineers to better understand the behavior of fluid systems by linking properties predicted by equations of state to actual test data gathered by the Thermophysical Properties of Fluids Group [21]. Spreadsheets were setup with user-defined initial and boundary conditions such as total tank volume and fill level, tank pressure, and hydrogen temperature(s). These values were then fed into a separate part of the spreadsheet that calculated new quantities based on the particular model methodology. The Visual Basic code handled iterative duties such as time accumulation and converging certain fluid properties for a given time step, and tabulated the properties of interest for comparison to test data. Both constant and variable helium inlet conditions (temperature, pressure and mass flow rate) were explored, and because the hydrogen used during testing began as liquid (expect for a tiny amount created during liquefaction testing), all hydrogen properties called by RefProp were for para-hydrogen.

Models were lumped node type schemes, forward-stepping in time. In general, liquid and vapor regions were defined as different nodes, and then the ratio of environmental heat leak-to-calculated refrigerator lift was used to determine how the hydrogen pressure and temperature were affected over time. The models also took into account the migration of mass from the ullage into the liquid via condensation as a result of the excess refrigerator lift. Variable helium inlet conditions were determined from refrigerator performance data captured by the Linde software over the chosen time slice (curve-fit equations of this data were used in the models), and constant properties were simply averaged over the same time period. Lift was calculated by prescribing a certain condition for the helium exiting the IRAS heat exchanger, and for sake of reducing model run times, pressure drop across the heat exchanger was assumed to be zero—this decision was

reached after sensitivity analysis showed very little change in model accuracy when accounting for varying pressure through the tubing. The models also took into account the heat absorbed by the helium in the vacuum-jacketed lines on its way to/from the IRAS tank. This heat leak (36 W @ T_{mean}=24 K) was determined using temperature data gathered across the lines during preliminary GODU-LH2 testing (not captured in figures 9-11), and was assumed to be constant and equal for both the supply and return lines because they were identical (each had a 25 mm diameter inner line, and was 8.3 m long).

As previously discussed, time slices from densification testing were chosen to explore the transient behavior of the GODU-LH2 system. Of primary interest was the ability of the models to predict the rate of depressurization. Because the ullage pressure was essentially constant throughout the tank, this property could be considered a bulk, or non-localized system property; as opposed to the hydrogen temperatures which, although almost equal throughout the tank while the refrigerator was operating, always showed some vertical stratification. Since the models were not equipped to deal with localized temperature differences, the data used for comparison had to be averaged over many diodes, this forced the pressure data to be viewed as higher fidelity. Figure 13 shows the depressurization curve for the three densification time slices analyzed

Because the chosen analysis regions did not always begin with the tank at normal boiling point—as can be seen in figure 13, the 67% full region began at a tank pressure of 71.7 kPa(a), and the 100% full analysis began at 52 kPa(a)—the difference in liquid-to-vapor mass ratio between NBP and the initial model start time had to be accounted for or else the predicted depressurization rate would be skewed. This was accomplished prior to running the transient code by calculating the total NBP mass inside the tank at the given fill level, and then comparing that

to the value determined using the model starting pressure while varying the vapor volume. The Excel Solver function was used to converge on the initial model vapor volume, which then set the vapor and liquid masses that fed into the model as initial conditions.

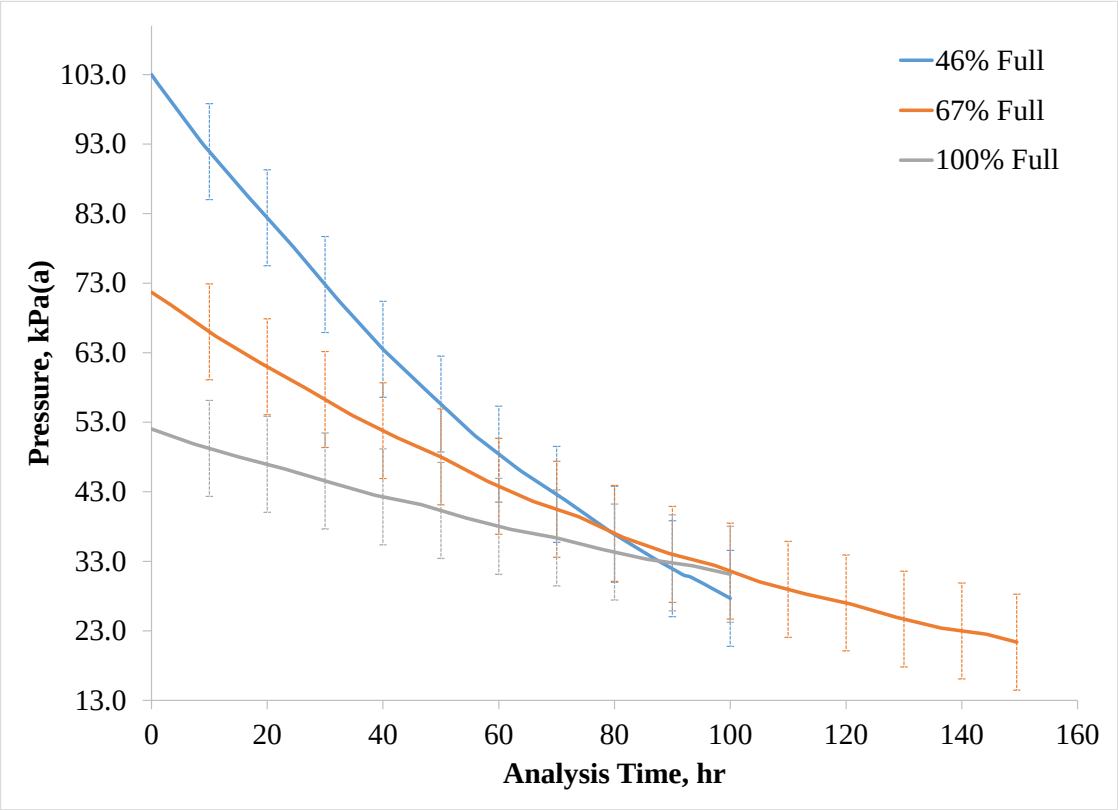

Figure 13: Densification Depressurization Data Used for Analysis
(Error bars = ± 6.9 kPa)

Saturated Model

The first of the two transient models developed was based on an overarching, simplifying assumption that the entire tank was saturated at the given pressure during densification testing. Substantiating this assumption was the trend toward isothermalization witnessed throughout the entire tank when transitioning from boiloff testing to active refrigeration operations—although

some stratification always existed, the entire tank tended to converge on the saturation condition once the refrigerator was brought online. A completely saturated tank meant that the hydrogen properties could be defined by just one parameter (the tank pressure in this case), and both the temperature and pressure of the liquid and vapor would be equal. Additionally, it was assumed that all refrigeration lift occurred in the liquid region, and that the temperature of the helium exiting the heat exchanger was equal to that of the liquid (i.e. the saturation temperature). Figure 14 shows a representative setup of the saturated analysis with relevant variables called-out.

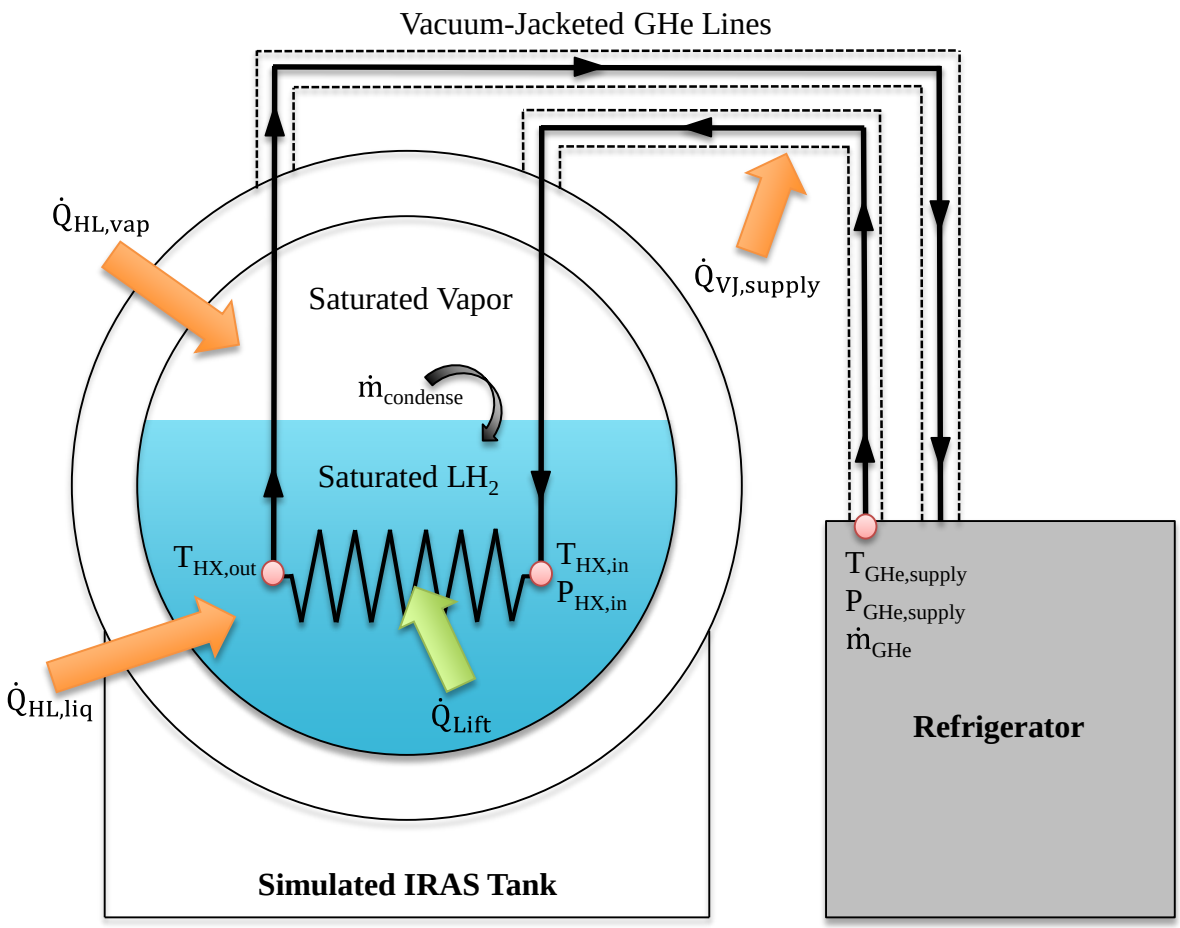

Figure 14: Saturated Model Setup

Models ran with 15 minute time increments, and each new iteration began by updating the helium inlet temperature, pressure and mass flow rate ($T_{GHe,supply}$, $P_{GHe,supply}$ & $\dot{m}_{GHe}$ respectively) per the refrigerator data curve fits (supplied in appendix A), and also took into account the heat absorbed in the vacuum-jacketed supply line ($\dot{Q}_{VJ,supply}$). By prescribing the heat exchanger outlet temperature ($T_{HX,out}$) to the LH_2 temperature calculated in the preceding iteration, a new gross heat lift could be determined using the updated inlet values; and a net heat lift ($\dot{Q}_{lift}$) for the iteration was determined by accounting for the total tank heat leak ($\dot{Q}_{HL,vap} + \dot{Q}_{HL,liq}$) per equation 1.

$$\dot{Q}_{lift_i} = \dot{m}_{GHe_i}\left(h_{HX,in,i} - h_{HX,out,i}\right) - \dot{Q}_{total} \tag{1}$$

Where "i" denotes the time iteration, and "h_{HX}" is the enthalpy of the helium (determined using RefProp). Using this new lift the code calculated an updated liquid temperature per equation 2 within each time iteration.

$$T_{liq_{j+1}} = T_{liq_j} - \frac{t_i \dot{Q}_{lift_i}}{m_{liq_{,k}} C_{p,liq_j}} \tag{2}$$

Where "j" denotes the temperature and specific heat iteration, "k" denotes the mass iteration, "t" is the time step, "m_{liq}" is the liquid mass, and "Cp_{liq}" is the specific heat of the liquid. Because the specific heat was itself a function of the temperature, the average temperature between the jth, and j+1 iterations were fed into RefProp, and then back into equation 2. This forced the temperature to converge to a more accurate value. Once a new T_{liq} was established—which, due to the saturated assumption, was also T_{vap}—an updated tank pressure and liquid density were determined from RefProp. This density was then used to determine a new liquid volume based on the kth liquid mass; and because the tank was a closed system, this led to a new vapor volume, density, and

pressure. This new vapor pressure was compared to the liquid pressure; and because both were required to be equal in order to satisfy the saturated assumption, the kth liquid mass was adjusted up or down slightly depending on which pressure was higher (increased by 0.001% if $P_{vap}>P_{liq}$, and decreased by the same amount if $P_{vap}<P_{liq}$), and then substituted back into equation 2. Once the pressures converged, the relevant properties were recorded in various columns on the spreadsheet, and the initial values were updated for the next time step. This nested loop process forced the accurate calculation of the thermophysical properties for each time step, and outputs could be plotted against actual test data for comparison. A flow chart detailing the saturated model analysis is supplied in appendix B.

Because the variable helium input conditions were extracted from actual refrigerator data gathered during testing, it was information that would not necessarily be known *a priori* when predicting the performance of a new IRAS system. For this reason, a related analysis was run wherein constant helium inlet conditions (i.e. pressure temperature and mass flow rate) were prescribed. The value of each constant boundary condition was an average over the entire time slice shown in the appendix A data—information that, again, may not be known up front, but that could be reasonably assumed/predicted. These results were compared to those found using variable properties in order to determine the validity of such an approach.

Table 4 summarizes the fundamental initial conditions for the saturated model at each of the three fill levels. Liquid and vapor volumes were determined based on the total tank volume (140 m^3) and the maximum useable liquid volume (i.e. the 100% NBP liquid level, or 125 m^3). Other initial conditions—fluid properties such as specific heat and mass—were determined from the fundamental quantities presented in table 4.

Table 4: Saturated Model Initial Conditions

Fill Level	NBP Liquid Volume	Initial Liquid Volume	Initial Vapor Volume	Initial Tank Press	Initial Tank Temp†	Constant GHe Properties		
						Press	Temp	Mass Flow
	m^3	m^3	m^3	kPa(a)	K	kPa(a)	K	g/s
46%	57.5	57.5	82.6	103.0	20.3	148.7	13.2	23.6
67%	83.8	82.6	57.8	71.7	19.2	143.1	12.4	24.8
100%	125.0	121.3	19.1	52.0	18.2	140.5	12.4	25.4

† Saturation temperature at initial tank pressure

Saturated Model Results

Figures 15 through 17 capture the results of the saturated model at each fill level. Graphs are similarly color-coded, and show the IRAS tank pressure and temperature data (averaged across diodes 1 through 18, see figure 6) plotted against the model outputs from both helium inlet conditions. Error bars shown in the plots are: pressure = ±6.9 kPa, and temperature = ±0.1 K.

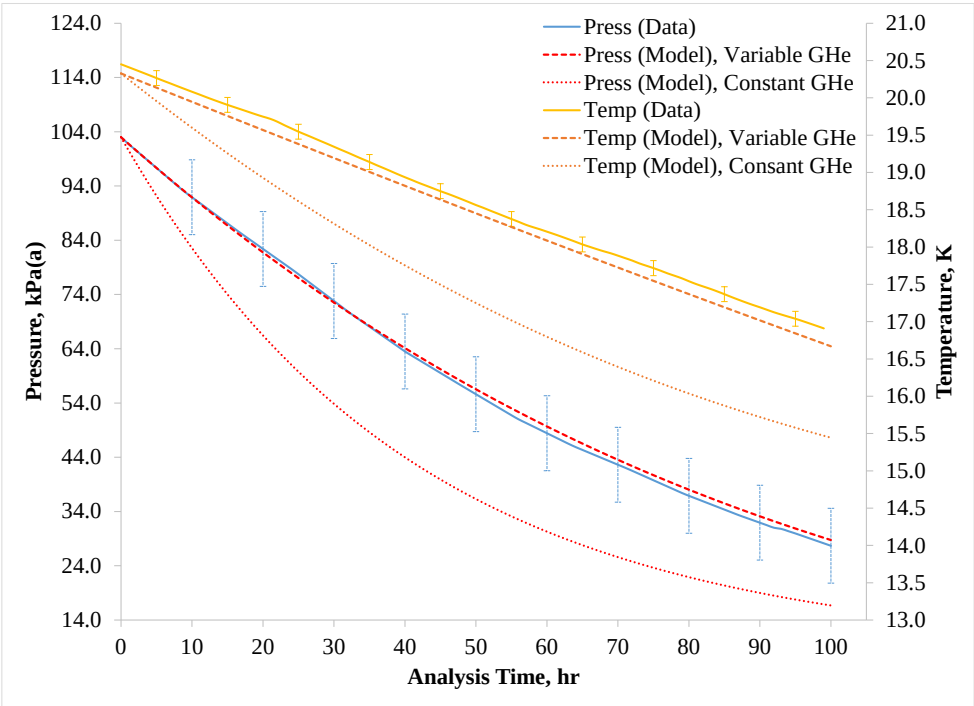

Figure 15: Saturated Model Results at the 46% Fill Level

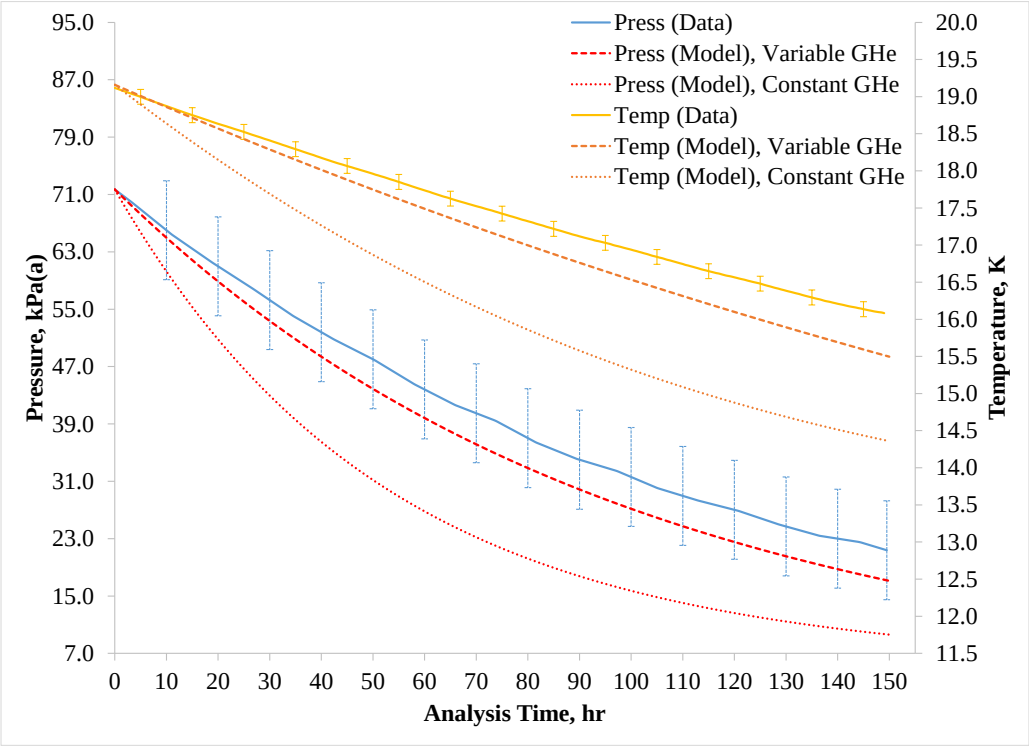

Figure 16: Saturated Model Results at the 67% Fill Level

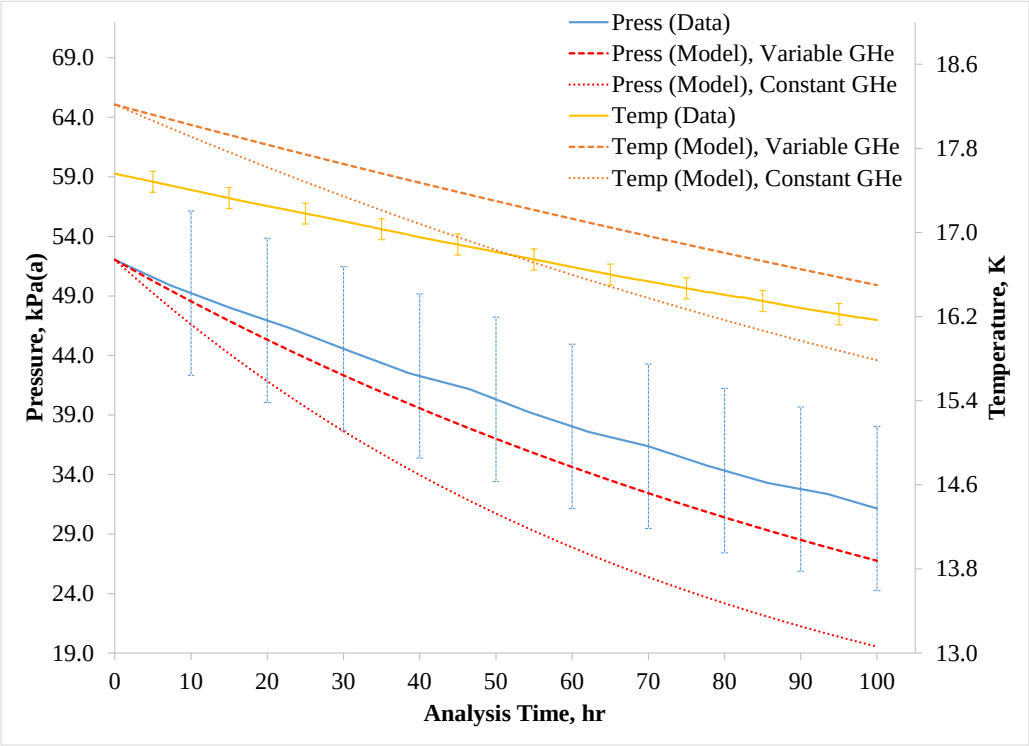

Figure 17: Saturated Model Results at the 100% Fill Level

Discussion of Saturated Model Results

Examining figures 15 through 17 reveals some interesting details and trends. First, it is obvious from the results across all three fill levels, that assuming constant helium inlet conditions lead to dramatically inaccurate predictions of the depressurization and temperature drop. In each case this simulation fell well outside the error envelopes, and were, at times, greater than 50% lower than the pressure test data, and 10% lower than the temperature data. From these results it can also be asserted that the assumption of constant refrigerant inlet conditions is not a reasonable simplification for modeling. Some understanding of the behavior of the refrigerant outlet conditions as a function of return conditions would probably need to be known when modeling a new IRAS system in order to accurately predict the resulting behavior of the stored fluid. However, such knowledge should be attainable by either analysis and/or performance testing of a given refrigeration system over a range of cold "dummy" loads.

The simulation employing variable GHe inlet properties predicted both the temperature and pressure trends with striking accuracy at the 46% fill level. Although the pressure predications fell within the error bounds at each fill level for the chosen time slices, at 46% full the model appeared to almost perfectly mimic the test data. This was also the case for the temperature prediction, although it failed to fall within the error bounds as they were very small (±0.1 K), nevertheless, the model trended extremely close to the data, and was consistent for the entire duration. Over the 100 hour time slice examined at the 46% fill level, the average difference between the pressure and temperature test data versus the model outputs was 1.7% and 0.8% respectively, with maximums of 3.9% and 1.4% respectively. This result seems to validate the overarching simplification that the entire tank was saturated, especially the temperature trend.

Since the temperature data curve was an average over 18 silicon diodes at each time step—both submerged and in the vapor space, and spread throughout the tank—the fact that the saturated model curve stayed in such close and consistent proximity strongly suggests that the entirety of the hydrogen volume was at the saturation condition for at least the time slice examined in figure 15. In fact, analysis were run for different time slices at the 46% fill level in order to determine whether or not the result presented above was simply a function of initial conditions (namely, that the tank began at NBP in figure 15), and in each case the trends were similar. Interestingly, the validation of the saturated model at the 46% fill level was not reflected at the two higher fill levels, a topic discussed next.

Comparing figures 15 and 16, it can be reasonably asserted that the tank was indeed saturated at both fill levels, yet the transient response was dissimilar. The pressure and temperature trends at 67% full match the test data quite well, but had larger errors than at 46% full, with averages of 10.6% and 1.7% respectively (7.6% and 1.1% through 100 hours), and maximums of 20% and 3.5% respectively (14% and 2.4% through 100 hours). Additionally, both the pressure and temperature predictions diverge from the data as time increases; this was also seen at 100% full, however, it is obvious from figure 17 that the tank was not completely saturated. As opposed to 46% and 67% full, the initial tank temperature at 100% fell roughly 0.7 K below the predicted value (which was simply the saturation temperature at the initial pressure), and remained lower over the entire simulation time. Because all of the 18 diodes were submerged at the 100% fill level, the temperature curve presented in figure 17 is the average value of the liquid itself. Therefore, at least some quantity of liquid must have been subcooled. In addition, the fact that the model over-predicted the depressurization rate suggests that the heat transfer between the liquid

and ullage must have been suppressed—this result must also be the case at 67% full also; in fact, the pressure error at the 100 hour mark was the same between the two simulations, roughly 14%. Unlike the 67% fill level however, virtually the entire heat exchanger was submerged at 100% full, save small lengths of the supply and return flex-hoses. This fact possibly explains the aforementioned suppression at the 100% level: perhaps the heat transfer from the vapor to the liquid across only the interface is markedly lower than from the vapor to the exposed heat exchanger tubing, allowing the liquid to be subcooled, and depressing the rate of depressurization (this reasoning partially forms the basis of the second transient model, to be discussed in the next section). However, this reasoning alone does not completely explain the behavior at the 67% level, since a large portion of the heat exchanger was exposed to the vapor region during this test. The relationship between the total heat exchanger area and the area of the liquid-to-vapor interface, as well as the ratio of heat exchanger area in contact with the vapor versus liquid is presented in appendix D for the GODU-LH2 IRAS tank, is thought to play an important role in developing a more complete understanding of this behavior; this analysis however, is left to future examinations.

Subcooled Model

Following the failure of the saturated model to accurately predict the transient behavior at 100% full, a separate model was developed that abandoned the totally saturated assumption in favor of a more complicated scheme using subcooled liquid. This subcooled model was predicated on three primary assumptions: (1) the vapor was saturated at the tank pressure—and by extension, so was the liquid-to-vapor interface; (2) refrigeration lift caused subcooling of the liquid; and (3) a layer of saturated liquid (saturated at the tank pressure) separated the ullage from the subcooled

liquid. It was surmised that this saturated liquid layer would act as a thermal resistance, suppressing the heat transfer between the liquid and vapor, and increasing depressurization times. It was also thought that this was a valid assumption at the 100% fill level due to the fact that the heat exchanger was, for all intents and purposes, completely submerged, allowing for a uniform layer to exist over virtually the entire liquid-to-vapor surface area. This approach is similar to a model used by Ewart and Dergance in 1978 [22], only the liquid layer was assumed to be stratified instead of completely saturated, and wall boundary layers were taken into account that fed the stratified layer with less dense fluid (boundary layers were neglected in the subcooled model since the GODU-LH2 heat exchanger geometry was such that it could be assumed that any wall heat flux was intercepted). Figure 18 depicts the subcooled model setup.

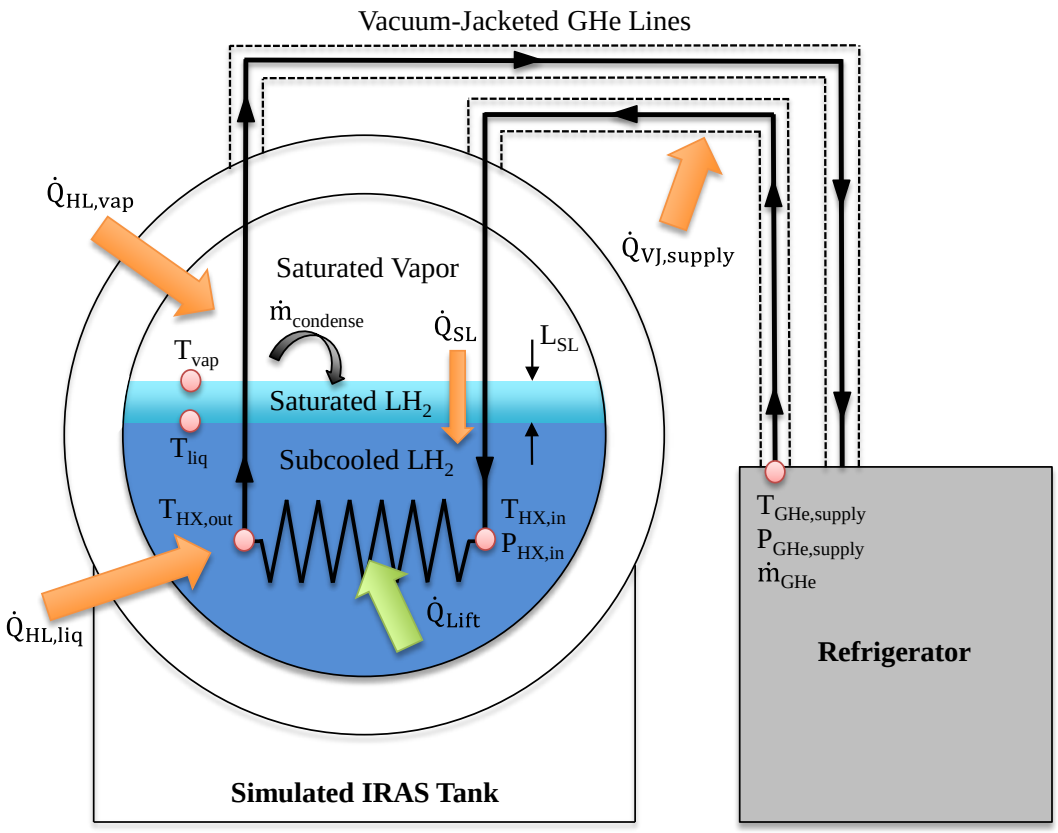

Figure 18: Subcooled Model Setup

The subcooled and saturated models shared many similarities: both assumed all refrigeration lift occurred in the liquid, that the temperature of the helium exiting the heat exchanger was equal to that of the liquid (subcooled liquid in this case), accounted for heat leak into the vacuum-jacketed GHe transfer lines, and used the same scheme to determine initial liquid and vapor quantities. However, where the saturated model converged on the solution that equated the liquid and vapor pressures before moving onto the next time step, the subcooled model calculated the pressure as a function of the heat removed from the vapor. This heat removal was determined by balancing the mass and energy into and out of the vapor, liquid, and saturated layer regions. Referencing figure 18, the following equations summarize this process.

$$\dot{Q}_{lift} = \dot{m}_{GHe}\left(h_{HX,in} - h_{HX,out}\right) - \dot{Q}_{SL} - \dot{Q}_{HL,liq} = \frac{m_{liq}C_{P,liq}}{t}\Delta T_{liq} \tag{3}$$

$$\dot{Q}_{SL} = \frac{k_{SL}A_{LV}}{L_{SL}}\left(T_{vap} - T_{liq}\right) \tag{4}$$

$$\dot{Q}_{Vap} = \dot{Q}_{SL} - \dot{Q}_{HL,vap} = h_{fg}\dot{m}_{condense} \tag{5}$$

Where "k_{SL}" is the thermal conductivity of the saturated layer, taken to be the average for saturated liquid between T_{vap} and T_{liq}; "A_{LV}" and "L_{SL}" are the surface area of the liquid-to-vapor interface, and thickness of the saturated liquid layer respectively, and both were assumed to be constant; "h_{fg}" is the heat of vaporization; and "$\dot{Q}_{SL}$" is the heat transfer through the saturated layer. Equation 3 yields an expression similar to equation 2 for the iterative liquid temperature, only the liquid mass is captured within j^{th} loop since it is not used as a convergent parameter; and combining equations 4 and 5 produces an expression for the mass flow rate of condensate.

$$T_{liq_{j+1}} = T_{liq_j} - \frac{t_i\left[\dot{m}_{GHe,i}\left(h_{HX,in,i} - h_{HX,out,j}\right) - \dot{Q}_{SL,j} - \dot{Q}_{HL,liq}\right]}{m_{liq_{,j}} C_{p,liq_j}} \tag{6}$$

$$\dot{m}_{condense,j} = \frac{k_{SL,j} A_{LV}}{h_{fg,j} L_{SL}}\left(T_{vap,j} - T_{liq,j}\right) - \frac{\dot{Q}_{HL,vap}}{h_{fg,j}} \tag{7}$$

Equations 6 and 7 comprised the prime machinery of the subcooled model code. Initial conditions, along with constant prescribed and/or predetermined values (k_{SL}, A_{LV}, L_{SL}, $\dot{Q}_{HL,vap}$ and $\dot{Q}_{HL,liq}$) established an iterative liquid temperature and condensation rate, and then average quantities for ten different variables from j to j+1 were fed back into the analysis within each ith time iteration to increase accuracy. As in the saturated analysis, once the j-iterations ended, the calculated i+1 properties were prescribed to the given i^{th} time step, and the loop began again with i=i+1. A step-by-step description of the analysis code would be much too cumbersome to be presented here; therefore only key details will be discussed. However, as with the saturated analysis, a flow chart is presented in appendix C.

Because L_{SL} and A_{LV} were assumed constant, the volume of the saturated layer remained constant as well. However, as the temperature of the vapor and subcooled liquid dropped over time the density of the saturated layer increased, therefore the mass of the liquid within it also increased. To keep track of the accumulation of mass with each zone, the analysis compared the mass of the saturated layer at j+1 (calculated using the volume and density at j+1) to that at j (i.e. Δm_{SL}). This delta was then compared to the mass of the condensate determined from equation 7, and the excess was assumed to have migrated into the subcooled liquid mass. The code verified that the combined mass of the vapor, saturated layer, and subcooled liquid always equaled the total mass calculated at the outset.

Surface area of the liquid-to-vapor interface was determined via a combination of geometric relations, and relations derived from the CAD model of the GODU-LH2 IRAS tank. For the barrel section of the tank the liquid-to-vapor interface area is simply the length of the circular segment positioned at the liquid height multiplied by the length of cylinder. For the 2:1 elliptical heads the area ($A_{LV,head}$) was determined by varying the liquid height in the CAD model, and using the internal surface area tool, the values were determined and recorded in Excel to create a curve fit equation. Normalizing $A_{LV,head}$ by the cross-sectional area of the inner tank ($A_{xs,Dh}$, based on the hydraulic diameter), and comparing that to the normalized liquid level (h/D_h), where "D_h" is the hydraulic diameter and "h" is the liquid level, it was found that $A_{LV,head}/A_{xs,Dh} = f(h/D_h)$ was constant with respect to D_h. This relationship was plotted, and the resulting curve-fit equation was combined with the cylindrical relationship to form an estimate for the total liquid-to-vapor surface area (A_{LV}) for a horizontal cylindrical tank with 2:1 ASME elliptical heads.

$$A_{LV} = 2L\sqrt{\left(\frac{D_h}{2}\right)^2 - \left(\frac{D_h}{2} - h\right)^2} + \frac{\pi {D_h}^2}{2}\left[\frac{h}{D_h} - \left(\frac{h}{D_h}\right)^2\right] \tag{8}$$

Where "L" is the length of the barrel section of the tank. At 100% full the GODU-LH2 IRAS tank liquid level was at roughly 2.4 m (95 in), and the inner tank diameter was 2.9 m (114 in), which, when plugged into equation 8, yields a total liquid-to-vapor interface area of 45.5 m^2.

A critical variable in the subcooled analysis was the thickness of the saturated layer, as it dramatically affected the thermal resistance between the subcooled liquid and vapor. Unfortunately, no definitive way to calculate L_{SL} presented itself prior to running the analysis; however, a method was devised that employed equation 4 during steady state ZBO-PC testing that

ultimately yielded realistic results. It was presumed that during steady state operation the heat transfer rate through the saturated layer must be equal to that leaking into the ullage in order to maintain constant pressure (i.e. $\dot{Q}_{SL} = \dot{Q}_{HL,vap}$). ZBO-PC test data was then used in conjunction with equation 4 to back out L_{SL}. At 100% full the heat leak into the vapor region was estimated to be 81 W (see table 3), and from the test data the saturated vapor and average liquid temperatures were 20.98 K and 20.38 K respectively. Thermal conductivity of the saturated layer was estimated between these two temperatures (k_{SL} = 0.104 W/m-K), and with A_{LV} known, equation 4 yielded L_{SL} = 35 mm (1.4 in). L_{SL} is considered to be a physical quantity only in the context of the subcooled model due the assumption that the entire layer is saturated. In reality, there is no definitive elevation where the saturated fluid ends and subcooled fluid begins, leading to the stratified model presented by Ewart and Dergance.

From L_{SL} and A_{LV} the volume of the saturated layer could be estimated, and once all the geometric properties were determined, they were fed into the code as initial conditions, along with the values presented in table 4 and the relevant hydrogen properties. As before, the subcooled model was run with 15 minute time steps, from 0 to 100 hours, using both variable and constant helium inlet conditions. Tank pressure, and liquid and vapor temperatures were tracked over time to compare to the test data. These results are presented in the next section.

Subcooled Model Results

Figures 19 and 20 capture the results of the subcooled model at the 100% fill level. Error bars are the same is in figures 15 through 17, and the saturated model results are superimposed for sake of comparison.

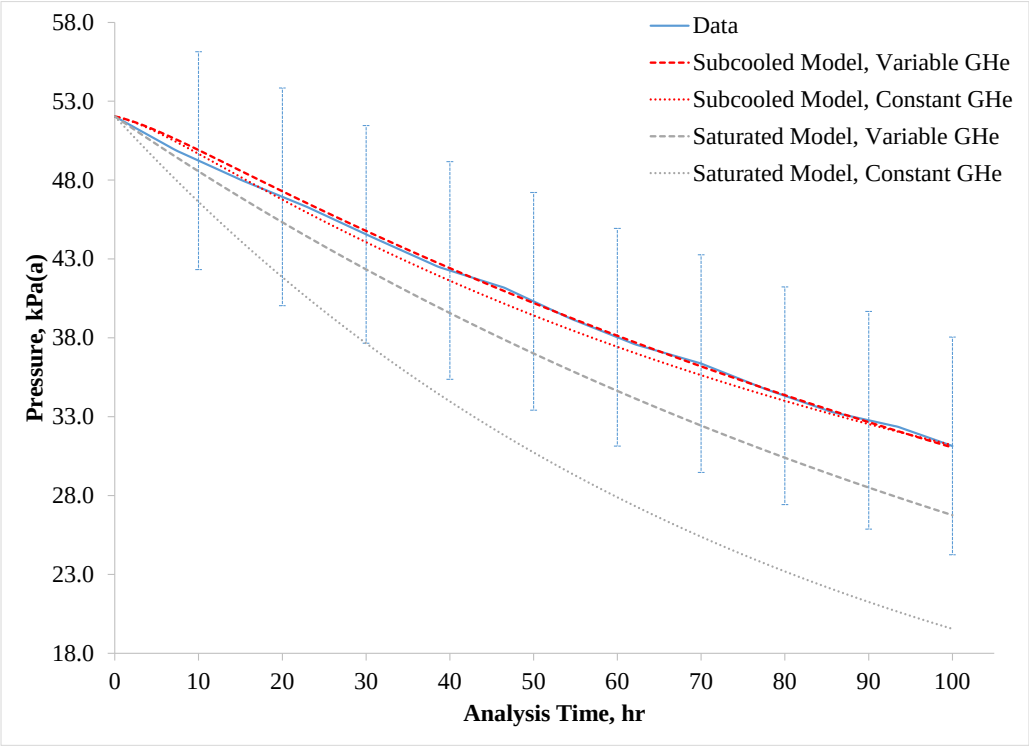

Figure 19: Subcooled Model Pressure Trends

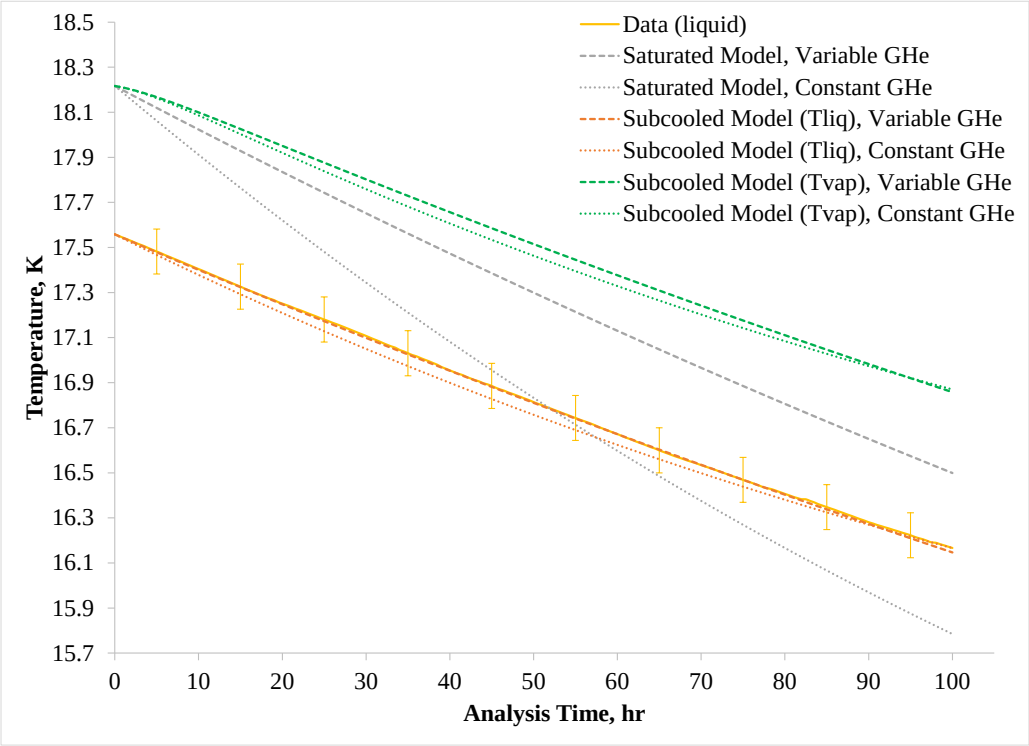

Figure 20: Subcooled Model Temperature Trends

Discussion of Subcooled Model Results

From figure 19 it is obvious that the subcooled model predicted the depressurization trend at 100% full much more accurately than the saturated model—save the slight delay of the pressure and vapor temperature curves to react at the beginning of the simulation, which was due to the sensitivity of the saturated liquid layer thickness on the thermal resistance. The maximum and average absolute error between the model and data for the two helium inlet conditions was 2.5% and 1.2% respectively for constant, and 1.4% and 0.5% for variable. Interestingly, the two GHe boundary conditions did not result in the drastically different behavior observed in the saturated model over the chosen time slice. Both curves trended closely, with a maximum ΔP of only 0.81 kPa; whereas, the maximum ΔP for the saturated model was between 7.26 kPa and 20.3 kPa depending on fill level. Additionally, the prediction did not noticeably diverge from the data as time increased like the saturated model did. However, the constant GHe case did appear to exhibit divergent behavior toward the end of the simulation time, whereas the variable case seemed to maintain a similar slope to the data curve. Looking further into this situation it was found that over the last quarter of the simulation time the error in the slope of the depressurization curve for the variable GHe case decreased from +2.2% to -1.1%, and increased from -8.7% to -19% for the constant GHe case. Also, the difference between data and prediction for variable the GHe case was -0.06 kPa on average, with a standard deviation of 0.12. This result was a marked improvement over the saturated model, where the slope of the variable GHe case was greater than that of the data by anywhere from 7% to 14% over the last quarter of the simulation, and the difference between the data and the prediction was -4.2 kPa on average, with a standard deviation of 0.23.

Turning to figure 20, both GHe cases of the subcooled model predicted the average liquid temperature extremely well. Average absolute errors were 0.2% and 0.03% for constant and variable GHe boundary conditions respectively over the entire 100 hour simulation time, with maximums of 0.35% and 0.12% respectively. Another noticeable feature is that the initial temperature condition of the saturated model was the same as that of the vapor, but quickly diverged thereafter. This is in line with the subcooled model assumption that the vapor was saturated throughout the analysis, and duplicates the trend seen in figure 17.

Although the behavior at the 67% fill level did not deviate from the saturated model as dramatically as it did at 100% full, the subcooled model was nevertheless run at 67% to determine which, if either, yielded a more accurate prediction. These results are not presented graphically, however, the depressurization rate was predicted slightly better than what is shown in figure 16. Although still lower overall, the slope of the curves showed closer agreement over the entire 150 hour time slice, and did not seem to exhibit any divergent behavior. Complicating matters however, was the much smaller saturated layer thickness used in the analysis. Calculated per the same method as in the 100% analysis presented previously (i.e. using steady state ZBO-PC data), the 67% thickness came out to be only 8 mm. Since, as L_{SL} approaches zero the subcooled model essentially makes the same prediction as the saturated model, this smaller thickness, along with the fact that the saturated model almost perfectly predicted the behavior at 46% full, seems to confirm that the IRAS tank trended toward full saturation conditions at lower fill levels regardless of how much heat exchanger area was submerged versus exposed to the vapor space. It is unknown at this time if factors such as tank geometry and stored fluid species bear the primary responsibility

for this result, and whether it is possible to completely saturate the tank regardless of fill level using only IRAS design features such as heat exchanger design and refrigerant flow path.

Steady State Analysis

Exploring the steady state operation of an IRAS system (i.e. maintaining a constant tank pressure) is, in effect, an effort in initial refrigerator sizing also. In order to achieve a constant pressure the environmental heat leak must be balanced with the refrigeration lift at a given fluid state; therefore, the thermal performance of a particular vessel must be known or estimated up front, and then the minimum acceptable refrigeration capacity can be established. In some cases it may be possible to directly test the thermal performance of a potential IRAS tank prior to refrigerator determination via boiloff calorimetry. However, if the system is in the design phases, or testing is simply not feasible, estimation of the steady state heat leak must be conducted analytically. Such was the case during GODU-LH2 planning phases—although, calorimetry was performed during the testing program (see table 3) to establish the actual performance, and validate the analysis. Many different types of thermo-fluid analysis software exist, and can be used to create detailed models of vessels to determine the thermal performance. However, in many cases it is desirable to obtain a simple, first order estimate before committing resources to a detailed thermal analysis. This approach is especially helpful in the planning phases, when developing high level requirements and obtaining cost estimates is a priority.

1st Order Analytical Estimate of IRAS Tank Heat Leak

For a vacuum-jacketed tank such as the one used for GODU-LH2 there are four primary paths of heat ingress: (1) through the broad area thermal insulation system, (2) through the structural supports between the inner and outer vessels, (3) through the man-way penetration, and (4) through the various other fluid and instrumentation penetrations such as pipes and tubes. Details pertaining to 1 through 3 were fairly well known up-front for the GODU-LH2 tank, so an initial heat leak estimate was determined neglecting fluid penetrations.

Numerous broad area thermal insulation systems are employed in vacuum-jacketed cryogenic storage vessels depending on the application and requirements. In the case of the GODU-LH2 tank that system was referred to as multi-layer insulation (MLI)—multiple layers of reflective material, usually aluminum foil or sheets, interspersed with low thermal conductivity spacer sheets to cut down on solid condition between adjacent reflectors, and wrapped around the cold inner tank surface inside the vacuum annulus. When properly designed and executed, this scheme can provide the highest thermal performance known (i.e. lowest heat leak), and has been formally standardized in the American Society for Testing and Materials (ASTM) C740/C740M standard [23]. Performance data for other insulation systems, such as bulk fill perlite and glass bubbles, is also available through ASTM, summarized in standard C1774 [24]. From data curves presented in C740 the heat flux for 80 layers of foil and paper (the MLI system installed in the GODU-LH2 tank) was estimated to be 0.5 W/m^2 at 0.1 millitorr vacuum pressure. Because these data were gathered using boiloff calorimetry, the heat flux number captured every available mode of heat transfer, therefore it could be used to directly estimate the total heat transfer through the MLI assuming the insulated surface area was known. However, because C740 data was obtained

at boundary temperatures of 77 K and 293 K, and the IRAS test tank would be working at LH_2 temperatures (~20 K), the direct use of the heat flux for this application was a simplification. In reality, the thermal performance would change somewhat with the decrease in cold boundary temperature, but for the purpose of preliminary heat leak estimation this simplification was deemed justified. Using a detailed CAD model of the inner tank, the surface area was estimated to be 203 m^2. Multiplying this by the heat flux yielded an estimate for the heat leak through the broad area MLI ($\dot{Q}_{MLI,broad}$) of 101.5 W.

The inner tank was supported by the outer shell inside the annular space on four rectangular pads. In an attempt to cut down on the solid condition heat leak between the vessels each pad was thermally isolated from one another using 17.8 cm x 7.6 cm x 5.1 cm thick G-10 fiberglass epoxy blocks—a standard structural material used in cryogenics. Average thermal conductivity of G-10 in the normal direction, between 20 K and 300 K was obtained from the NIST cryogenic material property database [25], and found to be 0.392 W/m-K. With the geometry and thermal conductivity known, it was possible to estimate the heat transfer through the support pads via the Fourier equation.

$$\dot{Q}_{pads} = 4 \cdot \frac{\lambda_{G10} A_{G10}}{t_{G10}} \Delta T = \frac{4\left(0.392\ \frac{W}{m-K}\right)(0.0136\ m^2)}{0.0508\ m}(300\ K - 20\ K) = 117.5\ W \qquad (9)$$

Although both are somewhat idealized, comparing the heat leak estimates for the MLI versus the support pads illustrates the importance of internal support design in vacuum-jacketed cryogenic vessels. Even though the combined heat transfer area of the four pads is almost 4000

times less than that of the MLI, the calculated heat leak is roughly 16% more than that due to the MLI thermal insulation system.

Because the man-way requires a large, straight-through penetration, this port constitutes a large percentage of the heat leak; especially so as the vessel size decreases. In the case of the GODU-LH2 IRAS tank the man-way penetration was 58.4 cm in diameter, and roughly 86 cm long. It was welded to the inner tank, and connected to the outer via a pair of flexible bellows to allow for thermal contraction. The annular space around the inner pipe communicated with the tank vacuum-jacket, and an MLI blanket (10 layers of foil and paper instead of 80) was employed to cut down environmental heat leak into the port. Figure 21 shows a cut-away of the penetration with relevant information for the heat leak calculation.

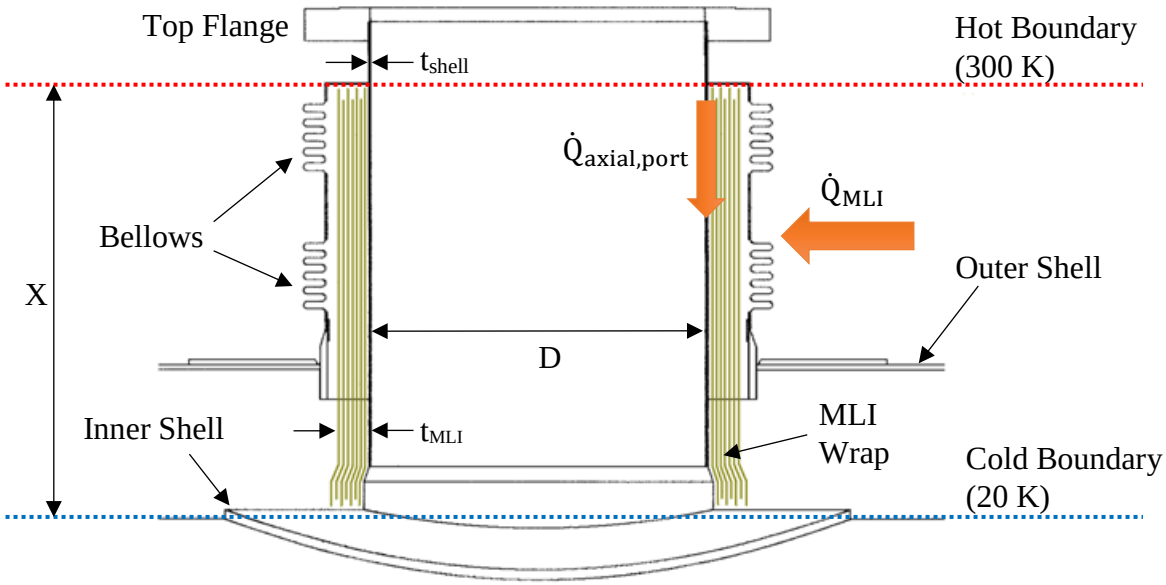

Figure 21: Setup for Man-Way Port Analysis

In figure 21, the inner diameter "D" is given above (58.4 cm), the conduction length "X" was 76.2 cm, the thickness of the cylindrical shell "t_{shell}" was 1.27 cm, and the thickness of the

MLI blanket "t_{MLI}" was 4.36 mm. The penetration was constructed of 304L stainless steel, and consulting the NIST cryogenic materials database it was found that the average bulk thermal conductivity of 304L (λ_{304}) between 300 K and 20 K is 8.75 W/m-K. The fitment of the man-way plug (not shown in figure 21) into the port allowed for a minimal gap to cut down on gas convection, and radiation from the warm top flange—hence, both modes were neglected for this 1st order estimate, as it was assumed they would be overshadowed by the solid conduction heat transfer through the stainless steel. From the geometry and thermal conductivity it was possible to estimate the axial heat leak through the penetration due to conduction.

$$A_{xs,port} = \pi\left\{\left[\left(\frac{D}{2}\right) + t_{shell}\right]^2 - \left(\frac{D}{2}\right)^2\right\} = 238\ \mathrm{cm}^2 \tag{10}$$

$$\dot{Q}_{axial,port} = \frac{\lambda_{304}A_{xs,port}}{X}\Delta T = \frac{\left(8.75\ \frac{W}{m-K}\right)(0.0238\ m^2)}{0.762\ m}(300\ K - 20\ K) = 76.5\ W \tag{11}$$

A similar methodology was used to determine the MLI heat leak through the man-way penetration, only the effective thermal conductivity (k_e) of the MLI was used as opposed to the bulk thermal conductivity. Unfortunately, ASTM C740 data did not include a curve for 10 layers of foil and paper, only 40, 60 and 80; therefore, it was decided instead, to use the Kaganer-k line benchmark [26] to estimate k_e. This benchmark encompasses actual boiloff calorimetry testing of many different MLI systems, similar to the heat flux estimated from C740 above, hence can be used to determine the heat leak directly using the Fourier equation. At 0.1 millitorr the Kaganer-k line estimates k_e to be 0.05 mW/m-K for 293 K and 77 K boundary temperatures—as before, the use of these metrics for a cold boundary other than 77 K introduces some error into the overall

heat leak estimates, but is thought to be minor, and considered a justifiable concession made for sake of simplicity in a 1st order analysis such as this. With the geometry and k_e in-hand, it was possible to calculate the heat leak through the MLI using a cold boundary of 160 K (the average between 300 K and 20 K), and subsequently, the total through the port.

$$A_{MLI} = 2\pi X\left[\left(\frac{D}{2}\right) + t_{shell}\right] = 1.46\ m^2 \tag{12}$$

$$\dot{Q}_{MLI} = \frac{k_e A_{MLI}}{t_{MLI}}\Delta T = \frac{\left(0.05\ x\ 10^{-3}\ \frac{W}{m-K}\right)(1.46\ m^2)}{4.36\ x\ 10^{-3}\ m}(300\ K - 160\ K) = 2.34\ W \tag{13}$$

$$\dot{Q}_{port} = \dot{Q}_{axial,port} + \dot{Q}_{MLI} = 78.8\ W \tag{14}$$

An additional heat leak also existed as a result of the man-way plug itself. This plug was essentially a 57.8 cm diameter by 6.35 mm thick, stainless steel (304L) cylindrical vacuum vessel filled with glass bubble insulation. Consulting ASTM C1774, the effective thermal conductivity of bulk fill glass bubbles at 0.1 millitorr was found to be 0.7 mW/m-K. Because k_e of the glass bubbles was roughly four orders of magnitude lower than the thermal conductivity of the stainless steel, the radiation heat transfer through the plug was neglected. As such, the heat leak through the plug could be estimated in a similar fashion to the penetration; followed by the total heat leak through the entire man-way assembly.

$$\dot{Q}_{plug} = \frac{\lambda_{304} A_{xs,plug}}{X}\Delta T = \frac{\left(8.75\ \frac{W}{m-K}\right)(0.0114\ m^2)}{0.762\ m}(300\ K - 20\ K) = 36.7\ W \tag{15}$$

$$\dot{Q}_{manway} = \dot{Q}_{port} + \dot{Q}_{plug} = 115.5\ W \tag{16}$$

Summing up the heat leak through each of the three paths examined yields a 1st order estimate for the entire tank heat leak during steady state.

$$\dot{Q}_{tank} = \dot{Q}_{MLI,broad} + \dot{Q}_{pads} + \dot{Q}_{manway} = 334.5\ W \tag{17}$$

Comparing this total to the boiloff calorimetry testing results presented in table 3 reveals that the analytical methodology used here over-predicted the heat leak, but not by a substantial amount. The analytical estimate was around 6% higher than the actual at the 100% fill level; however, this number might actually be higher or lower due to the simplifying assumptions. Inclusion of the fluid penetrations would drive the error higher due to the additional heat leak, but incorporating thermal contact resistance between the stainless steel support pads and G-10 blocks would have assuredly drove it back down. Additionally, using 20 K as the cold boundary temperature for the man-way calculations was also overly conservative. In reality, the very top of the tank, or bottom of the man-way, is always some distance away from the actual liquid, therefore is markedly warmer—especially during steady state operation where the ullage is stratified from top to bottom. Raising the cold boundary temperature decreases the ΔT, but increases λ_{304}, and not in a commensurate fashion due to the non-linear temperature dependency for λ_{304}, resulting in an increase or decrease in error. A quick examination into this revealed that, for the particular geometry and methodology presented here, $\dot{Q}_{manway}$ was maximum at a cold boundary temperature of roughly 57 K.

Knowledge of the intrinsic thermal performance of a future IRAS tank, along with the concept of operation for the system (i.e. what lift-to-heat leak ratio is required to achieve the design intent), effectively establishes a baseline for the size, scope and general cost of the necessary refrigeration system. As mentioned in chapter 3, the GODU-LH2 refrigerator was chosen to have

a lift-to-heat leak ratio ranging from 1.5 to 2.7 based upon the total estimated heat leak, stored commodity, heat exchanger geometry, and other factors. However, the basis of any IRAS system is the relationship between the intrinsic tank performance and the refrigerator lift capacity.

Steady State Data Envelope

In order to explore the steady state performance of GODU-LH2 refrigerator, time slices were examined during ZBO-PC testing at each fill level (see figures 9-11). ZBO-PC testing series were chosen because the tank pressure and temperatures were almost constant for a significant period of time at a given pressure set point. This condition meant that the refrigerator lift and tank heat leak were balanced, and therefore a comparison could be made between the two. Time slices (total duration), pressure set points, average hydrogen temperature (taken over all diodes in the tank), and tank heat leak for the 46%, 67% and 100% fill levels are presented in table 5.

Table 5: Data Used for Steady State Refrigerator Performance Analysis

Fill Level	Time Slice (total duration)	Pressure Set Point	Average Tank Temperature	Tank Heat Leak
	hr	kPa(g)	K	W
46%	20.0	22.8	21.4	291†
67%	25.0	15.9	20.9	296
100%	20.0	22.8	20.4	315

† Determined from the curve-fit equation presented in figure 12

Steady State Refrigerator Performance Analysis

Figure 22 shows the model setup used to determine the steady state refrigerator performance. Temperatures, pressures, engine RPM, and heater power were quantities gathered

by the data acquisition system; the tank and vacuum-jacketed line heat leak were presented earlier—governed by the curve-fit equations presented in figure 12, and assumed to be a constant 36 W respectively—and the heat exchanger lift and expander work extraction are the subject of the current examination.

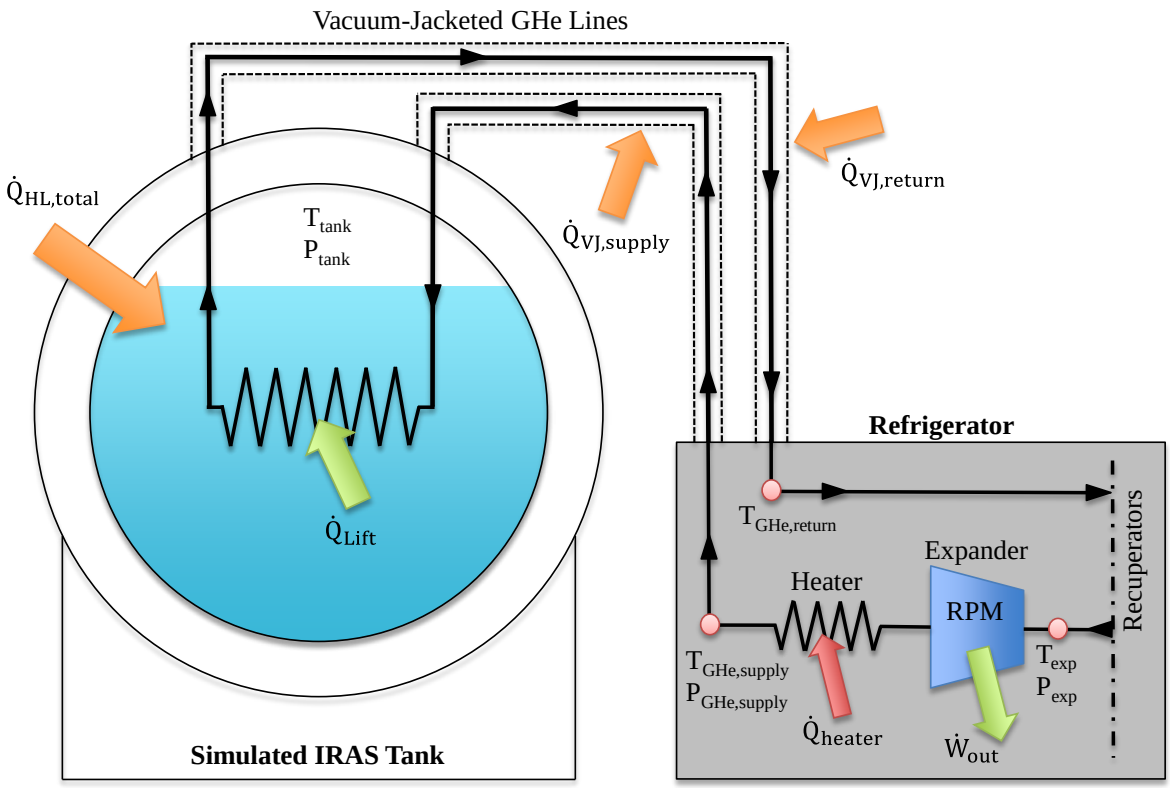

Figure 22: Steady State Refrigerator Performance Model Setup

Due to the laws of conservation, under perfect steady state conditions the total tank heat leak should match the heat exchanger lift exactly since the tank is a closed system. From this it is possible to set up an energy balance between the IRAS tank and refrigerator, and given the helium supply and return properties, examine the relationship between the two over time. This is summarized in equation 18. And by incorporating the additional heater power, the total work extracted by the expander was calculated per equation 19.

$$\dot{Q}_{HL,total} = \dot{Q}_{Lift} = \dot{m}_{GHe}\left(h_{GHe,return} - h_{GHe,supply}\right) - \dot{Q}_{VJ,supply} - \dot{Q}_{VJ,return} \tag{18}$$

$$\dot{W}_{out} = \dot{Q}_{Lift} + \dot{Q}_{VJ,supply} + \dot{Q}_{VJ,return} \tag{19}$$

The helium mass flow rate is a function of numerous factors, and is unique to each refrigeration system. In the case of the GODU-LH2 unit, it was calculated with respect to what is best described as the "virtual piston displacement"—a specific function derived from manufacturer supplied calibration data to calculate the displacement based on RPM, but not the actual physical distance the piston travels. In general, when running at full capacity (i.e. with LN_2 precooling) the mass flow rate followed the trends presented in appendix A when the LH_2 temperature dropped below the NBP, and was around 22 g/s on average; and without precooling it was around 13 g/s. Using the virtual displacement, the virtual piston volume was calculated, followed by the mass of helium that entered the expansion chamber each rotation based on the density at T_{EXP} and P_{EXP}.

$$\widehat{X}_{piston} = f(RPM) \;\rightarrow\; \widehat{V}_{piston} = \pi\left(\frac{D_{piston}}{2}\right)^2 \widehat{X}_{piston} \tag{20}$$

$$\rho_{GHe} = f(T_{EXP}, P_{EXP}) \;\rightarrow\; m_{GHe} = \rho_{GHe}\widehat{V}_{piston} \;\rightarrow\; \dot{m}_{GHe} = \frac{2m_{GHe}RPM}{60}\ (2\ \text{pistons}) \tag{21}$$

Figures 23 through 25 show the results of applying equations 18, 20 and 21 over each of the ZBO-PC analysis regions, and compares the calculated exchanger lift to the tank heat leak. Tank temperature and pressure, as well as the helium supply and return temperatures are also presented for a visual verification of steady state conditions. Due to the fluctuations in both the supply temperature and heat exchanger lift, which were caused by the heater hysteresis, linear curve-fits are included to better understand the overall behavior.

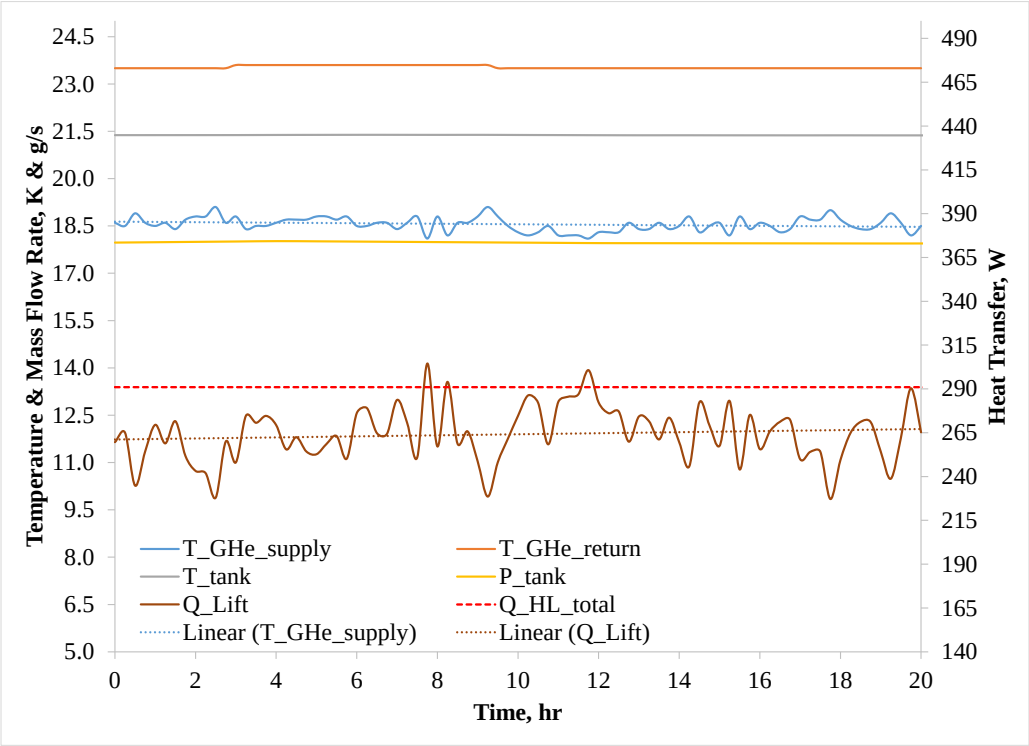

Figure 23: Steady State Results at the 46% Fill Level

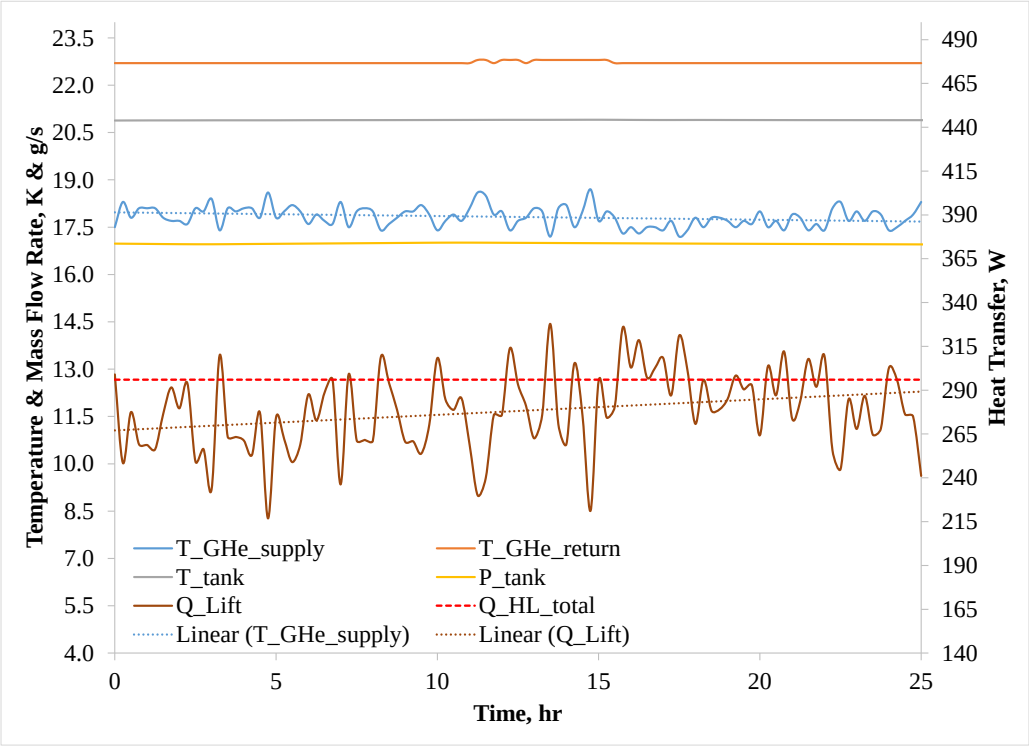

Figure 24: Steady State Results at the 67% Fill Level

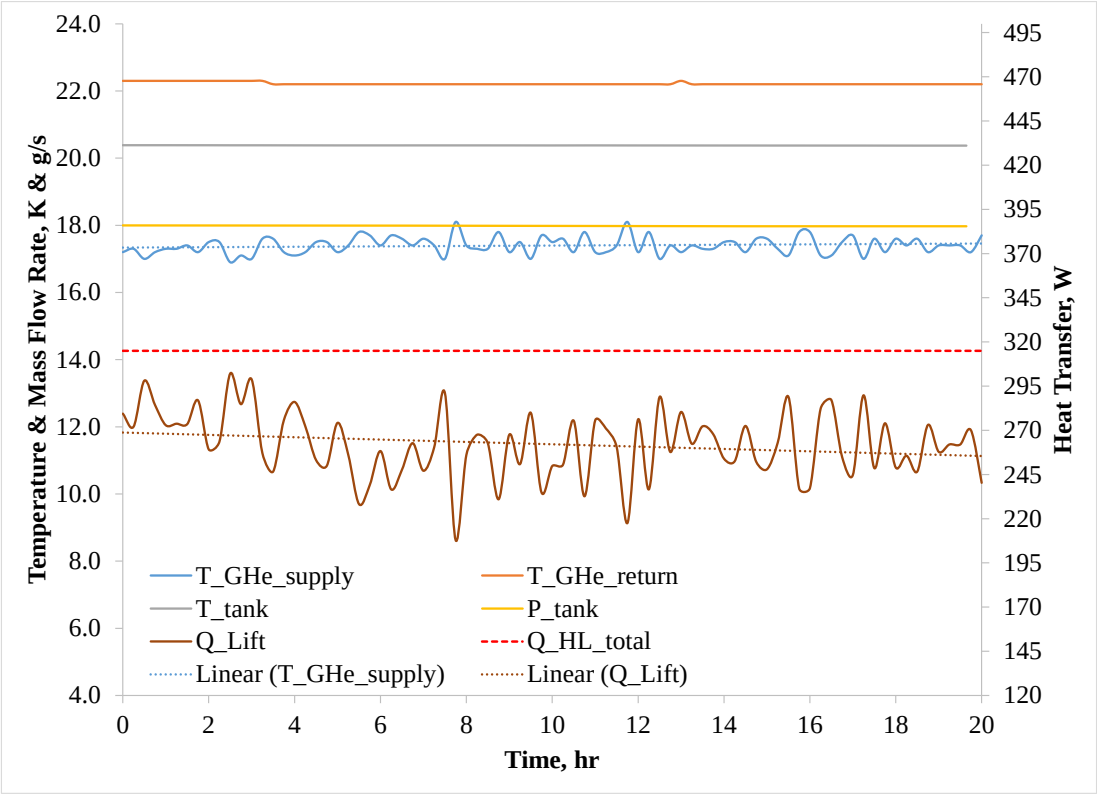

Figure 25: Steady State Results at the 100% Fill Level

Discussion of Steady State Results

There are numerous similarities between the results different presented in figures 23 through 25. In each case the tank pressure and temperature were extremely stable over the entire duration; which seems to confirm that the vessel was indeed at steady state, and that the heat transfer was balanced across its boundary. Also, the average helium supply temperature was fairly flat, with an absolute average slope of 0.009 K/hr between the three fill levels, implying that the refrigerator performance stayed consistent. The helium return temperature reading remained flat as well, which was expected since it was effectively dampened out by the consistent hydrogen temperature. What was unexpected however, was that the average IRAS heat exchanger lift was not flat for any of the time slices examined—although the slopes differed quite a bit, from +0.886

W/hr at 67% full to -0.663 W/hr at 100%—and were consistently lower than the constant heat leak value obtained via boiloff calorimetry testing at each fill level.

The differing average lift slopes seem it suggest that the tank was never at a true steady state condition during the ZBO-PC examination period, even though the pressure and temperature appeared stable. It is expected that, given long enough time scales and ideal conditions, the slopes would trend toward zero. However, because of the changes in environmental heat leak—both expected, as in the case of day/night cycles, or unexpected as in the case of weather—it is possible that an outdoor system will always remain in a state of dynamic equilibrium rather than steady state. Testing at one pressure set point for a long duration, or with the system contained within a climate-controlled building could perhaps determine if a genuine steady state is achievable.

An over-predicted steady state heat leak, or an under-estimated refrigerator lift are the only two explanations for the consistently lower lift-to-heat leak relationship witnessed. After a thorough examination, it was realized that either one, or both could be true. Even though the heat leak was directly determined via calorimetry, these tests were conducted very near normal boiling point. Whereas, the ZBO-PC data was taken when the tank was being maintained at a slight positive gauge pressure. Saturated at a higher pressure, the LH_2 temperature would also be slightly higher than at NBP, which would decrease the overall ΔT across the tank compared to the boiloff tests, and possibly the heat leak as well. Another source of error in the heat leak could be the constant 36 W assumed for each of the vacuum-jacketed helium lines. As mentioned previously, this load was calculated using temperature data across the supply line early on in testing, and it is possible that it decreased slightly over time due to the cooldown process and/or increased insulation performance. Also, the assumption that both the supply and return lines had equal heat

leaks may have affected the result; in reality the return line temperature was always higher than the supply, which affected the heat transfer, and even though they were identical designs, no two vacuum-jacketed lines perform exactly the same.

Possible sources of error that could have contributed to an low estimate for the refrigeration lift include uncertainties in the refrigerator temperature sensor data (± 0.1 K), helium enthalpies from RefProp (1% to 5% for Version 8), and virtual piston displacement (a function of a curve-fit equation that used calibration data that ultimately was used to determine GHe mass flow rate per equation 21). It is believed that the RefProp error bears the most blame, since it was found that adjusting the enthalpies by only 2% eliminated the under-prediction.

CHAPTER FIVE: CONCLUSION

Design, build-up and testing of a large scale Integrated Refrigeration and Storage (IRAS) system known as the Ground Operations Demonstration Unit for Liquid Hydrogen (GODU-LH2) has successfully demonstrated that the marriage of commercially available cryogenic refrigeration systems with large storage tanks is both technically and practically possible. Test data were presented that demonstrated the next generation capabilities IRAS affords, such as zero boiloff, in-situ liquefaction, liquid densification, and even slush production. Aside from the more obvious economic benefits, these capabilities may also improve operational and safety aspects related to cryogenic storage facilities. The venting and filling of vessels are, in many circumstances, considered hazardous operations, requiring specialty expertise and training. Therefore, reducing, or eliminating such processes could translate to increased operational efficiency, schedule flexibility, cost savings, and overall site safety. Possibly the most crucial point however, is that the technology provides a heretofore impossible level of control over the state of the stored fluid. Any end-use process, as well as the interconnecting transfer system, is either directly or indirectly designed around the thermodynamic state of the stored commodity. So, the ability of IRAS to achieve a desired state condition anywhere along the saturation curve effectively opens up a vast set of possibilities never before available to designers. It is therefore foreseeable, given that IRAS is widely accepted and implemented, that designs of future architectures for managing large quantities of cryogenic liquids, such as those required for space launch vehicles and ocean-going tanker ships, could be quite different than the traditional versions that have been in-use, and remained relatively unchanged, for multiple decades.

It is in the spirit of ushering in this future that much effort was spent on developing models that can predict the behavior of IRAS systems, for both steady state and transient operation, and anchoring them with actual GODU-LH2 test data. Steady state analysis focused on a first order estimation of the IRAS tank heat leak, and the comparison to the performance determined via boiloff calorimetry testing. This estimation proved to be conservative, overestimating the actual heat leak by around 6%, but was idealized in many ways also. An examination of refrigerator performance during steady state operation was also presented. Actual refrigerator data was used during zero boiloff pressure control testing—when the tank pressure and hydrogen temperature were virtually constant—to calculate the IRAS heat exchanger lift, and then a comparison was made to the tank heat leak obtained via testing. In each case the calculated lift was slightly lower than the heat leak and exhibited varying trends over time. However, this situation was not physically possible. Because the IRAS tank is a closed system, a balance between the heat leak and lift was the only means by which the tank pressure could stay constant. Numerous factors that may have contributed to this result are proposed, and it is surmised that more than one, or all, could have played a part.

At the outset it was desired to construct a generalized, "universal" model to predict the transient behavior of any IRAS system. Unfortunately, this effort was met with some difficulty when the initial scheme—rooted in the assumption that the hydrogen was saturated throughout the analysis period (i.e. the saturated model)—predicted the behavior at the 46% fill level extremely well, with average errors for the pressure and temperature trends of 1.7% and 0.8% respectively, but failed at the higher levels. At 100% full, when the IRAS heat exchanger was almost completely submerged, the saturated assumption was found to be invalid, which resulted in the model

dramatically over-predicting the de-pressurization rate. This realization led to the creation of a second transient scheme based upon the idea that there was a saturated liquid layer that separated a subcooled liquid region from a saturated vapor region (i.e. the subcooled model). This layer would act as a thermal resistance, retarding the heat transfer between the subcooled liquid (where cooling was taking place) and the vapor, and thus slow down the depressurization rate. The subcooled model successfully predicted the pressure and temperature trends at 100% as closely as the saturated model did at 46%, but did little to explain why a separate set of assumptions was necessary as the liquid level increased.

An obvious takeaway was that constructing a universal model of even a single, well understood IRAS tank is thoroughly challenging, and that extending such an effort to a encompass a completely generalized form that can be used to guide future, high fidelity designs will require additional work. Nevertheless, it is felt as though the work presented here achieved its primary goal by beginning to lay a foundation that can lead to a practical engineering understanding of large-scale IRAS systems, and the application thereof.

CHAPTER SIX: FUTURE WORK

Much progress was made by the GODU-LH2 campaign by proving that next generation IRAS systems and operations such as zero boiloff and densification achievable on a large scale. However, much more work is necessary—both experimentally and analytically—in order to develop a more thorough engineering understanding of the concept. Most importantly, what effect the IRAS heat exchanger geometry and position has on the system behavior needs to be examined. This task is also coupled to the tank geometry and size, as well as the species of stored commodity, which complicates matters somewhat due to the sheer number of potential variations. Development of a detailed computational fluid dynamics (CFD) model of the stored fluid in an IRAS tank will go far to efficiently cycle through different heat exchanger configurations, and could be instrumental in establishing standardized rules, or at least general rules of practice, for designing IRAS heat exchangers. Experimental testing of these configurations on different tank geometries will also be necessary in order to substantiate the CFD results—however, it is believed that laboratory-scale type tests, much smaller and less cost prohibitive than GODU-LH2, will be sufficient to tackle this challenge, and could provide much higher fidelity data. Exploring the effect and potential benefits of refrigerant flow path reversal on the system is also of interest. The GODU-LH2 IRAS tank was locked into a single flow path configuration, but it is believed that the ability to reverse the flow to the heat exchanger—supply to the top manifold rather than the bottom in the case of GODU-LH2—could produce some dramatic mixing effects within the stored fluid, leading to faster depressurization, and possibly better system response times. In addition, cycling the flow while densifying may accelerate the overall process, and could provide enhanced control of slush production at the triple point.

APPENDIX A:
CURVE-FITS FOR HELIUM INPUT DATA

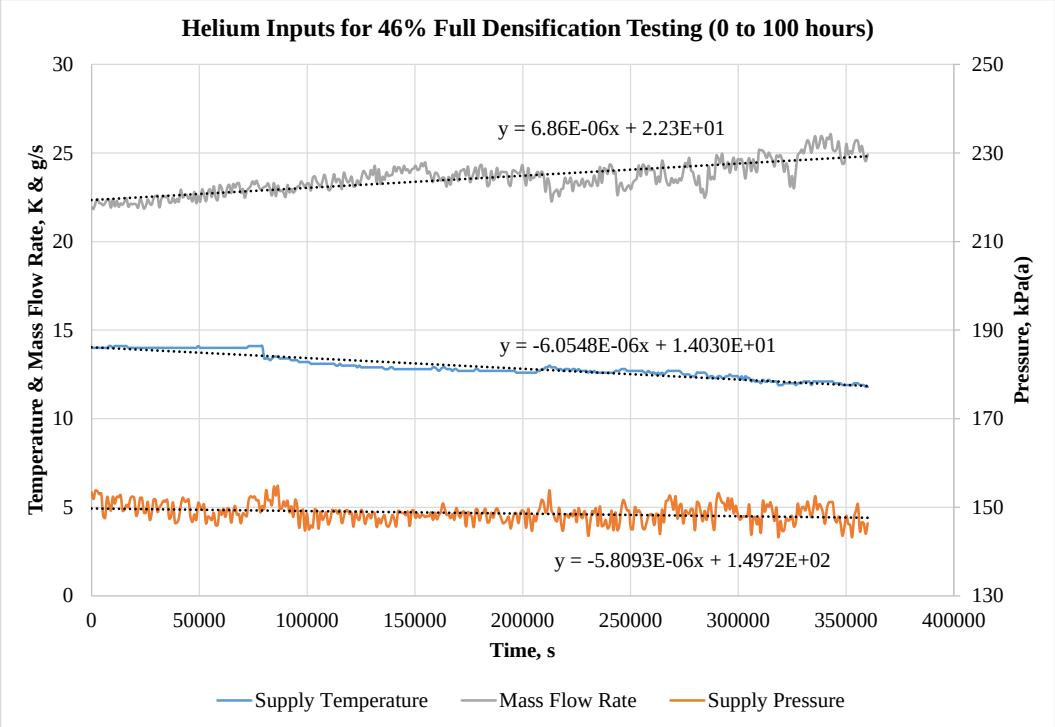

Figure 26: GHe Inputs for Transient Analysis at 46% Fill Level

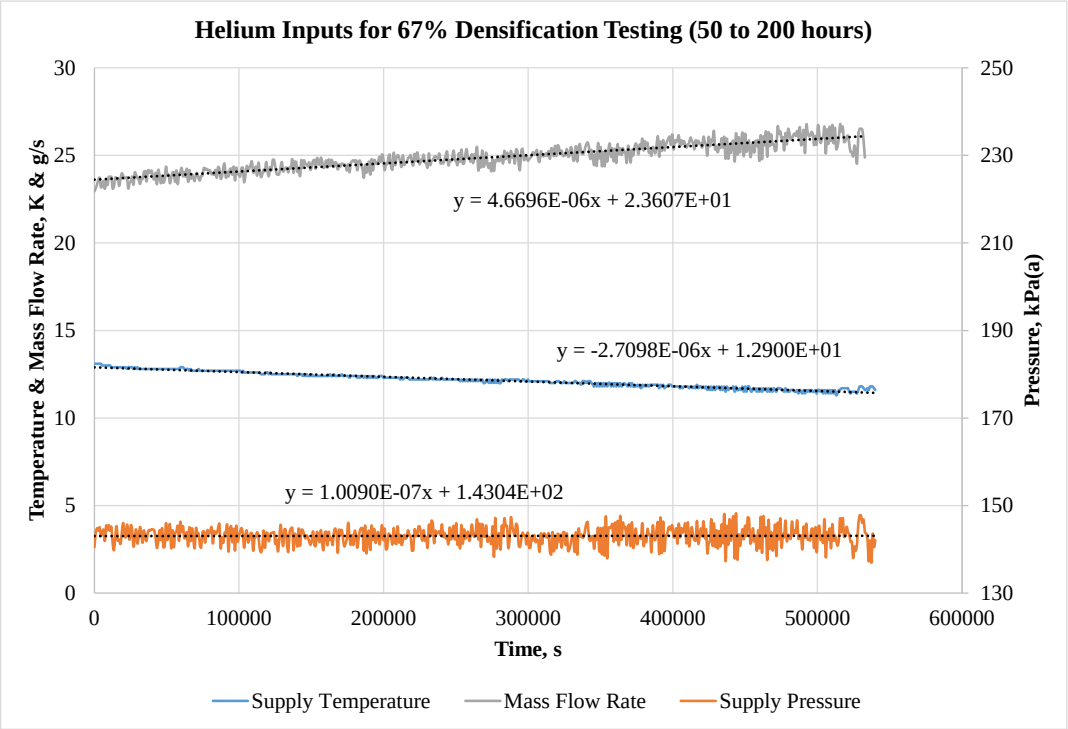

Figure 27: GHe Inputs for Transient Analysis at 67% Fill Level

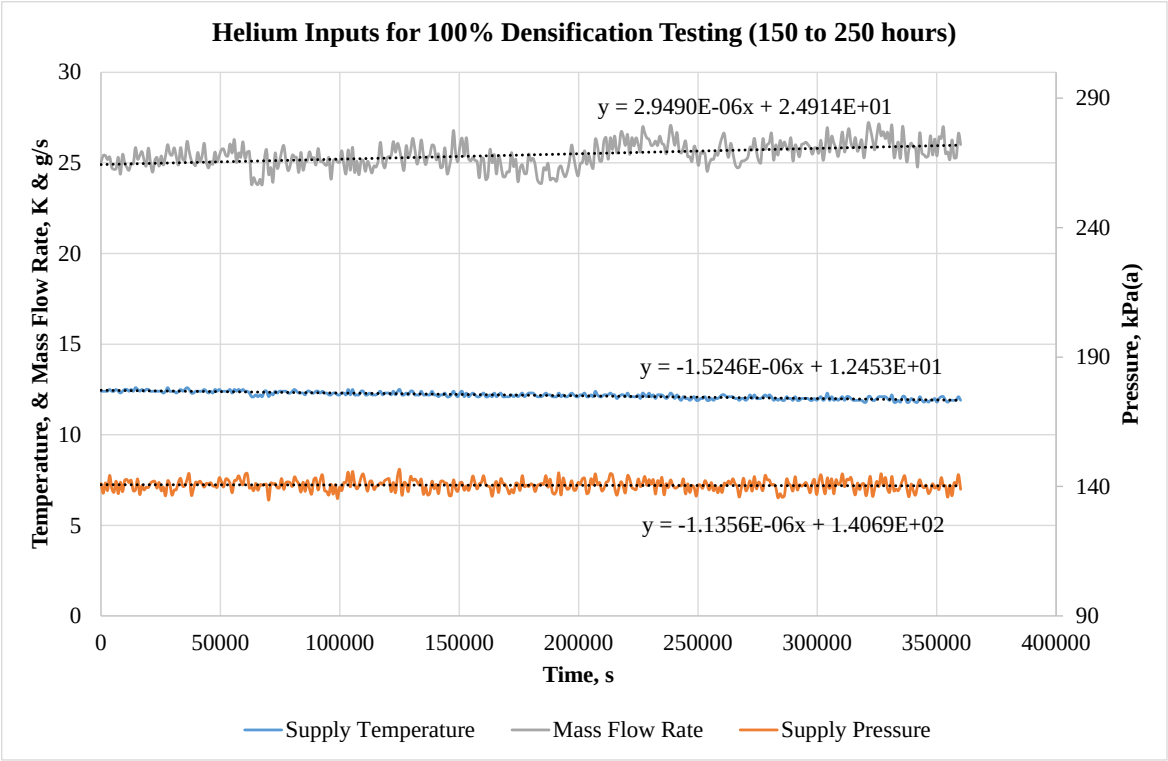

Figure 28: GHe Inputs for Transient Analysis at 100% Fill Level

APPENDIX B:
SATURATED ANALYSIS FLOW CHART

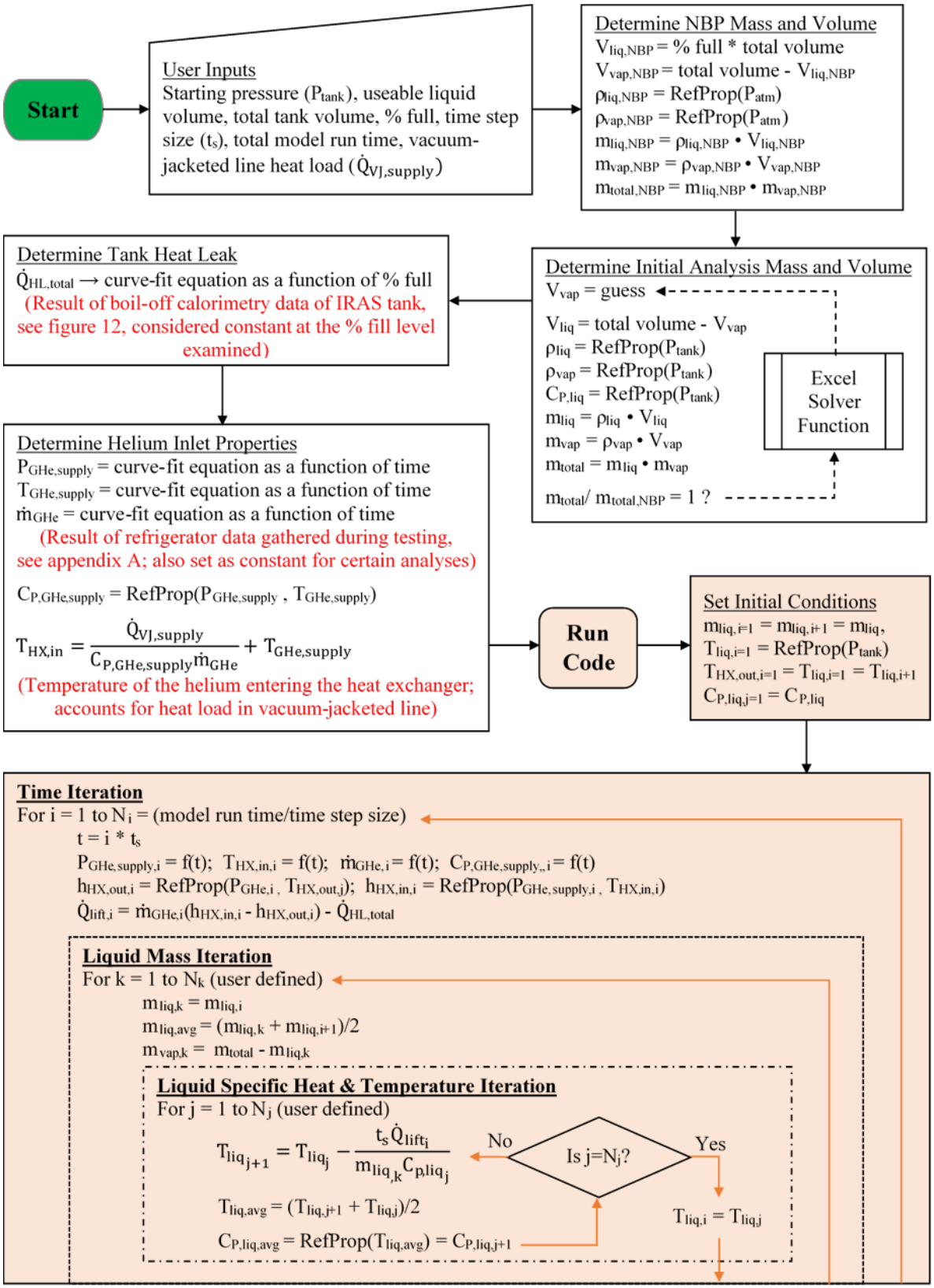
Start
User Inputs
Starting pressure (P_{tank}), useable liquid volume, total tank volume, % full, time step size (t_s), total model run time, vacuum-jacketed line heat load ($\dot{Q}_{VJ,supply}$)
Determine NBP Mass and Volume
$V_{liq,NBP}$ = % full * total volume
$V_{vap,NBP}$ = total volume - $V_{liq,NBP}$
$\rho_{liq,NBP}$ = RefProp(P_{atm})
$\rho_{vap,NBP}$ = RefProp(P_{atm})
$m_{liq,NBP} = \rho_{liq,NBP} \bullet V_{liq,NBP}$
$m_{vap,NBP} = \rho_{vap,NBP} \bullet V_{vap,NBP}$
$m_{total,NBP} = m_{liq,NBP} \bullet m_{vap,NBP}$
Determine Tank Heat Leak
$\dot{Q}_{HL,total}$ → curve-fit equation as a function of % full
(Result of boil-off calorimetry data of IRAS tank, see figure 12, considered constant at the % fill level examined)
Determine Initial Analysis Mass and Volume
V_{vap} = guess
V_{liq} = total volume - V_{vap}
ρ_{liq} = RefProp(P_{tank})
ρ_{vap} = RefProp(P_{tank})
$C_{P,liq}$ = RefProp(P_{tank})
$m_{liq} = \rho_{liq} \bullet V_{liq}$
$m_{vap} = \rho_{vap} \bullet V_{vap}$
$m_{total} = m_{liq} \bullet m_{vap}$
$m_{total}/ m_{total,NBP} = 1$?
Excel Solver Function
Determine Helium Inlet Properties
$P_{GHe,supply}$ = curve-fit equation as a function of time
$T_{GHe,supply}$ = curve-fit equation as a function of time
$\dot{m}_{GHe}$ = curve-fit equation as a function of time
(Result of refrigerator data gathered during testing, see appendix A; also set as constant for certain analyses)
$C_{P,GHe,supply}$ = RefProp($P_{GHe,supply}$, $T_{GHe,supply}$)
$T_{HX,in} = \frac{\dot{Q}_{VJ,supply}}{C_{P,GHe,supply}\dot{m}_{GHe}} + T_{GHe,supply}$
(Temperature of the helium entering the heat exchanger; accounts for heat load in vacuum-jacketed line)
Run Code
Set Initial Conditions
$m_{liq,i=1} = m_{liq,i+1} = m_{liq}$,
$T_{liq,i=1}$ = RefProp(P_{tank})
$T_{HX,out,i=1} = T_{liq,i=1} = T_{liq,i+1}$
$C_{P,liq,j=1} = C_{P,liq}$
Time Iteration
For i = 1 to N_i = (model run time/time step size)
$t = i * t_s$
$P_{GHe,supply,i} = f(t)$; $T_{HX,in,i} = f(t)$; $\dot{m}_{GHe,i} = f(t)$; $C_{P,GHe,supply,,i} = f(t)$
$h_{HX,out,i}$ = RefProp($P_{GHe,i}$, $T_{HX,out,j}$); $h_{HX,in,i}$ = RefProp($P_{GHe,supply,i}$, $T_{HX,in,i}$)
$\dot{Q}_{lift,i} = \dot{m}_{GHe,i}(h_{HX,in,i} - h_{HX,out,i}) - \dot{Q}_{HL,total}$
Liquid Mass Iteration
For k = 1 to N_k (user defined)
$m_{liq,k} = m_{liq,i}$
$m_{liq,avg} = (m_{liq,k} + m_{liq,i+1})/2$
$m_{vap,k} = m_{total} - m_{liq,k}$
Liquid Specific Heat & Temperature Iteration
For j = 1 to N_j (user defined)
$T_{liq_{j+1}} = T_{liq_j} - \frac{t_s \dot{Q}_{lift_i}}{m_{liq_k} C_{p,liq_j}}$
No
Is j=N_j?
Yes
$T_{liq,i} = T_{liq,j}$
$T_{liq,avg} = (T_{liq,j+1} + T_{liq,j})/2$
$C_{P,liq,avg}$ = RefProp($T_{liq,avg}$) = $C_{P,liq,j+1}$

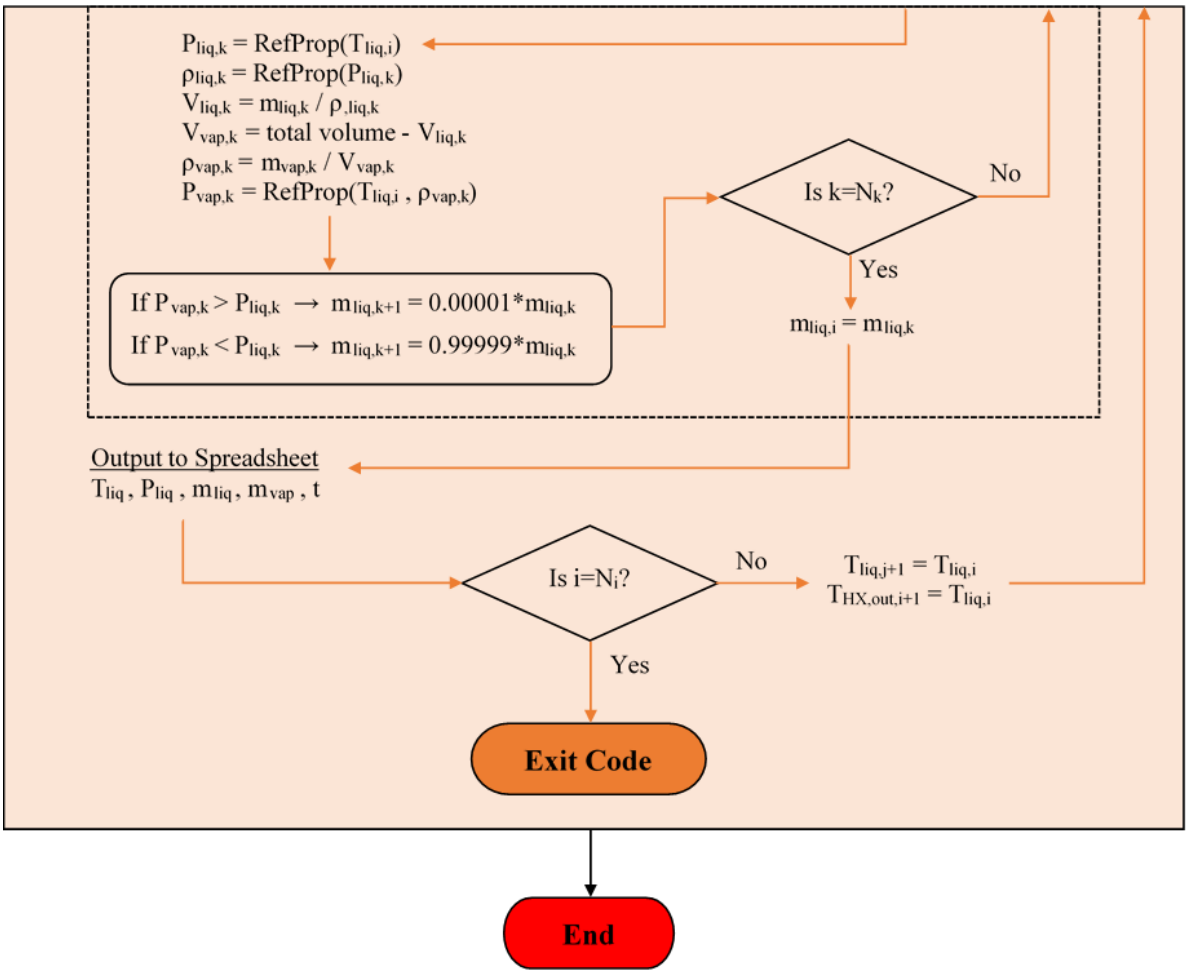
$P_{liq,k} = RefProp(T_{liq,i})$
$\rho_{liq,k} = RefProp(P_{liq,k})$
$V_{liq,k} = m_{liq,k} / \rho_{,liq,k}$
$V_{vap,k}$ = total volume - $V_{liq,k}$
$\rho_{vap,k} = m_{vap,k} / V_{vap,k}$
$P_{vap,k} = RefProp(T_{liq,i}, \rho_{vap,k})$
If $P_{vap,k} > P_{liq,k} \rightarrow m_{liq,k+1} = 0.00001*m_{liq,k}$
If $P_{vap,k} < P_{liq,k} \rightarrow m_{liq,k+1} = 0.99999*m_{liq,k}$
Is $k=N_k$?
No
Yes
$m_{liq,i} = m_{liq,k}$
Output to Spreadsheet
T_{liq}, P_{liq}, m_{liq}, m_{vap}, t
Is $i=N_i$?
No
$T_{liq,j+1} = T_{liq,i}$
$T_{HX,out,i+1} = T_{liq,i}$
Yes
Exit Code
End

APPENDIX C:
SUBCOOLED ANALYSIS FLOW CHART

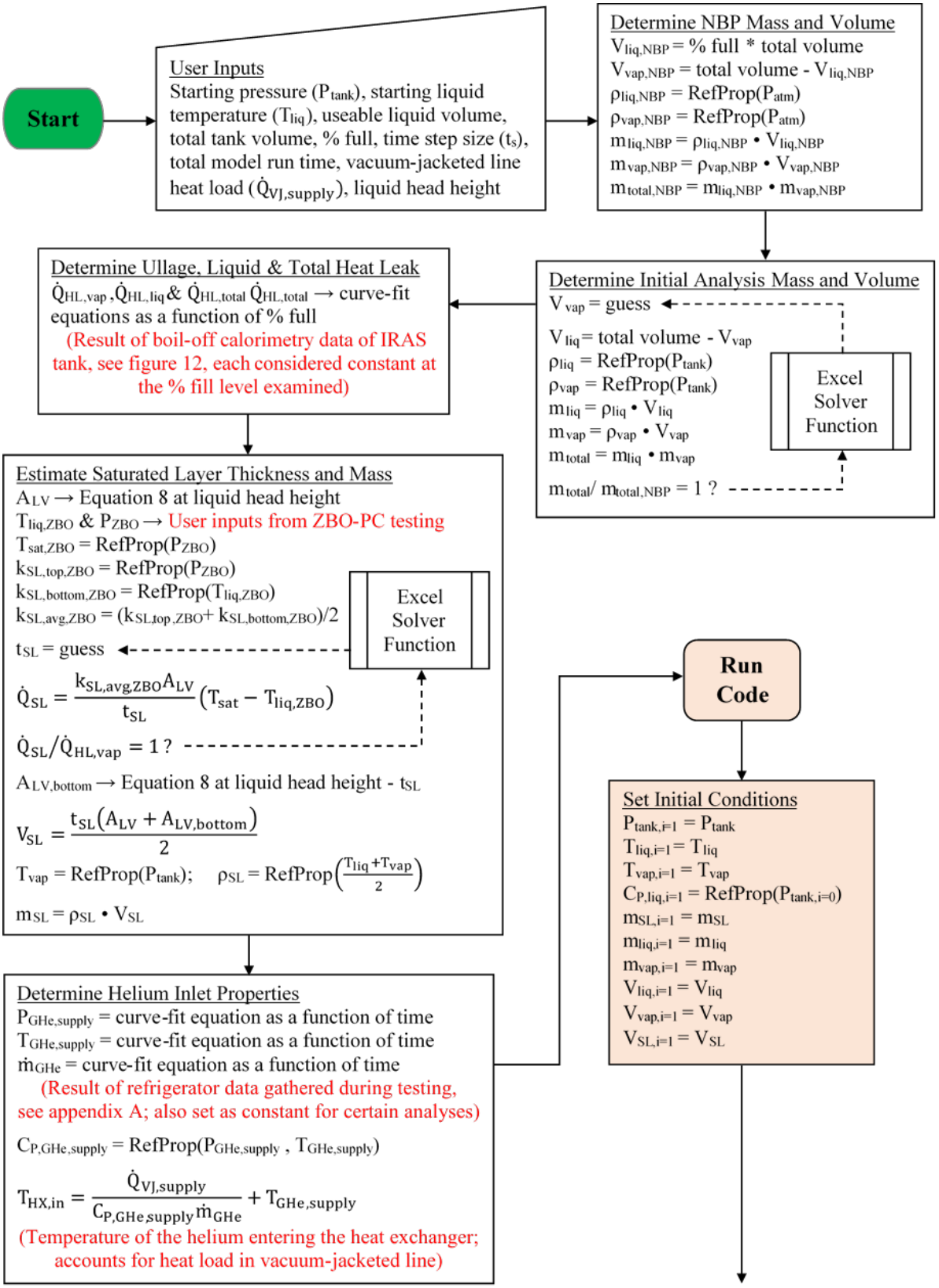
Start
User Inputs
Starting pressure (P_{tank}), starting liquid temperature (T_{liq}), useable liquid volume, total tank volume, % full, time step size (t_s), total model run time, vacuum-jacketed line heat load ($\dot{Q}_{VJ,supply}$), liquid head height
Determine NBP Mass and Volume
$V_{liq,NBP}$ = % full * total volume
$V_{vap,NBP}$ = total volume - $V_{liq,NBP}$
$\rho_{liq,NBP}$ = RefProp(P_{atm})
$\rho_{vap,NBP}$ = RefProp(P_{atm})
$m_{liq,NBP} = \rho_{liq,NBP} \bullet V_{liq,NBP}$
$m_{vap,NBP} = \rho_{vap,NBP} \bullet V_{vap,NBP}$
$m_{total,NBP} = m_{liq,NBP} \bullet m_{vap,NBP}$
Determine Initial Analysis Mass and Volume
V_{vap} = guess
V_{liq} = total volume - V_{vap}
ρ_{liq} = RefProp(P_{tank})
ρ_{vap} = RefProp(P_{tank})
$m_{liq} = \rho_{liq} \bullet V_{liq}$
$m_{vap} = \rho_{vap} \bullet V_{vap}$
$m_{total} = m_{liq} \bullet m_{vap}$
$m_{total}/ m_{total,NBP} = 1$?
Excel Solver Function
Determine Ullage, Liquid & Total Heat Leak
$\dot{Q}_{HL,vap}$, $\dot{Q}_{HL,liq}$ & $\dot{Q}_{HL,total}$ $\dot{Q}_{HL,total}$ → curve-fit equations as a function of % full
(Result of boil-off calorimetry data of IRAS tank, see figure 12, each considered constant at the % fill level examined)
Estimate Saturated Layer Thickness and Mass
A_{LV} → Equation 8 at liquid head height
$T_{liq,ZBO}$ & P_{ZBO} → User inputs from ZBO-PC testing
$T_{sat,ZBO}$ = RefProp(P_{ZBO})
$k_{SL,top,ZBO}$ = RefProp(P_{ZBO})
$k_{SL,bottom,ZBO}$ = RefProp($T_{liq,ZBO}$)
$k_{SL,avg,ZBO} = (k_{SL,top,ZBO} + k_{SL,bottom,ZBO})/2$
t_{SL} = guess
$\dot{Q}_{SL} = \frac{k_{SL,avg,ZBO} A_{LV}}{t_{SL}} (T_{sat} - T_{liq,ZBO})$
$\dot{Q}_{SL}/\dot{Q}_{HL,vap} = 1$?
Excel Solver Function
$A_{LV,bottom}$ → Equation 8 at liquid head height - t_{SL}
$V_{SL} = \frac{t_{SL}(A_{LV} + A_{LV,bottom})}{2}$
T_{vap} = RefProp(P_{tank}); ρ_{SL} = RefProp$\left(\frac{T_{liq}+T_{vap}}{2}\right)$
$m_{SL} = \rho_{SL} \bullet V_{SL}$
Determine Helium Inlet Properties
$P_{GHe,supply}$ = curve-fit equation as a function of time
$T_{GHe,supply}$ = curve-fit equation as a function of time
$\dot{m}_{GHe}$ = curve-fit equation as a function of time
(Result of refrigerator data gathered during testing, see appendix A; also set as constant for certain analyses)
$C_{P,GHe,supply}$ = RefProp($P_{GHe,supply}$, $T_{GHe,supply}$)
$T_{HX,in} = \frac{\dot{Q}_{VJ,supply}}{C_{P,GHe,supply}\dot{m}_{GHe}} + T_{GHe,supply}$
(Temperature of the helium entering the heat exchanger; accounts for heat load in vacuum-jacketed line)
Run Code
Set Initial Conditions
$P_{tank,i=1} = P_{tank}$
$T_{liq,i=1} = T_{liq}$
$T_{vap,i=1} = T_{vap}$
$C_{P,liq,i=1}$ = RefProp($P_{tank,i=0}$)
$m_{SL,i=1} = m_{SL}$
$m_{liq,i=1} = m_{liq}$
$m_{vap,i=1} = m_{vap}$
$V_{liq,i=1} = V_{liq}$
$V_{vap,i=1} = V_{vap}$
$V_{SL,i=1} = V_{SL}$

Time Iteration

For $i = 1$ to N_i = (model run time/time step size)

$t = i * t_s$

$P_{GHe,supply,i} = f(t)$; $T_{HX,in,i} = f(t)$; $\dot{m}_{GHe,i} = f(t)$; $C_{P,GHe,supply,i} = f(t)$

Convergence Iteration

$T_{liq,i+1}(j=0) = T_{liq,i}$

$T_{vap,i+1}(j=0) = T_{vap,i}$

$P_{tank,i+1}(j=0) = P_{tank,i}$

$C_{p,liq,i+1}(j=0) = C_{p,liq,i}$

$m_{liq,i+1}(j=0) = m_{liq,i}$

For $j = 0$ to N_j (user defined)

$m_{liq,avg,j} = (m_{liq,I} + m_{liq,i+1})/2$

$C_{p,liq,avg,j} = (C_{p,liq,i} + C_{p,liq,i+1})/2$

$T_{liq,avg,j} = (T_{liq,i} + T_{liq,i+1})/2$

$P_{tank,avg,j} = (P_{tank,i} + P_{tank,i+1})/2$

$T_{vap,avg,j} = (T_{vap,i} + T_{vap,i+1})/2$

$k_{SL,top} = \text{RefProp}(T_{vap,avg})$ {Saturated liquid @ $T_{vap,avg}$}

$k_{SL,bottom} = \text{RefProp}(T_{liq,avg})$ {Saturated liquid @ $T_{liq,avg}$}

$k_{SL,avg} = (k_{SL,top} + k_{SL,bottom})/2$

$$\dot{Q}_{LV} = \frac{k_{SL,avg} A_{LV,top}}{t_{SL}} \left(T_{vap,avg} - T_{liq,avg}\right)$$

$\dot{Q}_{vap} = \dot{Q}_{LV} - \dot{Q}_{HL,vap}$

$h_{fg} = \text{RefProp}(P_{tank,avg})$

$\dot{m}_{condense} = \dot{Q}_{vap}/h_{fg}$

$m_{condense} = \dot{m}_{condense} * t_s$

$\rho_{condense} = \text{RefProp}(P_{tank,avg})$

$V_{condense} = m_{condense} / \rho_{condense}$

$V_{liq,i+1} = V_{liq,i} + V_{condense}$

$V_{vap,i+1} = V_{vap,i} - V_{condense}$

$V_{SL,i+1}$ = total tank volume – $(V_{liq,i+1} + V_{condense})$

$m_{vap,i+1} = m_{vap,i} - m_{condense}$

$\rho_{vap,i+1} = m_{vap,i+1} / V_{vap,i+1}$

$T_{vap,i+1} = \text{RefProp}(\rho_{vap,i+1})$ {Saturated vapor}

$P_{tank,i+1} = \text{RefProp}(T_{vap,i+1})$

$T_{HX,out} = T_{liq,i+1}$

$h_{HX,out} = \text{RefProp}(P_{GHe,i}, T_{HX,out})$; $h_{HX,in} = \text{RefProp}(P_{GHe,i}, T_{HX,in,i})$

$\dot{Q}_{lift} = \dot{m}_{GHe,i}(h_{HX,in,i} - h_{HX,out}) - \dot{Q}_{HL,liq}$

$$T_{liq_{i+1}} = T_{liq_i} - \frac{t_s(\dot{Q}_{lift} - \dot{Q}_{LV})}{m_{liq,avg,j} C_{liq,avg,j}}$$

$C_{p,liq,i+1} = \text{RefProp}(P_{tank,i+1}, T_{liq,i+1})$

$\rho_{SL,top} = \text{RefProp}(T_{vap,avg})$ {Saturated liquid @ $T_{vap,avg}$}

$\rho_{SL,bottom} = \text{RefProp}(T_{liq,avg})$ {Saturated liquid @ $T_{liq,avg}$ }

$\rho_{SL,i+1} = (\rho_{SL,top} + \rho_{SL,bottom})/2$

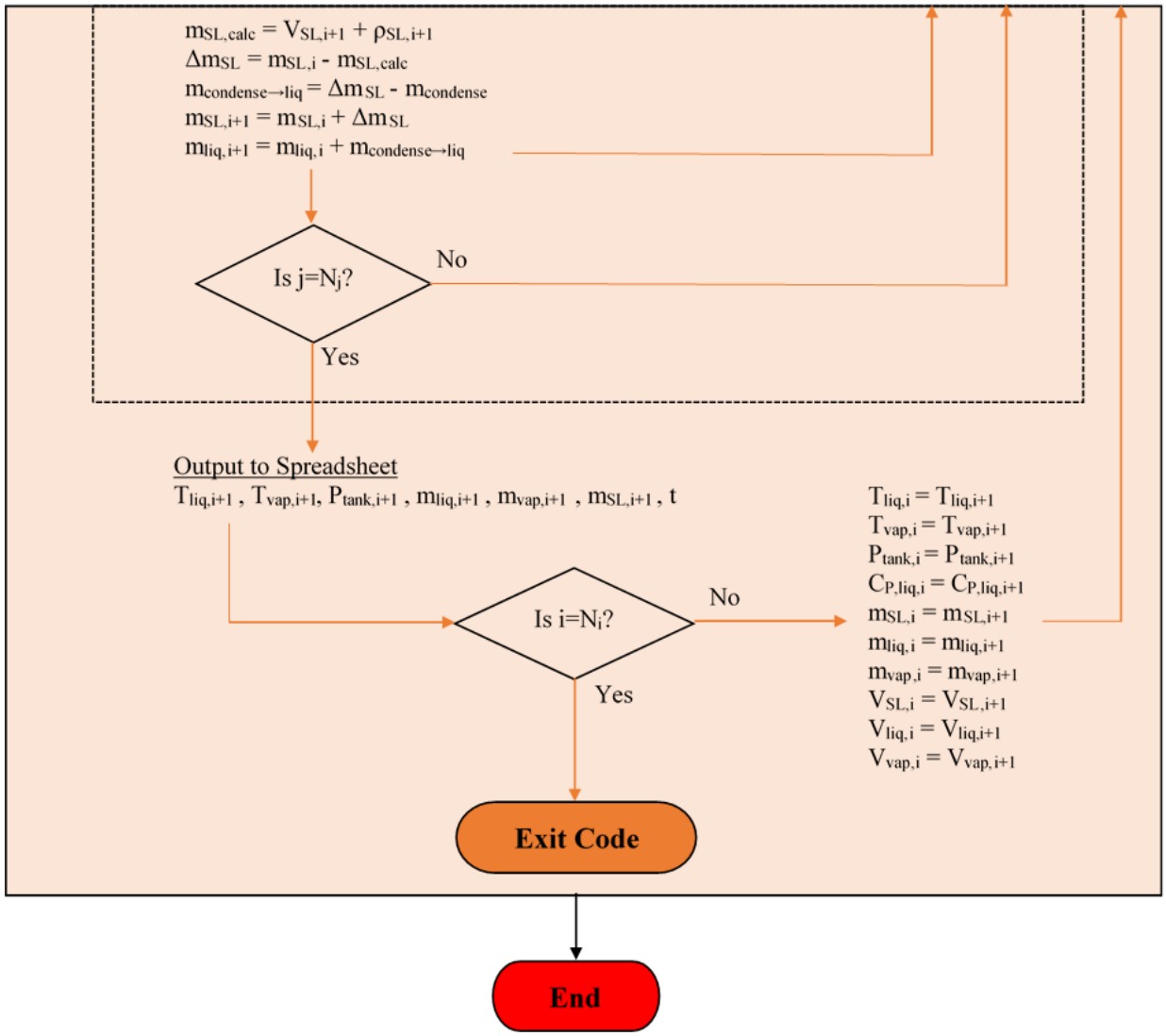
$m_{SL,calc} = V_{SL,i+1} + \rho_{SL,i+1}$
$\Delta m_{SL} = m_{SL,i} - m_{SL,calc}$
$m_{condense \rightarrow liq} = \Delta m_{SL} - m_{condense}$
$m_{SL,i+1} = m_{SL,i} + \Delta m_{SL}$
$m_{liq,i+1} = m_{liq,i} + m_{condense \rightarrow liq}$
Is $j=N_j$?
No
Yes
Output to Spreadsheet
$T_{liq,i+1}$, $T_{vap,i+1}$, $P_{tank,i+1}$, $m_{liq,i+1}$, $m_{vap,i+1}$, $m_{SL,i+1}$, t
Is $i=N_i$?
No
Yes
$T_{liq,i} = T_{liq,i+1}$
$T_{vap,i} = T_{vap,i+1}$
$P_{tank,i} = P_{tank,i+1}$
$C_{P,liq,i} = C_{P,liq,i+1}$
$m_{SL,i} = m_{SL,i+1}$
$m_{liq,i} = m_{liq,i+1}$
$m_{vap,i} = m_{vap,i+1}$
$V_{SL,i} = V_{SL,i+1}$
$V_{liq,i} = V_{liq,i+1}$
$V_{vap,i} = V_{vap,i+1}$
Exit Code
End

APPENDIX D:
GODU-LH2 IRAS HEAT EXCHANGER AREA RELATIONS

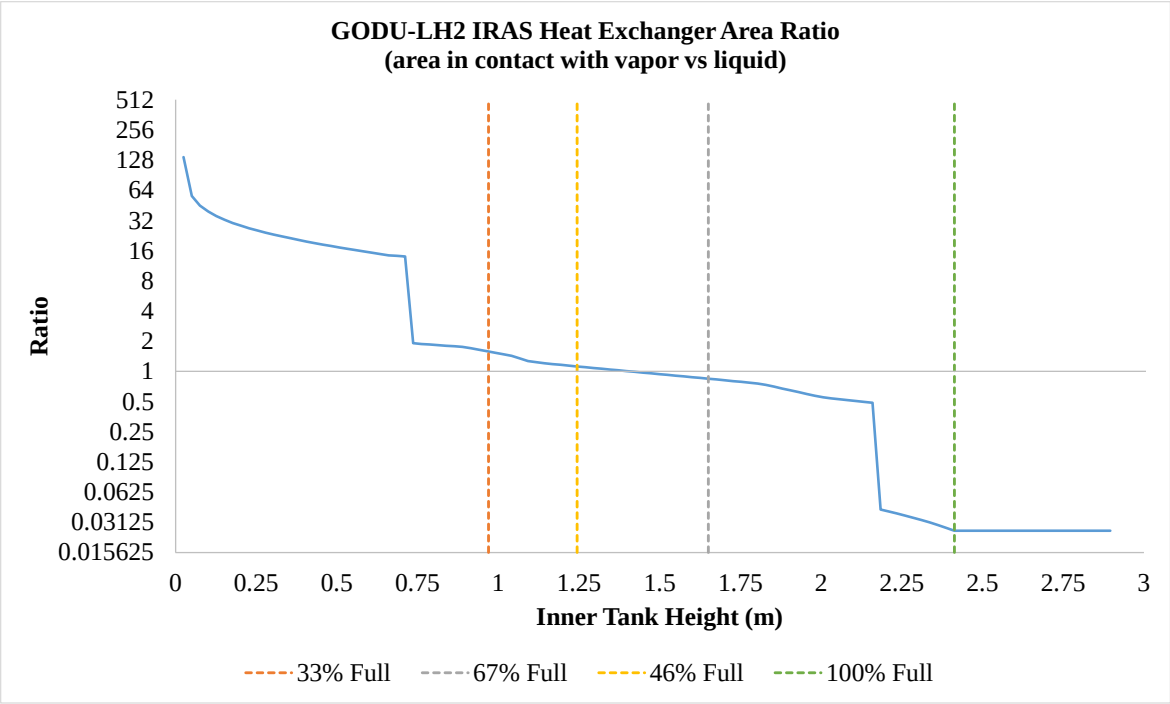

Figure 29: IRAS Heat Exchanger Area Ratio vs. Inner Tank Height

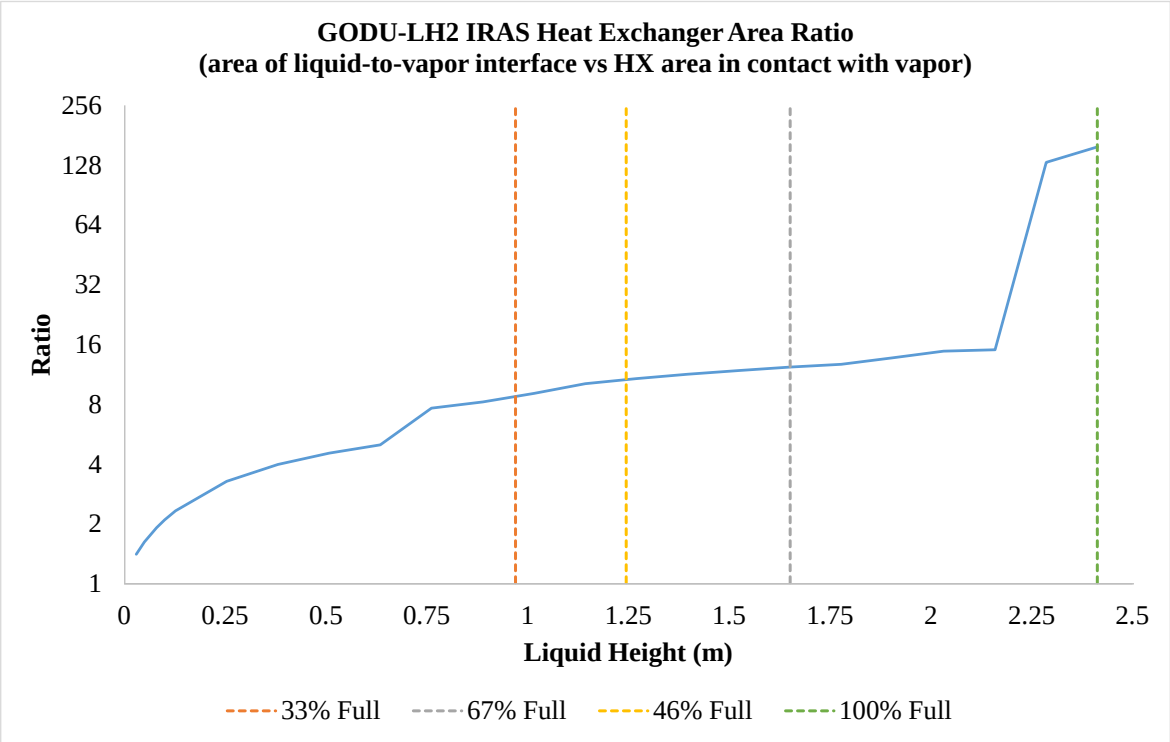

Figure 30: IRAS Heat Exchanger Area Ratio vs. Liquid Height

REFERENCES

[1] Papanelopoulou, F. (2013). Louis Paul Cailletet: The liquefaction of oxygen and the emergence of low-temperature research. Notes and Records of the Royal Society, 67(4), pp.355-373.

[2] Shell.com. (2017). Prelude FLNG in numbers. [online] Available at: https://www.shell.com/about-us/major-projects/prelude-flng/prelude-flng-in-numbers.html [Accessed 27 Dec. 2017].

[3] Bilstein, R. (1980). Stage To Saturn: A Technological History of the Apollo/Saturn Launch Vehicles. Washington, DC: National Aeronautics and Space Administration., NASA SP-4206

[4] Partridge, J. K. (2012), Fractional consumption of liquid hydrogen and liquid oxygen during the space shuttle program. Advances in Cryogenic Engineering, AIP Conference Proceedings, Vol.1434, pp.1765-1770

[5] NASA. (2015). *Space Launch System (SLS) Overview*. [online] Available at: https://www.nasa.gov/exploration/systems/sls/overview.html [Accessed 7 Jan. 2018].

[6] Fbo.gov. (2018). *Upgrade Liquid Hydrogen (LH2) System, Launch Complex 39B - Federal Business Opportunities: Opportunities.* [online], Solicitation number 80KSC018R0016, Available at: https://www.fbo.gov [Accessed 4 Jun. 2018].

[7] Swanger, A. M., Notardonato, W U., Johnson, W. L. and Tomsik, T. M. (2016), Integrated Refrigeration and Storage for Advanced Liquid Hydrogen Operations. Cryocoolers 19, 19th International Cryocooler Conference Proceedings, Vol.19, pp.513-522

[8] Birmingham, B., Brown, E., Class, C. and Schmidt, A. (1957). Vessels for the storage and transport of liquid hydrogen. Journal of Research of the National Bureau of Standards, 58(5), pp.243-253.

[9] Stearns, T., Sandell, D. and Burlew, J. (1954), The Refrigerated Transport Dewar. Advances in Cryogenic Engineering, Cryogenic Engineering Conference Proceedings, Vol.1, pp.35-40

[10] Pastuhov, A. (1954), Helium Refrigeration. Advances in Cryogenic Engineering, Cryogenic Engineering Conference Proceedings, Vol.1, pp.41-43

[11] Hastings, L., Plachta, D., Salerno, L. and Kittel, P. (2001). An overview of NASA efforts on zero boiloff storage of cryogenic propellants. Cryogenics, 41(11-12), pp.833-839.

[12] Plachta, D., Johnson, W. and Feller, J. (2016). Zero boiloff system testing. Cryogenics, 74, pp.88-94.

[13] Notardonato, W. U., Baik, J. H. and McIntosh, G. E. (2004), Operational testing of densified hydrogen using G-M refrigeration, Advances in Cryogenic Engineering, AIP Conference Proceedings, Vol. 49, pp.64-74, DOI: 10.1063/1.1774668

[14] Notardonato, W.U., Johnson, W. L., Oliveria, J. and Jumper, K. (2010), Experimental results of integrated refrigeration and storage system testing, Advances in Cryogenic Engineering, AIP Conference Proceedings, Vol. 55, pp.1369-1376

[15] Notardonato, W., Swanger, A., Fesmire, J., Jumper, K., Johnson, W. and Tomsik, T. (2017). Final test results for the ground operations demonstration unit for liquid hydrogen. Cryogenics, 88, pp.147-155.

[16] Swanger, A. M., Notardonato, W. U., Fesmire, J. E., Jumper, K. M., Johnson, W. L. and Tomsik, T. M. (2017), Large scale production of densified hydrogen to the triple point and below, Advances in Cryogenic Engineering, IOP Conf. Series: Materials Science and Engineering 101, doi:10.1088/1757-899X/278/1/012013

[17] Notardonato, W. U., Swanger, A. M., Fesmire, J. E., Jumper, K. M., Johnson, W. L. and Tomsik, T. M. (2017), Zero boiloff methods for large scale liquid hydrogen tanks using integrated refrigeration and storage, Advances in Cryogenic Engineering, IOP Conf. Series: Materials Science and Engineering 101, doi:10.1088/1757-899X/278/1/012012

[18] Swanger, A. M., Jumper, K. M., Fesmire, J. E., and Notardonato, W. U. (2015), Modification of a Liquid Hydrogen Tank for Integrated Refrigeration and Storage, Advances in Cryogenic Engineering, IOP Conference Series: Materials Science and Engineering 101, doi:10.1088/1757-899X/101/1/012080

[19] Swanger, A. M., Notardonato, W. U., and Jumper, K. M. (2015), ASME Section VIII Recertification of a 33,000 Gallon Vacuum-Jacketed LH2 Storage Vessel for Densified Hydrogen Testing at NASA Kennedy Space Center, Proceedings of the ASME Pressure Vessels and Piping Conference, Massachusetts, Boston, doi:10.1115/PVP2015-45625

[20] Fesmire, J. E., Tomsik, T. M., Bonner, T., Oliveira, J. M., Conyers, H. J., Johnson, W. L. and Notardonato, W. U. (2014), Integrated heat exchanger design for a cryogenic storage tank, Advances in Cryogenic Engineering, AIP Conference. Proceedings, Vol. 1573, pp.1365-1372, doi:10.1063/1.4860865

[21] Lemmon, E. (2018). Reference Fluid Thermodynamic and Transport Properties Database (REFPROP). [online] NIST. Available at: https://www.nist.gov/programs-projects/reference-fluid-thermodynamic-and-transport-properties-database-refprop [Accessed 5 Feb. 2018].

[22] Ewart, R. O. and Dergance, R. H., (1978), Cryogenic Propellant Densification Study, NASA CR-159438

[23] ASTM C740 / C740M-13, (2013), Standard Guide for Evacuated Reflective Insulation In Cryogenic Service, ASTM International, West Conshohocken, PA, www.astm.org

[24] ASTM C1774-13, (2013), Standard Guide for Thermal Performance Testing of Cryogenic Insulation Systems, ASTM International, West Conshohocken, PA, www.astm.org

[25] Trc.nist.gov. (2018). *Cryogenics Material Properties*. [online] Available at: https://trc.nist.gov/cryogenics/materials/materialproperties.htm [Accessed 9 May 2018].

[26] Fesmire, J. E. and Johnson, W. L., (2018). Cylindrical cryogenic calorimeter testing of six types of multilayer insulation systems. Cryogenics, 89, pp.58-75.